Improved precision calculation of the $0\nu\beta\beta$ contact term within chiral effective field theory

Graham Van Goffrier*

University of Southampton, Southampton, United Kingdom and University College London, London, United Kingdom

(Received 7 January 2025; accepted 3 March 2025; published 31 March 2025)

Neutrinoless double-beta ($0\nu\beta\beta$) decay is an as-yet unobserved nuclear process, which stands to provide crucial insights for model building beyond the Standard Model of particle physics. Its detection would simultaneously confirm the hypothesis that neutrinos are Majorana fermions, thus violating lepton-number conservation, and provide the first measurement of the absolute neutrino mass scale. This work aims to improve the estimation within chiral effective field theory of the so-called "contact term" for $0\nu\beta\beta$ decay, a short-range two-nucleon effect that is unaccounted for in traditional nuclear approaches to the process. We conduct a thorough review of the justifications for this contact term and the most precise computation of its size to date [$g_\nu^{NN} = 1.3(6)$ at renormalization point $\mu = m_\pi$], whose precision is limited by a truncation to elastic intermediate hadronic states. We then perform an extension of this analysis to a subleading class of inelastic intermediate states that we characterize, delivering an updated figure for the contact coefficient [$g_\nu^{NN} = 1.4(3)$ at $\mu = m_\pi$] with uncertainty reduced by half. Such *ab initio* nuclear results, especially with enhanced precision, show promise for the resolution of disagreements between estimates of $0\nu\nu\beta\beta$ from different many-body methods.

DOI: 10.1103/PhysRevD.111.055033

I. INTRODUCTION

From a theory perspective, the usefulness of neutrinoless double-beta ($0\nu\beta\beta$) decay as a probe of neutrino mass and of lepton-number violation (LNV) is constrained by the precision with which its half-life may be related to physical model parameters. This precision is most severely limited by our ability to calculate many-body or even few-body nuclear structure, a challenge amplified by the inherent two-body nature of $0\nu\beta\beta$ decay. The factorization of the $0\nu\beta\beta$ amplitude into a leptonic phase-space factor (PSF) and a hadronic nuclear matrix element (NME) [1], although inexact, has become a standard approximation. This is, in part, because the imprecision introduced by this factorization falls well below other theoretical uncertainties [2] and, in part, because the PSFs are calculable with relative ease compared to the NMEs.

No exact method to solve the nuclear many-body problem from first principles has yet been developed; instead, a collection of efficient, truncated techniques are in common usage, which are reviewed extensively, e.g., in [3]. Estimates of the $0\nu\beta\beta$-decay NMEs are known to be correlated across isotopes, both within and across many-body methods, due to shared (and only partially understood) systematics of the many-body procedures [4]. These correlations are sometimes interpreted through the lens of "quenching," a generic overestimation of NMEs for both β and $2\nu\beta\beta$ decay, owing to the Gamow-Teller term. As Ref. [3] reviews in great detail, numerous underlying mechanisms for this systematic offset have been proposed but lack any conclusive evidence. Any or all nuclear-structure correlations, multinucleon weak currents, heavier isobars such as the Δ, pion-range properties of the nuclear medium, and more could be responsible for the effect, and as such it is unclear whether a similarly strong effect occurs for $0\nu\beta\beta$ decay.

Between 2018 and 2021, Cirigliano *et al.* surprised the $0\nu\beta\beta$ and nuclear theory communities with a series of works [5–8] purporting to show that even the two-body picture of $0\nu\beta\beta$ decay within conventional nuclear theory was, in fact, incomplete, containing its own intrinsic systematic offset. Employing an *ab initio* framework derived from chiral effective field theory (χEFT), these works claimed that a short-range, two-nucleon LNV interaction necessarily induces a contribution to the decay similar in magnitude to the contribution from the usual light neutrino exchange. There has been debate in the community about the implications of this result for NME computations performed in standard phenomenological nuclear frameworks and, in particular,

*Contact author: gwvg1e23@soton.ac.uk

whether the proposed "contact counterterm" is already accounted for by the nucleon-nucleon correlations included within modern many-body nuclear models. However, [8] argued concisely that the EFT-based argument still proceeds even if the involved nucleons are maximally correlated and so must be a distinct effect. To this point, there has been no published rebuttal.

Beyond such generic considerations, the $0\nu\beta\beta$-decay theorist is of course most interested in the quantitative impact of the contact counterterm on estimated NMEs. This question was partially answered in the most recent works by Cirigliano *et al.* [7,8], which implemented a matching analysis between low-momentum χEFT and high-momentum perturbative QCD in order to estimate the coefficient of the contact counterterm. Their final result, at renormalization point $\mu = m_\pi$, was

$$g_\nu^{NN}|_{NN} \simeq 1.32(50)_{\text{inelastic}}(20)_{\text{V}_\text{S}}(5)_{\text{parameters}} = 1.3(6), \quad (1.1)$$

where the largest error, about 38% relative error, arises from the choice to only account for elastic NN states in the intermediate stage of the process. The other acknowledged sources of error are the choice of a short-range nuclear potential V_S and other model-dependent parameters used to extend the χEFT result up to higher momenta, closer to the perturbative QCD regime so that a matching analysis is possible. The renormalization point is a kinematic scale at which one chooses to match theory parameters to physical observables; it is not unexpected that an unobservable coupling such at g_ν^{NN} should vary with this choice of scale, although observables should not.

This work aims to improve upon the 38% error from truncation to elastic states, by explicitly accounting for the lowest-lying collection of inelastic states, namely, $NN\pi$ states. Our result will therefore include both an adjusted coefficient for the contact counterterm and an improved error bar on the inelastic-state truncation, and at the same renormalization point will have numerical value

$$g_\nu^{NN}|_{NN+NN\pi} \simeq 1.40(20)_{V_S}(5)_{\text{parameters}}(3)_{\text{inelastic}} = 1.4(3). \quad (1.2)$$

To contextualize this result, and our methods, we will first give an overview of the mathematical and physical foundations of the work of Cirigliano *et al.* in Sec. II: chiral symmetry, χEFT, and nucleon-nucleon interactions within that framework. Section III will review the derivation of the contact counterterm from [8], including the aforementioned matching procedure for determining its coefficient. Finally, in Sec. IV, we will present our novel derivation of the contact counterterm coefficient accounting for both NN and $NN\pi$ intermediate states, ultimately delivering an updated estimate of g_ν^{NN} with improved uncertainty, and comment on the uncertainties that then dominate.

II. CHIRAL EFFECTIVE FIELD THEORY AND NUCLEAR FORCES

The experimental properties of both bound quark-gluon matter and hadronic scattering processes have constrained the gauge group of the strong interactions to be $SU(3)_{\text{color}}$. This fact has numerous nontrivial implications, not the least of which is that quarks and gluons should be confined into hadronic matter in systems below the Hagedorn temperature [9,10]. In studying QCD at low energies (MeV–GeV) relevant to *nuclear* processes, typically MeV–GeV-scale as opposed to TeV-scale collisions, our essential goal will be to make accurate predictions of hadronic properties, in particular the interactions of stable baryonic matter (protons and neutrons) via short-lived mesonic mediators. The running of the strong coupling leads to the breakdown of perturbation theory for low-energy QCD; i.e., we cannot hope to describe these hadronic interactions through some convergent series of diagrams involving their constituent quark and gluon field quanta.

However, nature has blessed QCD with a natural (chiral) symmetry, which is broken lightly enough that direct calculation of hadronic interactions is possible—with quantifiable perturbative uncertainties. The lightest mesons, pions, emerge as the Goldstone bosons of this approximate spontaneously symmetry breaking (SSB), and their interactions are severely constrained. The resultant χEFT, whose formulation is outlined in this section, will prove powerful enough to explain properties of nucleon-nucleon collisions from what are effectively QCD first principles. By including electroweak source terms in the χEFT Lagrangian, $0\nu\beta\beta$ decay can also be described at the nucleon level.

A. Chiral symmetry, SSB, and an effective Lagrangian

Chiral symmetry is most simply stated as the separation between the mass scale of the light quarks and that of the hadrons; with these light-quark masses taken to be 0, QCD classically enjoys an exact, global $U(3)_{\text{flavor}}$ symmetry. Furthermore, examining chirality eigenstates of the quark field reveals a copy of this flavor symmetry in each chirality sector, i.e., $U(3)_L \times U(3)_R \simeq SU(3)_L \times SU(3)_R \times U(1)_L \times U(1)_R$, where the latter factorization emerges from extracting a global phase from each $U(3)$ transformation.

This approximation of QCD still holds when we promote the $SU(3)_{\text{color}}$ symmetry of the quark fields to a local symmetry, introducing non-Abelian gauge self-interactions and a θ-term. However, the gauge interactions do constrain the collection of global flavor symmetries *after* quantization. The famous axial anomaly of $U(1)_A$ [11,12], with a violation inversely proportional to the number of colors, implies that $U(1)_A$ plays a role neither in chiral symmetry breaking nor in the eventual χEFT. The remaining Abelian symmetry $U(1)_V$, on the other hand, is preserved after quantization and corresponds to baryon-number conservation.

The action of chiral SSB is therefore restricted to $SU(3)_L \times SU(3)_R$ and its subgroup $SU(3)_V$ under which the QCD vacuum is invariant. Before exploring the consequences of this breaking, it is valuable to physically motivate its occurrence. Speaking phenomenologically, a $SU(3)_A$ symmetry on the baryon spectrum allows one to construct from any positive parity state a mass-degenerate negative parity state; however, such opposite-parity pairs are firmly absent from the observed baryon spectrum. Speaking theoretically, if the operator $\bar{q}q$ has a nonvanishing expectation value, which must be flavor independent in the chiral limit, the QCD vacuum is no longer invariant under axial symmetry $SU(3)_A$ [13]. Thus, the scalar singlet quark condensate $\bar{q}q$ provides not only an explanation, but a mechanism by which chiral symmetry can be spontaneously broken at zero temperature, yet be preserved/restored at higher energies. The pions, an isotriplet of pseudoscalars with masses 135.0 (π^0) and 139.6 MeV ($\pi^\pm$), are interpreted as the pseudo-Goldstone bosons resulting from this SSB, and their significant mass hierarchy to the next-lightest mesons, kaons ~490 MeV and ρ mesons ~770 MeV, may be taken as evidence of the chiral symmetry of QCD in action.

Some general comments about EFTs are in order. Although we have selected a symmetry-breaking pattern based on the theoretical and experimental properties of QCD, numerous quantum field theories could be constructed that obey this symmetry-breaking pattern. The natural question is then: which approximation is the best choice? A key result by Weinberg [14] is that the most general Lagrangian obeying the chosen symmetry will generate the most general complex-analytic S matrix that also obeys that symmetry, as well as being consistent with unitary time evolution and "cluster decomposition," where the latter refers to a conjected asymptotic independence between distant experiments. The conventional wisdom is that one cannot generically improve on this choice, as all specific physical content is encoded in the symmetry breaking. One is free to select the constituent fields most appropriate at the observed scale; in χEFT, these degrees of freedoms are hadrons rather than the more fundamental quarks and gluons. The resultant Lagrangian will also, in general, be nonrenormalizable, but this is in line with the expectation that the effective theory will only make accurate predictions within some range of scales. Even still, an infinite quantity of interaction terms appear in the Lagrangian, and there is no *a priori* method for determining which will contribute dominantly in all situations. As a result, part of constructing the effective theory is the choice of "power counting" scheme, usually in the form of a small expansion parameter. In χEFT, the standard and physically well-motivated choice is an expansion in $\frac{Q}{\Lambda_\chi} \simeq \frac{m_\pi}{\Lambda_\chi} \sim \frac{1}{7.5}$ for characteristic momentum Q and chiral symmetry-breaking scale $\Lambda_\chi \sim 1$ GeV [15].

We will not review the construction of the χEFT Lagrangian from the above principles in detail, but instead direct the reader to standard resources such as [13]. In brief, one constructs the simplest nontrivial realization of spontaneously broken chiral symmetry, building invariant interactions out of $SU(N)$-valued fields $U(x) = \exp\left(i\frac{\phi(x)}{F_0}\right)$ for pion fields ϕ and constant F_0. ϕ can be expanded $\phi = \phi_a\lambda_a$ over some basis $\lambda_{a=1,\ldots,n^2}$ of $SU(N)$, with standard normalization $\mathrm{Tr}(\lambda_a\lambda_a) = 2$; for $N = 2$, λ_a are the (isospin) Pauli matrices, and for $N = 3$ they are the Gell-Mann matrices. The chiral symmetry is promoted to a local symmetry by introducing two gauge fields l_μ, r_μ and an appropriate gauge-covariant spacetime derivative. Explicit chiral symmetry breaking is encoded in the light-quark mass matrix $\mathcal{M}$, and an argument due to Manohar and Georgi [15] shows that it is consistent to treat $\mathcal{M}$ as an auxiliary field and build the most general possible chiral-invariant Lagrangian accordingly, although it will always take on a constant value at evaluation.

If we are to apply χEFT to nuclear problems, baryonic fields must be introduced into the formalism. It is not necessary, for low-energy applications, for these baryons to be full-fledged dynamical fields, as processes in which baryons are created and destroyed are already beyond the range of validity of χEFT due to the heavy masses of baryons. Practically, this implies that our baryon realizations of the chiral symmetry need not be matrix valued; instead they can be isospin multiplet states N that transform under $SU(N)_V$ as $N \mapsto VN$. While previously we could only evaluate pion diagrams between QCD vacuum initial and final states, now these states can be (tensor products of) N states, providing a language for n-nucleon interactions.

Again, invariance under chiral symmetry specifies the most general set of interactions possible between baryons N and pion exponentials U. In nuclear applications, it is highly beneficial to take a "static approximation" in which the nucleon mass is thought of as very large and in which Dirac algebra reduces to Pauli algebra. Within the regime of our results, we implicitly take to be equivalent such formalisms as the heavy-baryon chiral perturbation theory of [16] or the simple neglect of a mass term for nucleons employed by [17,18].

Altogether, we have leading-order chiral Lagrangian

$$\mathcal{L}_2 = \frac{F_0^2}{4}\mathrm{Tr}\left(D_\mu U D^\mu U^\dagger\right) + \frac{F_0^2 B_0}{2}\mathrm{Tr}\left(\mathcal{M}U^\dagger + U\mathcal{M}^\dagger\right) + \bar{N}\left(i\gamma^\mu(\partial_\mu + \Gamma_\mu) - m + \frac{g_A}{2}\gamma^\mu\gamma_5 u_\mu\right)N, \tag{2.1}$$

where B_0 is an independent low-energy constant not determined by chiral symmetry, and where Γ_μ and u_μ are particular vector combinations of the pion fields and

their derivatives, to be defined as needed. F_0 may be related to the expectation value for the decay of a pion to the vacuum via an axial current [13],

$$\langle 0|A_a^\mu(0)|\phi(b)(p)\rangle = ip^\mu F_0 \delta_{ab} \tag{2.2}$$

and is thus known as the "pion decay constant." Normalization varies by factors of $\sqrt{2}$ depending on the choice of pion field normalization, but we follow [8,13] and the bulk of recent literature in taking the relation above to define F_0. Corrections from $\mathcal{L}_4$ and beyond distinguish between F_π for pions and F_K for kaons, and the experimental value $F_\pi = 92.1(8)$ MeV [19] includes these corrections. Therefore, in the following, we will follow [8] in writing F_π with an awareness that its value includes higher-order chiral corrections even though the rest of our calculation does not.

Since even the $l = 2$ Lagrangian contains infinitely many interaction terms, it is necessary to be able to truncate this series such that any resultant approximation error is bounded. This is the ethos of power counting: to estimate the magnitudes of interaction vertices, and therefore the magnitudes of the diagrams they compose, before needing to evaluate the high-dimensional integrals that those diagrams encode. Of course, these integrals must eventually be evaluated and divergences cured through appropriate regularization and the introduction of counterterms, but power counting allows for the choice of truncation to be made without the evaluation of any *unnecessary* integrals.

The more exact aspect of power counting is the bookkeeping of both dimensionless and dimensionful constants that arise at interaction vertices. In χEFT, this is quite straightforward. All terms in the U-field Lagrangian come with fixed constants, e.g., $\frac{F_\pi^2}{4}$ for all terms of $\mathcal{L}_2$, in combination with B_0 for the scalar/pseudoscalar symmetry-breaking terms; external fields, of course, may come with their own dimensionless factors that are defined during matching, but are fixed for every appearance of the field. Where unknown, is it standard to take such dimensionless constants to be of order $\mathcal{O}(1)$ or vary them over $\sim$2 orders of magnitude around 1. In the exponential realization of the spontaneously broken axial symmetry, each pion field ϕ also comes with a factor of $\frac{1}{F_\pi}$.

The less exact aspect of power counting is the choice of representative values for the spatial momenta and energies that emerge from derivatives of field operators. Physically, one can imagine that these virtual quanta have some characteristic scale for all processes within the range of validity of χEFT. Of course, no choice can be truly universal, and indeed we encounter in $0\nu\beta\beta$ a process that in part astounds expectations of a nice hierarchy of scales for nuclear processes. For now, we will proceed by letting the characteristic four-momentum scale of pions be $Q \sim m_\pi$, which is considered in ratio to the chiral symmetry-breaking scale Λ_χ; this is plausible since $r \sim \frac{1}{m_\pi}$ is the typical distance between nucleons. Any interaction vertex may then be assigned a label k denoting approximate magnitude $(\frac{Q}{\Lambda_\chi})^k$. Since our interactions will permit only low-energy pions and nucleons, we can write $Q \sim m_\pi \ll \Lambda_\chi \sim M_N$ [20] such that the ratio $Q/\Lambda_\chi \sim \frac{1}{7.5}$ is an appropriate small parameter [15].

We will revisit the chiral power counting in Sec. IV D, when we define the specific rules necessary for estimating the magnitudes of our $NN\pi$ contributions.

B. The problematic *NN* sector

Studies of two-nucleon (NN) interactions and bound-systems in χEFT, as distinct from the very broad literature on high-energy nucleon scattering, e.g., in colliders, have been motivated by the desire to perform further analysis of many-nucleon systems. The first steps in this direction were phenomenological treatments of two-nucleon potentials, which were derived as fits to measured scattering data and bound-state (deuteron) characteristics [21,22] and dominated the discipline until recently. The reasons are twofold for the broad acceptance [23] of effective chiral potentials over these phenomenological ones: they come with quantitative error bars owing to the truncation of the chiral ordering and are therefore systematically improvable; and they are explainable in terms of the broken chiral symmetry of QCD.

The key distinction between the NN sector of χEFT and the π and πN sectors is that NN interactions are known to be strong at low energies, and perturbation theory breaks down. While interactions involving pions, as Goldstone bosons, are "protected" by chiral symmetry, those between nucleons are not. Pion-range interactions such as one-pion exchange may obey the chiral power counting, but by the same logic, shorter-range nucleon interactions should also—this paradoxically leads to a description of nuclear physics where the interactions are not strong, where nuclear bound states are not captured, and indeed where nuclei do not appear at all [24]. More concretely, we will consider the effective NN Lagrangian of [18]

$$\mathcal{L}_{NN} = N^\dagger i\partial_t N - N^\dagger \frac{\nabla^2}{2M_N} N - \frac{1}{2} C_S (N^\dagger N)^2 - \frac{1}{2} C_T (N^\dagger \vec{\sigma} N)^2 \ldots, \tag{2.3}$$

which includes all interactions invariant under chiral symmetry and defines two undetermined four-nucleon low-energy constants (LECs), C_S and C_T.

Evaluating all leading-order (LO) diagrams between incoming and outgoing NN states $|\vec{p}\rangle$ and $|\vec{p}'\rangle$ gives the NN potential first elucidated by Weinberg [20],

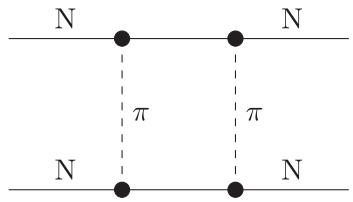

FIG. 1. The box diagram for two-pion exchange, shown in the text to be of similar order to the diagram for one-pion exchange.

$$\langle \vec{p}'|V_{NN}|\vec{p}\rangle = C - \tau_1 \cdot \tau_2 \frac{g_A^2}{2F_\pi^2} \frac{(\vec{p}-\vec{p}')\cdot\sigma_1(\vec{p}-\vec{p}')\cdot\sigma_2}{(p-p')^2+m_\pi^2}, \tag{2.4}$$

where $C = C_S - 3C_T$ for a ${}^1S_0 \to {}^1S_0$ transition. The derivation of the pion-exchange term is unimportant here, but will prove key to our argument in Sec. IV. From the chiral power counting and now manifestly from the evaluation between states, both terms of the LO potential are of order $\mathcal{O}(Q^0)$. Consider then the two-pion-exchange "box diagram" of Fig. 1. While the heavy-baryon NN propagator contributes Q^{-1}, the nonrelativistic loop integration contributes Q^3, and we find that the diagram is suppressed by Q^2 compared to one-pion exchange; the same result would hold with any or all of the pion exchanges replaced by NN contact interactions.

This power counting does not survive integration using the static nucleon propagator $\frac{i}{p_0}$, which diverges uncontrollably for the reason that the static baryon approximation cannot consistently hold while $p_0 \to 0$. To see this, it is enough to observe that there is no such thing as a soft nucleon in our chiral limit; all components of the on-shell nucleon four-momentum p cannot at once be 0.

NN pairs of kinetic energy E experience a pairwise Green's function

$$\langle \vec{p}|G_0(E)|\vec{p}\rangle = \frac{i}{E - \frac{p^2}{M_N}}, \tag{2.5}$$

whose enhancement can be estimated to be $\frac{M_N}{m_\pi}$ over the naive estimate by letting $|\vec{p}| \sim m_\pi$. The chiral power counting would have us take M_N to be of order Q^0, as $M_N \sim$ chiral symmetry-breaking scale Λ_χ, whereby the suppression of the doubly iterated NN interaction drops to Q^1, still allowing perturbative expansion. Weinberg argues [20] that large nuclear scattering lengths observed at low energies justify the treatment of M_N as a "free parameter," in the sense that its value is determined more directly by the number of colors in QCD than by the chiral flavor symmetry. Then taking $M_N \sim Q^{-1}$, while not quite numerically satisfying [24], is a compact way to bring the iterated NN interaction down to $\mathcal{O}(Q^0)$. In summary, the enhancement of pure nucleon intermediate states by both the pinch singularity and the separation of scales $M_N \gg m_\pi$ implies that it is equally probable, roughly speaking, for a pair of low-energy nucleons to propagate freely or to interact via the contact/pion-range interactions of $\mathcal{L}_{NN}$.

The resultant procedure for generating nuclear forces from χEFT has become ubiquitous in the literature. First, one produces an effective n-nucleon potential by evaluating only those interaction diagrams which *do not* include n-nucleon intermediate states, corresponding to joint Green's functions like $G_0(E)$. Then, one iterates this potential, for example, by numerically solving a complete Schrödinger equation with the potential as input [17]. This iteration may in some cases be treated as a formal geometric series, and indeed this is the approach that will prove efficient for the study of $0\nu\beta\beta$ decay. The great success of Weinberg's scheme is that it allows for the nonperturbative computation of n-nucleon forces within χEFT; the great drawbacks are that the power counting is not wholly consistent with the single-nucleon sector and that the extension to higher-order contact terms (with spacetime derivatives) is undefined [24].

Perhaps inadvertently, a toy model Weinberg used to demonstrate the above procedure in [20] emerged as a significant tool for modern nuclear theory. This is the pionless EFT ($\not{\pi}$EFT), which contains only the interactions of Eq. (2.3) at LO and supports only nucleonic degrees of freedom. As such, it is the simplest nuclear EFT valid at short-distance scales [24], and yet it is robust enough to indicate the renormalization procedure for diagrams containing two (or more) nucleons. We note that, because the $m_q \to 0$ limit is no longer meaningful, this theory cannot be said to obey even a broken chiral symmetry.

First we recall the demonstration by [20] of the one-loop renormalization of four-nucleon contact strength C, shown diagrammatically in Fig. 2. The integral to be evaluated is

$$\begin{aligned} T_2(E) &= C^2 \int \frac{d^3q}{(2\pi)^3} \langle \vec{q}|G_0(E)|\vec{q}\rangle \\ &= C^2 \int \frac{d^3q}{(2\pi)^3} \frac{1}{E - \frac{q^2}{M_N} + i\epsilon}, \end{aligned} \tag{2.6}$$

which in dimensional regularization with $D = 3 - \varepsilon$ gives [18]

$$T_2^{D=3-\varepsilon}(E) = -C^2(4\pi)^{-\frac{3-\varepsilon}{2}}\mu^\epsilon M_N(-M_N E - i\epsilon)^{\frac{1-\varepsilon}{2}}\Gamma\left(\frac{\varepsilon-1}{2}\right). \tag{2.7}$$

Letting $\varepsilon \to 0$ gives a finite regularized result, with $E = \frac{p^2}{M}$ for the reduced-mass NN system,

$$T_2(E) = \lim_{\epsilon\to 0} T_2^{D=3-\varepsilon}(E) = \frac{-iC^2 M_N|\vec{p}|}{4\pi}. \tag{2.8}$$

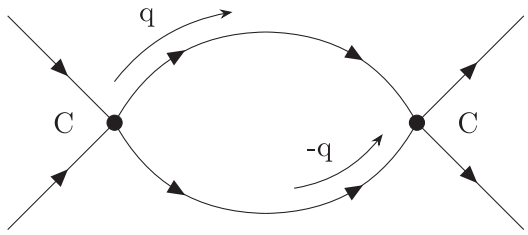

FIG. 2. The one-loop renormalization diagram of four-nucleon contact interaction C in pionless EFT ($\not{\pi}$EFT), as encoded in integral $T_2(E)$.

However, Weinberg does not perform the renormalization of C order by order in [20], nor even attempt it. Realizing that a chain of k contact loops is, in fact, separable into $k+1$ interaction vertices C and k bubbles $\frac{T_2(E)}{C^2}$, and applying the infinite geometric series property $\sum_{k=0}^{\infty} ar^k = a(1-r)^{-1}$ with radius of convergence $|r| < 1$, he writes

$$T_\infty(E) = \left[\frac{1}{C} - \int \frac{d^3q}{(2\pi)^3} \frac{1}{E - \frac{q^2}{M_N} + i\epsilon}\right]^{-1}, \tag{2.9}$$

which may be encoded diagrammatically, following [18], as

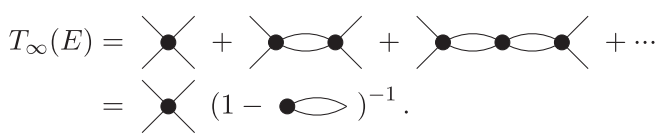

(2.10)

Then absorbing any infrared divergences in $T_\infty(E)$ by defining $C_R \equiv T_\infty(0)$, the geometric series simplifies to

$$T_\infty(E) = \left[\frac{1}{C_R} + \frac{iM_N|\vec{p}|}{4\pi}\right]^{-1}. \tag{2.11}$$

This result already contains all the key physics of NN scattering in $\not{\pi}$EFT, even if some loose ends need tying up. It can be matched directly to the so-called effective-range expansion, an experimentally determined [25] fit to NN-scattering phase-shift data,

$$i|\vec{p}| - \frac{4\pi}{M_N}\frac{1}{T(E)} = -\frac{1}{a} + \frac{1}{2}r_0 p^2 + \mathcal{O}(p^4), \tag{2.12}$$

where a is known as the scattering length, and r_0 is the effective range. Reference [18] quotes ${}^1S_0$ np scattering values $a = -23.714 \pm 0.013$ and $r_0 = 2.73 \pm 0.03$ fm from [26] as a point of reference. Evaluating with $T_\infty(E)$ gives

$$a = \frac{M_N}{4\pi} C_R, \qquad r_0 = 0. \tag{2.13}$$

Two important conclusions must be drawn. The first is that large scattering lengths, as are observed for shallow NN bound states (those near the unitarity limit), necessitate large contact couplings C_R in Weinberg's approach. The second is that the "natural" proportionality $C \sim \frac{4\pi}{M_N m_\pi}$ [24] implies $a \sim 1/m_\pi \sim 1.5$ fm; by defying this expectation, the experimental scattering length suggests that this effective theory formalism is not, in fact, consistent up to the m_π scale. Reference [18] cleanly shows the converse by working out $T(E)$ to next-to-leading order (NLO) in $\not{\pi}$EFT and observes a breakdown of the chiral expansion around $\Lambda \sim 35$ MeV, a factor of 5 below m_π.

In landmark work, Kaplan *et al.* [18] showed that both of these limitations can be overcome by an alternative regularization scheme, referred to as power-divergence subtraction (PDS) or alternatively as the Kaplan-Savage-Wise (KSW) scheme. First, one notes that the dimensionally regularized expression of Eq. (2.7), while finite at $\varepsilon = 0$ and therefore requiring no counterterm in the minimal subtraction MS scheme, does diverge linearly at $\varepsilon = -1$. The idea of PDS is to subtract this divergence with an additional counterterm, dependent on a regularization scale μ [27]. Then,

$$T_\infty^{\mathrm{PDS}}(E) = \left[\frac{1}{C(p^2,\mu)} + \frac{M_N(\mu + i|\vec{p}|)}{4\pi}\right]^{-1}, \tag{2.14}$$

which clearly matches the MS result if $\mu = 0$.

The above approach may seem arbitrary, and indeed surprising, given the familiar result that physical results obtained from different perturbative renormalization schemes are identical; only the sum of divergence and counterterm is observable. As a toy model, Ref. [28] instead argues that for δ potentials the physical amplitude can be dependent on the nonperturbative renormalization scheme, in particular, with different results for MS-dimensional regularization compared with cutoff regularization. Since the MS removal of divergences is a choice of renormalization scheme beyond the regularization of a loop integral, PDS achieves success by making an alternative choice more compatible with cutoff renormalization.

More precisely, bound states with large scattering lengths, also known as shallow bound states, are those where the kinetic and potential energies of the state nearly cancel [27]. However, neither the kinetic nor the potential energy is an independent observable, and so this cancellation is an unfortunate side effect of MS renormalization. The additional scale μ provides a sliding cutoff that separates the kinetic and potential terms and can be chosen at a value that provides a consistent power counting. Specifically, matching to the effective-range expansion now gives

$$C_R = \frac{4\pi}{M_N}\left(\frac{1}{a} - \mu\right)^{-1}, \tag{2.15}$$

so even for large scattering length a, the natural choice $\mu \sim m_\pi$ facilitates $C \sim \mathcal{O}(Q^{-1})$ as initially claimed, while $\mu = 0$ again reproduces the MS result. With renormalization complete, the power counting of all diagrams in the theory is well defined: the iteration of the lowest-order contact term C has been justified, while all higher-order vertices are counted perturbatively [27].

$\not{\pi}$EFT has proven useful to the nuclear community because large scattering lengths manifest in many physical systems beyond NN. For example, it has been applied to so-called halo nuclei whose valence nucleons largely have density outside the classical interaction radius [29]. Since a large scattering length in comparison to the interaction radius implies that the bound-state properties are driven by tunneling, an EFT approach need not probe many details of the internucleon potential to be descriptive of such systems [24]. $\not{\pi}$EFT has also successfully been applied to the Efimov effect [30], the observation that three particles with short-range attractions near threshold can induce long-range, specifically three-body interactions [31]. A review of practical applications of the pionless framework to few-nucleon systems may be found in [32]; these include electromagnetic form factors for the deuteron, deuteron formation in the context of big bang nucleosynthesis, and weak-deuteron interactions. While our focus is on the NN system as relevant to $0\nu\beta\beta$ decay, many of our χEFT conclusions will first be motivated within $\not{\pi}$EFT.

The value of including explicit pion fields and interactions in our model as opposed to the $\not{\pi}$EFT approach (beyond the realization of chiral symmetry) is that the EFT should be valid to higher energies—naively, up to the mass scale of the next "integrated-out" degree of freedom, the ρ meson.

Weinberg's power counting implied that a one-pion-exchange potential should be iterated to all orders, just as the four-nucleon contact potential was. The joint iteration of two potentials requires some careful algebra, detailed in [18]. Let us define the free, retarded two-nucleon Green's function as $\hat{G}_E^0 = [E - \hat{H}^0 + i\epsilon]^{-1}$ and the two-nucleon potential as $\hat{V}$, both of which will have simple actions on the space of momentum eigenstates $|\vec{p}\rangle$. Writing the geometric series

$$\hat{V} + \hat{V}\hat{G}_E^0\hat{V} + \hat{V}(\hat{G}_E^0\hat{V})^2 + \cdots = \sum_{k=0}^{\infty} \hat{V}(\hat{G}_E^0\hat{V})^k \equiv \hat{V} + \hat{V}\hat{G}_E\hat{V} \tag{2.16}$$

allows us to define an interacting Green's function $\hat{G}_E$. Reducing the geometric series gives the simple relations

$$\hat{G}_E = \frac{\hat{G}_E^0}{1 - \hat{G}_E^0\hat{V}}, \qquad \hat{G}_E^{-1} = (\hat{G}_E^0)^{-1} - \hat{V} = \left[E - \hat{H}^0 - \hat{V} + i\epsilon\right]^{-1}, \tag{2.17}$$

which relate the "dressed" and "undressed" Green's functions. It is then straightforward to uniquely define the scattering state $|\chi_{\vec{p}}\rangle$ as the eigenvector of $\hat{H}$ with eigenvalue $E = \frac{p^2}{M_N}$ or, equivalently, such that

$$\hat{G}_E^{-1}|\chi_{\vec{p}}\rangle = 0, \qquad |\chi_{\vec{p}}\rangle = (1 + \hat{G}_E\hat{V})|\vec{p}\rangle, \tag{2.18}$$

where the latter relation is consistent with factorizing the iterated potential amplitude as

$$\langle\vec{p}|\hat{V} + \hat{V}\hat{G}_E\hat{V}|\vec{p}'\rangle = \langle\vec{p}|\hat{V}|\chi_{\vec{p}'}\rangle = \int d^3r e^{-i\vec{p}\cdot\vec{r}} V(\vec{r})\chi_{\vec{p}'}(\vec{r}). \tag{2.19}$$

With these definitions in place, the strategy of [18] is to absorb the four-nucleon contact interaction C into $\hat{H}_0$ in the sense of $\not{\pi}$EFT, making use of the same explicit power series solution. $\hat{V}$ then consists only of the one-pion-exchange potential, and it is with (iterated) pion exchange that the scattering state $|\chi_{\vec{p}}\rangle$ and two-nucleon propagator $\hat{G}_E$ are therefore dressed. In $\not{\pi}$EFT, $|\chi_{\vec{p}}\rangle$ reduces to the plane-wave state $|\vec{p}\rangle$, $\hat{G}_E$ reduces to the free two-nucleon propagator $\hat{G}_E^0$, and the NN-scattering amplitude corresponds to Eq. (2.11) or Eq. (2.14) depending on subtraction scheme.

We can now precisely state how this framework changes when pions are included. First, the pion-exchange potential induces a correction in the NN contact coupling, $C \mapsto \tilde{C} = C + \frac{g_A^2}{2f_\pi^2}$. Iterating as before, the T matrix is [18]

$$T_\infty^{\chi\mathrm{EFT}}(E) = T_\infty^{\pi}(E) + [\chi_{\vec{p}}(0)]^2\left[\frac{1}{C} + \tilde{G}_E\right]^{-1}, \tag{2.20}$$

so long as one can evaluate scattering state $|\chi_{\vec{p}}\rangle$ at $\vec{r} = 0$ and compute $\tilde{G}_E = \int\int \frac{d^3q}{(2\pi)^3}\frac{d^3q'}{(2\pi)^3}\langle\vec{q}'|\hat{G}_E|\vec{q}\rangle$, the dressed two-nucleon propagator from $\vec{r} = 0$ to $\vec{r}' = 0$. $T_\infty^{\pi}(E)$ is the iterated one-pion-exchange contribution, i.e., the collection of terms containing no contact interactions. This series can be represented diagrammatically as follows, adapted from [18]:

$T_\infty^{\chi EFT}(E) =$ 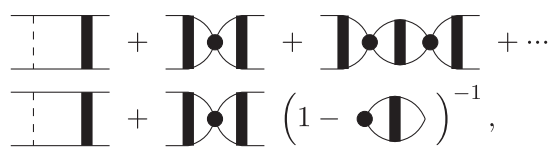 (2.21)

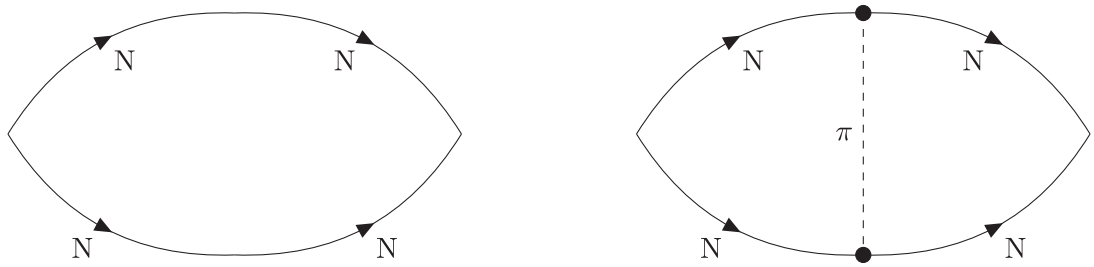

FIG. 3. Leading perturbative diagrams of chiral two-nucleon bubble $\tilde{G}(E)$, both of which contain regularizable divergences.

where

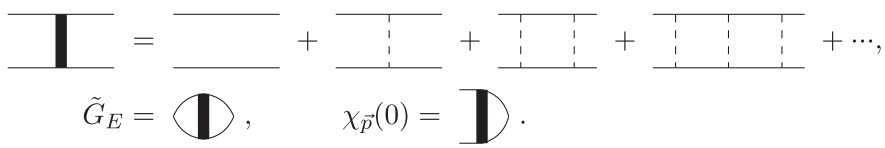

(2.22)

Green's function $\tilde{G}_E$ contains divergences from the first two diagrams in its perturbative series, shown in Fig. 3. These divergences must be regularized and absorbed into the renormalized interaction strength $\tilde{C}(\mu)$. It will be instructive to review the $\overline{\mathrm{MS}}$ regularization of these diagrams by [18], as an analogous computation for divergent diagrams containing a neutrino-exchange operator will later prove relevant to $0\nu\beta\beta$ decay. The goal is to examine the divergent parts of these diagrams only; the finite parts, while calculable through numerical solution of the relevant Schrödinger equation, will not be directly relevant to us. Because the S-wave solutions to this Schrödinger equation are independent of E as $r \to 0$, [18] sets $E = 0$ for convenience in these calculations.

As an example, we can explicitly evaluate the integral corresponding to the left of Fig. 3, the amplitude with no pion exchange,

$$\begin{aligned}
\langle \vec{r}'|\hat{G}_0^0|\vec{r}=0\rangle &= \iiint \frac{dr^3}{(2\pi)^3}\frac{dq^3}{(2\pi)^3}\frac{dq'^3}{(2\pi)^3}\langle \vec{r}'|\vec{q}'\rangle \frac{(2\pi)^3\delta^{(3)}(\vec{q}'-\vec{q})}{-\frac{q^2}{M_N}+i\epsilon} \\
&= 2\pi\int_0^\infty q^2 dq \int_0^\pi d\theta \cos\theta e^{-iqr\cos\theta}\frac{M_N}{q^2-i\epsilon} \\
&= 2\pi M_N \int_0^\infty dq \int_0^\pi d\theta \cos\theta e^{-qr\cos\theta} \\
&= \frac{2\pi M_N}{(2\pi)^3}\int_0^\pi d\theta \left[-\frac{1}{r}e^{-qr\cos\theta}\right]_{q=\infty}^{q=0} \\
&= -\frac{M_N}{4\pi r'},
\end{aligned} \tag{2.23}$$

where in the third line, we take $q \mapsto -iq$ by the Cauchy theorem in the absence of any poles off the imaginary q^2 axis. The limit $r' \to 0$ is then singular. Reference [18] shows that the irregular s-wave solution takes the following asymptotic form at small distances:

$$\lim_{r'\to 0} K_E^\lambda(r') \to \frac{M}{4\pi r'} - \frac{\alpha_\pi M_N^2}{4\pi}\ln(\lambda r) + \mathcal{O}(r\ln r), \tag{2.24}$$

where λ is a choice of separation scale between the regular and irregular Schrödinger solutions. Crucially, the $1/r'$ divergence here exactly cancels that from our first divergence perturbative diagram. Since $\overline{\mathrm{MS}}$ dimensional regularization reduces this diagram to 0 [18], the conclusion is that this asymptotic Schrödinger regularization agrees with dimensional regularization to $1/r'$ order.

What of the $\ln r'$ divergence? Ignoring finite contributions, direct integration of the amplitude $\langle \vec{r}'|\hat{G}_0^0\hat{V}_\pi\hat{G}_0^0|\vec{r}=0\rangle$

shown on the right of Fig. 3 gives a divergent term $\frac{\alpha_\pi M_N^2}{4\pi}\ln r'$, which again precisely cancels the divergence of $K_E^\lambda(r')$. $\overline{\mathrm{MS}}$ dimensional regularization at scale μ gives the divergent contribution $\frac{\alpha_\pi M_N^2}{4\pi}\ln(\frac{m_\pi}{\mu})$ identical to the Schrödinger divergence with $\lambda \mapsto \mu$ [18], albeit with a distinct finite part. Therefore, we learn two things: the renormalization of $\tilde{C}$ is scheme independent, and the kinematic point $\mu \sim m_\pi$ provides the most precise perturbative series, as expected from dimensional analysis.

Reference [18] promotes the numerical Schrödinger procedure for practical calculations in part because it is easily extended to higher-order chiral potentials. Indeed, this approach will also extend to the inclusion of neutrino potentials, but backed up with rigorous agreement to dimensional regularization. A clever way to see the manifest symmetry preservation of dimensional regularization is to observe [33] that the $D\pi DNDN^\dagger$ path-integral measure transforms nontrivially under chiral symmetry, requiring the introduction of a counterterm; this counterterm vanishes with dimensional regularization. Therefore, momentum cutoffs must be used with some caution, either by checking for symmetry violations postcalculation [34] or by including counterterms in the Lagrangian that cancel the effects of cutoff regularization at each chiral order [33].

In effect, the choice of PDS subtraction during regularization of the leading divergences has implied a new power counting for NN interactions in χEFT, in which pion exchanges are treated perturbatively with convergence guaranteed for momentum scales less than $\Lambda_{NN} \simeq$ 300 MeV [27]—the Kaplan-Savage-Wise power counting, in contrast to the Weinberg power counting. This approach has not been without controversy, shown in [35] to not converge for spin-triplet channels such as $^3S_1$, where two-pion-exchange contributions are large. One resolution to this quandary has been to apply KSW counting only in the $^1S_0$ partial wave, where the distinctive hard-core interaction between nucleons facilitates a perturbative treatment of pion exchanges [36]. Because the singular tensor component of the pion potential in higher partial waves seeded the failure of the KSW counting in these cases, a direct regularization of the pion propagator [37] is another route to perturbative pion physics beyond $^1S_0$. A more modern approach that has been shown to be scalable through N^{4}LO in the chiral expansion is a for-purpose regularization of contact interactions by nonlocal Gaussian cutoffs, while pion-range interactions are regularized at the level of the propagator—thus, semilocal momentum-space regularization [38]. Although the renormalization of pionic NN forces has been thoroughly computed in higher partial waves [39,40], this will play only a small role in our analysis—the enhanced contact term for $0\nu\beta\beta$ to be discussed will only appear in the $^1S_0$ partial wave.

We have now introduced all the primary tools and methodologies that facilitate [5] in treating the leading-order divergent diagrams of $0\nu\beta\beta$ in χEFT—these will prove essential to our refined estimate of the contact term. The unifying feature that binds all these EFT-driven nuclear computations together, whether in the symmetry-constrained framework of χEFT or the satisfying simplicity of $\not{\pi}$EFT, is that each and every observable quantity comes with a quantitative estimate of error. As in any EFT with a consistent power counting, this bound emerges from the truncation in the chiral expansion, which can be either treated somewhat approximately [41] or formalized as a Bayesian inference procedure [42–44] such that any prior-assumption dependence, regarding the coefficients of the chiral expansion of the observable, is controlled. Without such tools, nuclear theorists have historically had to rely upon variations of cutoffs and fit parameters to indirectly estimate the theoretical uncertainty of a computation. Although informative, such estimates are not statistically rigorous and, unlike an EFT power counting, do not allow the practitioner to anticipate at what scale higher-order mechanisms may become relevant to a process.

III. RENORMALIZATION ENHANCEMENT AND THE $0\nu\beta\beta$ CONTACT TERM

We have now overviewed the development of χEFT-derived nuclear potentials and, in particular, their application to shallow two-nucleon bound states. Now we will present the state of the field in applying this *ab initio* technology to the $0\nu\beta\beta$ transition in the two-nucleon system, following the seminal works by Cirigliano *et al.* [5–8]. To our knowledge, this is the first thorough review of the Cirigliano group's approach in print outside of their own publications, and as such we will aim to present the core results simply, but with an emphasis on how they represent a general viewpoint toward calculations of nuclear amplitudes [both Standard Model (SM) and beyond SM (BSM)], which is very much in the spirit of systematically improvable effective theories. We will also highlight the explicit and implicit assumptions that are manifest in this approach, the most numerically significant of which we will attempt to expand upon in Sec. IV.

The procedure for realizing the two-nucleon contribution to $0\nu\beta\beta$ decay at LO in the χEFT expansion has three stages. First, a "neutrino potential" corresponding to the $\Delta L = 2$ $NN \to NN$ operator of choice must be defined between any relevant NN partial waves, as first performed in [5]. Second, in the style of the NN scattering computations presented in Sec. 2.2 [18], this potential must be dressed with resummed contact and pion-exchange potential operators and renormalized where divergences appear to produce a consistent nonperturbative amplitude. The key result of [6] is that this renormalization enhances a doubly LNV dimension-nine contact counterterm to LO in the chiral power counting, which is not accounted for in standard phenomenological nuclear calculations of the decay. Third and finally, although the contact term contribution to the full two-nucleon

amplitude depends on an unknown LEC that will ultimately require input from lattice QCD (LQCD), its size may be estimated by a matching analysis as illustrated in [8].

A. Neutrino potential in χEFT

In order to evaluate the T matrix for an NN neutrino exchange, the neutrino-lepton vertex on a single nucleon must first be specified. Given that Lorentz invariance severely constrains the form of this vertex, an efficient approach is to first decompose the vertex into all permitted Lorentz structures, whose unknown kinematic dependence is encoded in form factors. In purely phenomenological approaches to nuclear theory, these form factors are derived from experiment using simple parametrizations such as dipoles; in an *ab initio* approach, each form factor is computable from χEFT.

Following [45], the effective single-β-decay Hamiltonian is

$$\mathcal{H}_\beta = \frac{G_F}{\sqrt{2}}[\bar{e}\gamma_\mu(1-\gamma_5)\nu_{e,L}]J_L^{\mu\dagger} + \text{H.c.}, \tag{3.1}$$

where the expression in square brackets is the usual leptonic weak current, which is left handed $(V-A)$—note that full details of neutrino potentials for "leptonic" BSM operators of all Lorentz structures may be found in [46]. Taking the impulse approximation for nucleon-level calculations, the hadronic current consists of six independent Lorentz structures [47],

$$J_L^\mu = J_V^\mu - J_A^\mu = \bar{N}\tau^+\Big[g_V(q^2)\gamma^\mu + g_M(q^2)\frac{\sigma^{\mu\nu}}{2M_N}q_\nu + ig_S(q^2)q^\mu - g_A(q^2)\gamma^\mu\gamma_5 - g_T(q^2)\frac{\sigma^{\mu\nu}}{2M_N}q_\nu\gamma_5 - g_P(q^2)q^\mu\gamma_5\Big]N, \tag{3.2}$$

where $\sigma^{\mu\nu} = \frac{i}{2}[\gamma^\mu, \gamma^\nu]$. Imposing hermiticity and time-reversal invariance, scalar and tensor terms $g_S(q^2) = g_T(q^2) = 0$, and the other form factors are guaranteed to be real [47]. It is convenient to write this current in the nonrelativistic limit [45]

$$J_{L,NR}^\mu = \bar{N}\tau^+\left[g^{\mu,0}g_V(q^2) + g^{\mu,i}\left(ig_M(q^2)\frac{\epsilon_{ijk}\sigma^j q^k}{2M_N} + g_A(q^2)\sigma^i - g_P(q^2)\frac{q^i\sigma\cdot q}{2M_N}\right)\right]N. \tag{3.3}$$

While the above separation is guided by phenomenological simplicity, symmetry properties also support the conserved vector-current (CVC) hypothesis and partially conserved axial-current (PCAC) hypothesis. CVC allows one to set $g_V(0) = 1$ regardless of host isotope and to assign dipole approximations to both g_V and g_M [45],

$$g_V(q^2) = g_V(0)\frac{m_V^2}{q^2 + m_V^2}, \tag{3.4}$$

$$g_M(q^2) = (1+\kappa_1)g_V(q^2). \tag{3.5}$$

PCAC connects the divergence of the axial current to measurable pion decay, allowing both g_P and g_A to be expressed in terms of the same phenomenological vertex form factor $F_{ANN}(q^2)$ accurate up to $q^2 \sim 1$ GeV,

$$g_A(q^2) = g_A(0)F_{ANN}(q^2)\frac{m_A^2}{q^2 + m_A^2}, \tag{3.6}$$

$$g_P(q^2) = \frac{2M_N g_A(q^2)}{q^2 + m_\pi^2}\left(1 - \frac{m_\pi^2}{m_A^2}\right), \tag{3.7}$$

which take the functional form of a dipole because they emerge from a single graph mediated by an axial meson. Sample values for the constants in this model are [45] $g_V = 1$, $g_A = 1.27$, $\kappa_1 = 3.7$, $m_V = 0.84$ GeV, and $m_A = 1.09$ GeV. Although the CVC/PCAC hypotheses predate the modern EFT approach and indeed QCD itself, their predictions generically hold at the first nontrivial leading orders of χEFT [13] with small corrections at higher chiral orders.

Separate from the determination of form factors, we can construct the neutrino potential by taking a product of two copies of the nonrelativistic one-body current $J_{L,NR}^\mu$, contracted over the index of exchange momentum q. Those product terms that do not evaluate to zero are collected in Table I, where notably the vector term decouples in the nonrelativistic limit, and $h_{(M,A)} = h_{(M,P)} = 0$ by symmetrization. Of these, only $h_{(V,V)}$ is a Fermi contribution and is purely so; $h_{(A,A)}$ is purely Gamow-Teller, and all other terms include both Gamow-Teller and tensor contributions. We define the Gamow-Teller and tensor contributions as the respective coefficients of Pauli inner product $\sigma_{12} \equiv \vec{\sigma}_1\cdot\vec{\sigma}_2$ and Pauli quadrupole moment $S_{12} \equiv 3(\vec{\sigma}_1\cdot\hat{q}\vec{\sigma}_2\cdot\hat{q}) - \sigma_{12}$.

Finally, to make contact with χEFT predictions for the couplings of nucleons to external currents, [46] computes the single-nucleon form factors at LO in the chiral expansion, obtaining

TABLE I. Allowed pairs of Lorentz structures, their contributions to the NN neutrino potential, and LO χEFT evaluation.

$h_{(\cdot,\cdot)}$	$\bar{N}_1\bar{N}_2\tau^{1+}\tau^{2+}(\ldots)N_2N_1$	LO χEFT
(V, V)	$g_V^2(q^2)$	1
(A, A)	$g_A^2(q^2)\vec{\sigma}_1\cdot\vec{\sigma}_2$	g_A^2
(P, P)	$g_P^2(q^2)\frac{1}{4M_N^2}[\vec{\sigma}_1\cdot\vec{q}\vec{\sigma}_2\cdot\vec{q}]q^2$	$\frac{g_A^2}{3}[S_{12}+\sigma_{12}]\frac{q^4}{(q^2+m_\pi^2)^2}$
(M, M)	$g_M(q^2)\frac{-1}{M_N^2}[\vec{\sigma}_1\cdot\vec{\sigma}_2q^2-\vec{\sigma}_1\cdot\vec{q}\vec{\sigma}_2\cdot\vec{q}]$	$\frac{(1+\kappa_1)^2}{3}[S_{12}-2\sigma_{12}]\frac{q^2}{M_N^2}$
(A, P)	$g_A(q^2)g_P(q^2)\frac{1}{2M_N}\vec{\sigma}_1\cdot\vec{q}\vec{\sigma}_2\cdot\vec{q}$	$\frac{g_A^2}{3}[S_{12}+\sigma_{12}]\frac{q^2}{q^2+m_\pi^2}$

$$g_V(q^2)=1,\qquad g_M(q^2)=1+\kappa_1=4.7,$$
$$g_A(q^2)=g_A=1.27,\qquad g_P(q^2)=-g_A\frac{2M_N}{q^2+m_\pi^2},\tag{3.8}$$

where κ_1 encodes the difference between the proton and neutron magnetic moments [47]. Form factors have also been derived at higher order in χEFT, for example, to next-to-next-to-leading order (NNLO) in [48], but these will be beyond the requirements of our precision. It is noteworthy that LO χEFT reproduces the pseudoscalar form factor "induced" by the axial coupling in PCAC. Then the resultant expression for each Lorentz product is given in the right-hand column of Table I. Factoring out global constants and the lepton bilinear as $V_\nu=(4G_F^2V_{ud}^2)\bar{u}(k_1)P_RC\bar{u}^T(k_2)\hat{V}_\nu$, we can now write the neutrino potential induced by light Majorana-neutrino exchange [45,46],

$$\begin{aligned}\hat{V}_\nu(q)&=\frac{\tau^{(1)+}\tau^{(2)+}}{q^2}[h_F(q^2)-\sigma_{12}h_{GT}(q^2)-S_{12}h_T(q^2)]\\&\simeq\frac{\tau^{(1)+}\tau^{(2)+}}{q^2}\left[1-\frac{2g_A^2}{3}\sigma_{12}\left(1+\frac{m_\pi^4}{2(q^2+m_\pi^2)^2}\right)\right.\\&\quad\left.-\frac{g_A^2}{3}S_{12}\left(1-\frac{m_\pi^4}{(q^2+m_\pi^2)^2}\right)\right].\end{aligned}\tag{3.9}$$

Coordinate-space realizations of the above are presented in [6]. Our primary interest will be the insertion of the neutrino potential between ${}^1S_0$ NN states, where $S_{12}=0$ and $\sigma_{12}=-3$, the above expression simplifying to

$$\hat{V}_\nu^{{}^1S_0}(q)=\frac{\tau^{(1)+}\tau^{(2)+}}{q^2}\left[1+2g_A^2+\frac{g_A^4m_\pi^4}{(q^2+m_\pi^2)^2}\right].\tag{3.10}$$

When $q\gg m_\pi$, the quantity in brackets has a limiting behavior of $1+2g_A^2$, while it is enhanced to $1+3g_A^2$ if $m_\pi\to\infty$ as in $\not{\pi}$EFT.

B. Resummation, the leading divergence, and its counterterm

With the NN potential corresponding to doubly LNV light neutrino exchange in hand, the naive expectation might be that the amplitude between well-defined NN states should be directly calculable. More precisely, if we write [6]

$$\mathcal{A}_\nu(E,E')=-{}_{{}^1S_0}\langle\Psi_{pp}(E')|V_\nu^{{}^1S_0}(q)|\Psi_{nn}(E)\rangle_{{}^1S_0}\tag{3.11}$$

for center-of-mass energies $E=p^2/m_n$ and $E'=p'^2/m_p$, with momentum transfer $\vec{q}=\vec{p}-\vec{p}'$, the naive expectation is that $\mathcal{A}_\nu$ should be finite for all physical kinematics and represent the LO perturbation theory of this weak operator, naturally regularized by the leading q^{-2} dependence of the neutrino potential. This expectation fails as a consequence of the enhanced contact counterterms required to renormalize $\mathcal{A}_\nu$, after the strong interactions intrinsic to Ψ_{NN} are accounted for.

In agreement with the analysis of shallow bound-state NN scattering reviewed in Sec. II B, the χEFT $|\Psi_{NN}\rangle$ differs from a free nucleon pair state $|\vec{p}\rangle$ by the iteration to all orders of both contact and pion-exchange terms in V_{NN}. In the ${}^1S_0$ channel, we therefore have three potentials to be combined,

$$\begin{aligned}{}_{pp,{}^1S_0}\langle\vec{p}'|V_\nu|\vec{p}\rangle_{nn,{}^1S_0}&=\frac{1}{(\vec{p}-\vec{p}')^2}\\&\quad\times\left[1+2g_A^2+\frac{g_A^4m_\pi^4}{((\vec{p}-\vec{p}')^2+m_\pi^2)^2}\right],\\{}_{{}^1S_0}\langle\vec{p}'|V_C|\vec{p}\rangle_{{}^1S_0}&=C,\\{}_{{}^1S_0}\langle\vec{p}'|V_\pi|\vec{p}\rangle_{{}^1S_0}&=-\frac{g_A^2}{4F_\pi^2}\frac{m_\pi^2}{(\vec{p}-\vec{p}')^2+m_\pi^2}.\end{aligned}\tag{3.12}$$

Although they appear two orders suppressed in the chiral expansion, we should have in mind the leading local $\Delta L=2$ structures in the χEFT Lagrangian [49],

$$\mathcal{L}^{(2)}_{\Delta L=2} = \frac{2G_F^2 V_{ud}^2 m_{\beta\beta}}{(4\pi F_\pi)^2}\left[\frac{5}{6}F_\pi^2 g_\nu^{\pi\pi}\partial_\mu\pi^-\partial^\mu\pi^- + \sqrt{2}g_A F_\pi g_\nu^{\pi N}\bar{p}S_\mu n\partial^\mu\pi^- + g_\nu^{NN}\bar{p}n\bar{p}n\right]\bar{e}_L C\bar{e}_L^T, \tag{3.13}$$

where $g_\nu^{\pi\pi}$, $g_\nu^{\pi N}$, and g_ν^{NN} are $\mathcal{O}(1)$ LECs corresponding to respective tree-level amplitudes $\pi^-\pi^- \to e^-e^-$, $n\pi^- \to p^+e^-e^-$, and $nn \to p^+p^+e^-e^-$. Because the latter is the trivial counterterm topology for our neutrino potential amplitude, we can make the ansatz

$${}_{pp,{}^1S_0}\langle\vec{p}'|V_\nu|\vec{p}\rangle_{nn,{}^1S_0} \mapsto {}_{pp,{}^1S_0}\langle\vec{p}'|V_\nu - 2g_\nu^{NN}(\mu_S)|\vec{p}\rangle_{nn,{}^1S_0} \tag{3.14}$$

to adjust for any regulator dependence of $\mathcal{A}_\nu$, where μ_S is the regulator scale that separates any short-range $\Delta L = 2$ physics.

The earliest evidence that the size of this counterterm is larger than anticipated by the chiral power counting comes from a $\not{\pi}$EFT analysis in [49]. The argument ultimately parallels that of [18] in the pure NN-scattering case; the large scattering length requires that any contact NN interaction be enhanced if the iteration of the interaction is to reflect nonperturbative nuclear physics. The g_ν^{NN} interaction itself cannot be iterated because it includes leptonic final states, but intuitively it can induce the iteration of both incoming and outgoing C interactions, resulting in two orders of enhancement. To see this explicitly, [49] employs dimensional regularization with the PDS scheme, with the result

$$g_\nu^{NN}(\mu_S) = (4\pi F_\pi)^2\left[\frac{M_N C_R(\mu_S)}{4\pi}\right]^2 \tilde{g}_\nu^{NN}(\mu_S), \tag{3.15}$$

where $\tilde{g}_\nu^{NN}(\mu_S)$ is $\mathcal{O}(1)$ and the quantity in square brackets is the inverse scattering length a^{-1}. Thus, $g_\nu^{NN} \sim \Lambda_\chi^2 a^2 \sim (\frac{Q}{\Lambda_\chi})^{-2}$. This amplitude and its counterterm diagram are shown in Fig. 4. To see how this back-of-the-envelope calculation generalizes to χEFT, [5,6] construct a geometric series in the style of [18]. Recall that, in the pure strong-interaction case, it was possible to decompose the T matrix as $T_\infty^{\chi\mathrm{EFT}}(E) = T_\infty^\pi(E) + \chi_{\vec{p}}(0)K_E\chi_{\vec{p}}(0)$, where $K_E \equiv [\frac{1}{C} + \tilde{G}_E]^{-1}$ is the iteration of the NN contact interaction to all orders, with each $\vec{r} = 0$ to $\vec{r}' = 0$ bubble dressed by iterated one-pion exchange. Analogously, an insertion of the LO V_ν can be dressed by contact strong interactions on either or both side, which are then summed coherently,

$$\mathcal{A}_\nu = \mathcal{A}_A + \chi_{\vec{p}'}(0)K_{E'}\mathcal{A}_B + \bar{\mathcal{A}}_B K_E\chi_{\vec{p}}(0) + \chi_{\vec{p}'}(0)K_{E'}\left(\mathcal{A}_C + \frac{2g_\nu^{NN}}{C^2}\right)K_E\chi_{\vec{p}}(0), \tag{3.16}$$

where all $\mathcal{A}$ implicitly have incoming E and outgoing E' two-nucleon kinematics, and the constant factors on g_ν^{NN} account for the two C interactions that are absorbed compared to the bubble diagram, as well as the symmetry of the counterterm. Because both the scattering states $\chi_{\vec{p}}(0)$ and K_E can be regularized in a scheme-independent manner [18], it is sufficient to separately evaluate and regulate $\mathcal{A}_{A,B,C}$ to obtain $\mathcal{A}_\nu$. As it happens, $\mathcal{A}_A$ and $\mathcal{A}_B$ are UV finite and so do not require regularization. This can be seen exactly in $\not{\pi}$EFT [6],

$$\mathcal{A}_A = \frac{1+3g_A^2}{2pp'}\tanh^{-1}\left(\frac{-2pp'}{p^2+p'^2}\right),$$
$$\mathcal{A}_B = \bar{\mathcal{A}}_B = \frac{iM_N}{4\pi}\frac{1+3g_A^2}{2p'}\log\frac{p+p'}{p-p'+im_\nu} + \mathcal{O}(m_\nu), \tag{3.17}$$

where dimensional regularization and the Feynman integral trick have been applied, analogous to Coulomb corrections to nucleon scattering in [50]. The apparent IR divergence in both cases is controlled by including some small neutrino mass $m_\nu \sim 0^+$ in the propagator. $\mathcal{A}_C$, on the other hand, exhibits a logarithmic divergence at $d = 4$, for example in the $\overline{\mathrm{MS}}$ regularization scheme [6,50],

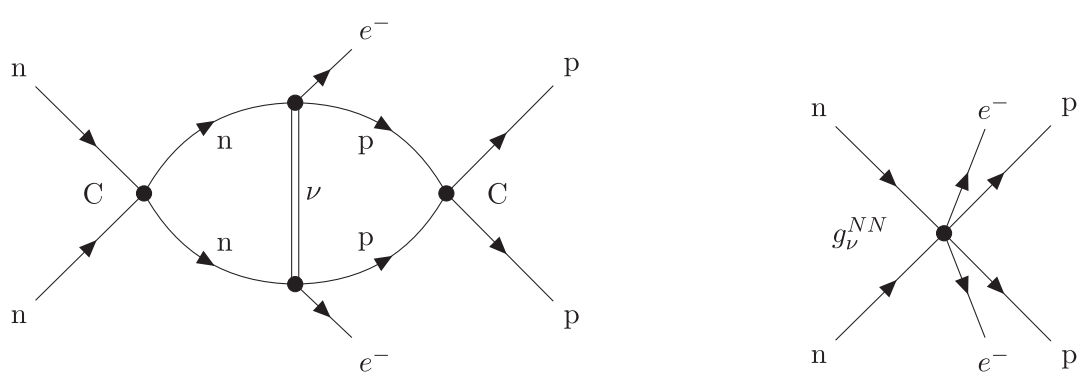

FIG. 4. Leading $\Delta L = 2$ NN-scattering amplitude (left) and its counterterm diagram (right) in pionless EFT ($\not{\pi}$EFT).

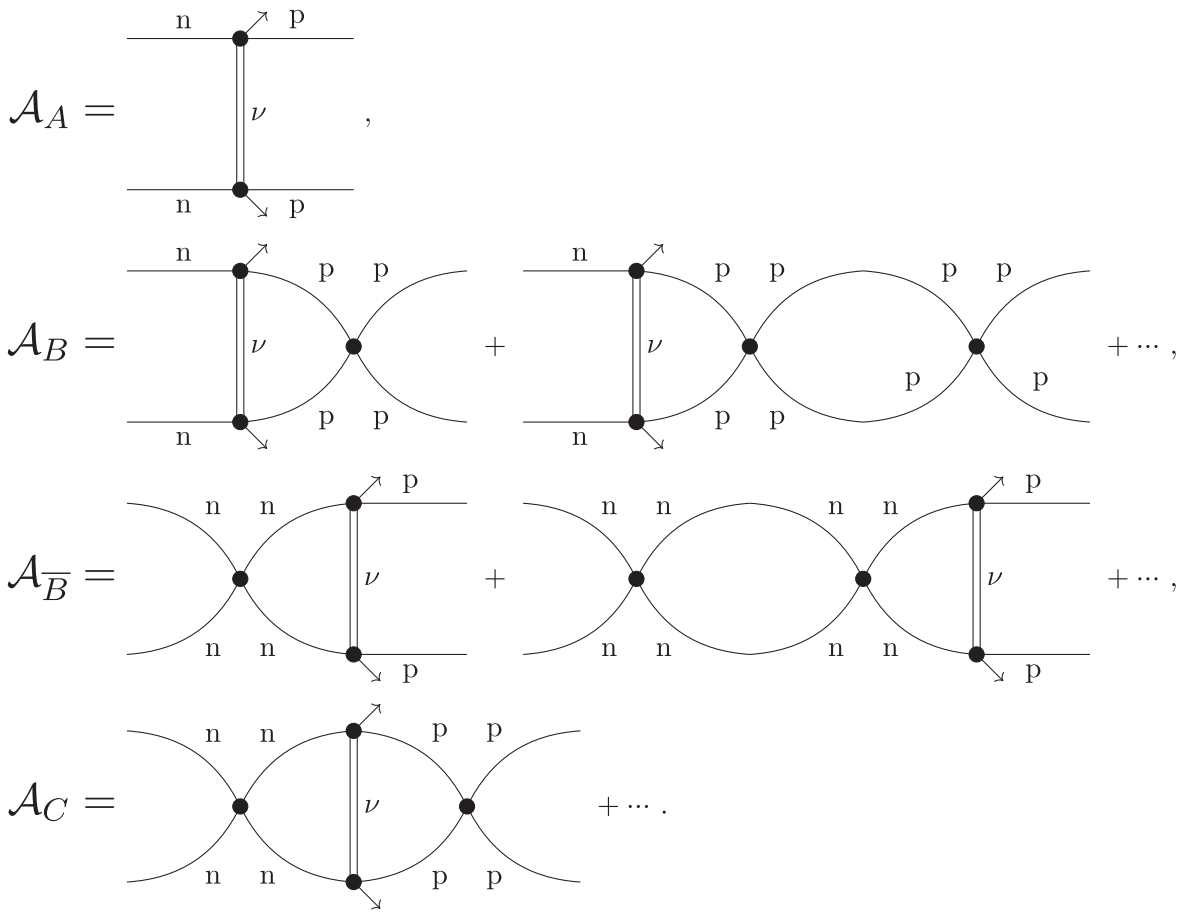

FIG. 5. Decomposition of NN $0\nu\beta\beta$ diagrammatic series in pionless EFT ($\not{\pi}$EFT), adapted from [6]. The leading (leftmost) $\mathcal{A}_A$ and $\mathcal{A}_B \simeq \mathcal{A}_{\bar{B}}$ diagrams are evaluated in the text and shown to be finite to all orders of contact iteration, while the leading diagram $\mathcal{A}_C$ is divergent and requires regularization through contact $\Delta L = 2$ diagram g_ν^{NN}.

$$\mathcal{A}_C = \frac{-M_N^2(1+3g_A^2)}{2\cdot(4\pi)^2}\left(\frac{1}{\varepsilon} - \gamma_E + \log 4\pi + 1 + \log\frac{\mu^2}{-(p+p')^2}\right), \tag{3.18}$$

where $\gamma_E \sim 0.577$ is the Euler-Mascheroni constant and μ is the chosen regularization scale. In alignment with the PDS subtraction scheme proposed in [18] and defined in Sec. II B, one can also observe that $\mathcal{A}_C$ is finite at $d = 3$, and so should be consistent with cutoff regularization—in other words, the calculation performed here should not fall victim to the same energetic cancellations that plagued the ${}^1S_0$ NN-scattering state.

Recalling that the scale-dependent amplitude was defined with normalization $\mathcal{A}_C(\mu) + \frac{2g_\nu^{NN}(\mu)}{C^2}$, the counterterm has β function

$$\beta_{g_\nu^{NN}} \equiv \frac{dg_\nu^{NN}}{d\ln\mu} = \frac{1+3g_A^2}{2}, \tag{3.19}$$

which can be satisfied, e.g., by coupling $g_\nu^{NN}(\mu) = \frac{1+3g_A^2}{2}\ln(\mu/\mu_0) + g_\nu^{NN}(\mu_0)$.

All of the above calculations have been performed in $\not{\pi}$EFT, and the critical reader might reasonably expect that proceeding to χEFT could substantively modify the structure of divergences. Diagrammatically, this corresponds to inserting an iterated pion exchange of the form in Eq. (2.22) into every two-nucleon reducible component of each diagram in Fig. 5. However, the difference is minor, for the convenient reason that each pion-exchange potential inserted between the two nucleons contributes $\int \frac{d^3k}{(2\pi)^3}\frac{1}{k^4}$ [6] and therefore improves the convergence of a diagram by one order. Therefore, only the leading diagram of type C with no pion exchanges could require an enhanced counterterm. Following [8], the divergent contribution is denoted $\mathcal{A}_C^{\sin g}$, while the convergent part of these diagrams and any pion-iterated convergent diagrams are collected in $\delta\mathcal{A}_C$.

$\mathcal{A}_C^{\sin g}$ itself is modified in passing from $\not{\pi}$EFT to χEFT in two ways. First, as before, the pion-exchange potential induces a correction in the NN contact coupling,

$C \mapsto \tilde{C} = C + \frac{g_A^2}{2f_\pi^2}$, wherever it appears in a diagram. Second, the coefficient of the neutrino potential recovers its induced pseudoscalar component: $1 + 3g_A^2 \mapsto 1 + 2g_A^2 + \frac{g_A^2 + m_\pi^2}{k^2 + m_\pi^2}$. For the same reason as the pion-exchange insertions above, this additional term can only improve the convergence of diagrams, and its effects are absorbed into $\delta\mathcal{A}_C$. $\mathcal{A}_C^{\sin g}$ is then recovered in χEFT by means of the simple substitution $1 + 3g_A^2 \mapsto 1 + 2g_A^2$, and the β function of g_ν^{NN} is similarly adjusted.

Overall, we see that the leading-order χEFT renormalization requirements on neutrino exchange in an NN system can be extracted from a $\not{\pi}$EFT analysis. We could interpret this to mean that the separation of nuclear forces into short- and pion-range interactions remains appropriate for a process such as $0\nu\beta\beta$ decay—but that some short-range physics specific to neutrino exchange is not captured by the naive truncation of the short-range diagrams and so must be encoded in g_ν^{NN}. Our more precise investigation of the extent to which short- and pion-range physics can be separated will play a central role in Sec. IV.

C. Quantitative estimates for the contact contribution

Having established that a sizable two-nucleon contact term enters into the χEFT description of $0\nu\beta\beta$ decay, it remains to quantify its size. A preliminary attempt at this estimation was made in [5], based on a comparison to the $I = 2$ charge-independence-breaking (CIB) NN process, with a more thorough and systematically improvable estimate made in [7,8], based on a generalization of the Cottingham approach to electromagnetic hadron-mass corrections [51]. In this section, we will summarize the former approach and detail the latter, which we will then expand upon in Sec. IV E.

1. Approximating g_ν^{NN} from CIB scattering data

In the midterm, precise LQCD computations of NN systems are expected to become possible to the effect that quantities like g_ν^{NN} may be extracted from a matching between $\not{\pi}$EFT/χEFT and LQCD [52]. At present, a substitute is to consider nuclear processes similar in topology to $0\nu\beta\beta$ decay for which experimental scattering data are available. Reference [5] makes the first such comparison with CIB, or isospin-breaking, NN scattering. Just as in the $\Delta L = 2$ case discussed above, the leading diagrams of this process require renormalization by a contact counterterm. Two such four-nucleon contact operators are available [5], which correspond to the insertion of currents with handedness LL/RR or LR, associated with respective LECs C_1 and C_2. In the electromagnetic case, the LH and RH currents are identical and so the process can only probe the sum $C_1 + C_2$, which [5] reports to have regularization scale dependence,

$$\frac{d(C_1 + C_2)}{d\log\mu} = 1 + g_A^2 \frac{m_{\pi^+}^2 - m_{\pi^0}^2}{e^2 F_\pi^2}. \tag{3.20}$$

Choosing $\mu = m_\pi$ as the natural regularization scale within χEFT, experimental scattering lengths imply the dimensionless value $\tilde{C}_1 + \tilde{C}_2 = (C_1 + C_2)[\frac{M_N \tilde{C}}{4\pi}]^2 \simeq 5.0$. For $0\nu\beta\beta$ decay, however, the weak-current insertion can only occur with LL handedness, and so $g_\nu^{NN} = C_1$. Thus, Ref. [5] makes the assumption that $C_1 = C_2$ to arrive at estimate $\tilde{g}_\nu^{NN} = \frac{\tilde{C}_1 + \tilde{C}_2}{2} \simeq 2.5$. More conservatively assuming that $|C_1|$ and $|C_2|$ differ at most by an order of magnitude, one can conclude that $-0.5 < \tilde{g}_\nu^{NN} < 5.5$.

Once g_ν^{NN} is determined, the magnitude of its contribution to the amplitude can be assessed by comparing the divergent amplitude $\mathcal{A}_{\Delta L=2}^\nu(\mu)$ and counterterm $\mathcal{A}_{\Delta L=2}^{CT}(\mu)$, the sum of which is seen to be scale invariant. Reference [5] finds that $R_{CT} \equiv \mathcal{A}_{\Delta L=2}^{CT}(\mu)/\mathcal{A}_{\Delta L=2}^\nu(\mu) \sim 10\%$ for $\mu \sim 350$ MeV, increasing to $R_{CT} \sim 30\%$ for $\mu \sim 2$ GeV, although beyond the chiral symmetry-breaking scale Λ_χ one can expect these results to come with significant uncertainties. Further computational estimates on $A = 6$, 12 nuclei affirm this substantial impact, with $R_{CT} \sim 25\%$–60% depending on the choice of CIB contact potential and the fit of $C_1 + C_2$.

2. Aside: The neutron-proton mass difference á la Cottingham

The second, more thorough estimate of the contact contribution by [7,8] is conceptually based on a classic dispersive calculation of the electromagnetic nucleon mass correction [51], which we will now briefly review.

The forward Compton scattering amplitude for a virtual photon with momentum $\vec{q}$ and polarization $\vec{\varepsilon}$ may be written

$$\varepsilon^\mu \varepsilon^\nu T_{\mu\nu}(\vec{q}) = i\pi\varepsilon^\mu\varepsilon^\nu \int d^4x e^{iq^\mu x_\mu} \langle N|\mathcal{T}\{j_\mu(\vec{x}), j_\nu(0)\} + \mathcal{T}\{j_\nu(\vec{x}), j_\mu(0)\}|N\rangle, \tag{3.21}$$

where $\mathcal{T}$ is the time-ordering operator and j_μ is the electromagnetic current. By inserting a complete set of intermediate nuclear states and performing the Fourier integrals in the nucleon rest frame, one obtains

$$T_{\mu\nu}(\vec{q}) = \frac{(2\pi)^4}{2} \sum_\kappa \langle N|j_\mu(0)|\kappa\rangle\langle\kappa|j_\nu(0)|N\rangle \left[\frac{\delta^{(3)}(k-q)}{k_0 - q_0 - M - i\epsilon} + \frac{\delta^{(3)}(k+q)}{k_0 + q_0 - M - i\epsilon}\right] + (\mu \leftrightarrow \nu). \tag{3.22}$$

Dispersive analysis relies on the examination of analyticity constraints when a real function $f(q_0)$ or $f(q^2)$ is continued to complex-valued q_0 or q^2. In general, two-point functions in quantum field theories may be written in the Källén-Lehmann spectral representation [53]

$$f(q^2) = \int_0^\infty ds \frac{\rho(s)}{s - p^2 - i0^+}, \tag{3.23}$$

where the analogous representation for $f(q_0)$ may be obtained by taking $\mathbf{q}^2$ as a fixed parameter. Unitarity requires that the spectral function $\rho(s)$ is positive definite, and it frequently may be decomposed as

$$\rho(s) = Z\delta(s - m^2) + \theta(s - s_0)\sigma(s), \tag{3.24}$$

where the pole term (first) represents a one-particle state of total energy m^2, and the branch-cut term (second) represents a continuum of multiparticle states beginning at threshold energy s_0. For a single nucleon in χEFT, $m^2 = M_N^2$ and $s_0 = (M_N + m_\pi)^2$ imply the following poles and branch cuts in q_0 [51]:

$$\begin{aligned} \pm q_0 &= \sqrt{M_N^2 + \mathbf{q}^2} - M_N - i\epsilon, \\ \pm q_0 &\geq \sqrt{(M_N + m_\pi)^2 + \mathbf{q}^2} - M_N - i\epsilon. \end{aligned} \tag{3.25}$$

Cottingham's essential observation is that the one-loop electromagnetic correction to the nucleon mass is simply the forward Compton scattering amplitude with the photon line contracted. This is not immediately useful. However, the absence of any poles or branch cuts from the ++ quadrant of the complex plane (including the new photon pole $\pm q_0 = \mathbf{q}^2 - i\epsilon$) allows for a rotation to Euclidean four-momentum, i.e.,

$$\begin{aligned} \Delta M &= \frac{i}{8\pi^2} \int d^4q \frac{\eta^{\mu\nu}}{q^\mu q_\mu - i\epsilon} T_{\mu\nu}(\vec{q}) \\ &= -\frac{1}{8\pi^2} \int d^4q \frac{\eta^{\mu\nu}}{\mathbf{q}^2 + q_0^2} T_{\mu\nu}(iq_0, \mathbf{q}). \end{aligned} \tag{3.26}$$

This result is very consequential, because the now-spacelike virtual "photons" of energy iq_0 are equivalent to those that mediate measurable electron-nucleon scattering. Reference [51] decomposes $T_{\mu\nu}(iq_0, \mathbf{q})$ into two independent Lorentz structures t_i, which can be further decomposed into elastic pole contributions f_i and inelastic cut contributions h_i (which must be integrated along the cut).

In modern incarnations of the Cottingham approach, elastic photon contributions are able to quantitatively capture the final result for the electromagnetic nucleon mass difference within 30% error [54,55]. Determinations of the inelastic contribution between dispersive and lattice methods disagree: in contrast to the elastic term $m_{p-n}^{\mathrm{el}} = 0.72(2)$ MeV approaching percent-level precision [8,55], the dispersive evaluation gives $m_{p-n}^{\mathrm{inel}} = -0.17(16)$ MeV [55], while the lattice gives $m_{p-n}^{\mathrm{inel}} = 0.28(11)$ MeV [8,56]. A resolution of this tension at some intermediate value would thus only improve the 30% error of an elastic-only calculation. It is noteworthy that calculations for electromagnetic meson-mass corrections do not show the same elastic dominance, with the vector and axial-vector resonances first applied by [57] delivering over 93% of the experimental pion mass difference in a modern calculation [58], while elastic diagrams give only 10%, the excess being negated by other inelastic corrections.

3. Extracting contact contribution from matching procedure

On the above grounds, [7,8] argue that there is no conceptual reason why a loop correction to a two-nucleon system cannot be treated according to Cottingham's approach, and furthermore that the nominal error from only including elastic contributions should be taken to be ~30%. A more rigorous dispersive derivation would likely verify and clarify this claim, but to date has not been attempted. In the following, we will see how the Cottingham representation of the two-nucleon $0\nu\beta\beta$-decay amplitude allows for a controlled estimate of the impact of the contact counterterm.

The construction begins by defining the factorized amplitude [Eq. (2.9) in [8]]

$$\mathcal{A} = (2\pi)^4 \delta^{(4)}(p_{e_1} + p_{e_2} + p_f - p_i)(4G_F^2 V_{ud}^2 m_{\beta\beta} \bar{u}_L(p_1) u_L^c(p_2)) \times \mathcal{A}_\nu, \tag{3.27}$$

where the hadronic amplitude $\mathcal{A}_\nu$ encodes the nuclear evaluation that is our focus. The neutrino propagator becomes that of a massless boson while mass effects are absorbed into $m_{\beta\beta}$. With the further assumption that the outgoing electron momenta are sufficiently similar that their Dirac algebra may be approximated as $\gamma^\mu\gamma^\nu \to \eta^{\mu\nu}$, $\mathcal{A}_\nu$ is reduced to the form necessary for the Cottingham approach,

$$\begin{aligned} \mathcal{A}_\nu &= 2 \int \frac{d^4k}{(2\pi)^4} \frac{\eta^{\mu\nu}}{k^2 + i\epsilon} T_{\mu\nu}^{(\nu)}(k, p_i, p_f) \\ &= 2 \int \frac{d^4k}{(2\pi)^4} \frac{\eta^{\mu\nu}}{k^2 + i\epsilon} \langle NN_f(p_f)| \int d^4r e^{ik\cdot r} \mathcal{T}\{J_\mu^L(r/2) J_\nu^L(-r/2)\} |NN_i(p_i)\rangle, \end{aligned} \tag{3.28}$$

where $T_{\mu\nu}$ is now a forward two-nucleon neutrino scattering amplitude. Just as for forward Compton scattering, one can insert a complete set of intermediate nuclear states and perform not just the Fourier integrals, but the k_0 integral as well, obtaining [Eq. (2.22) in [8]]

$$T^{(\nu)}_{\mu\nu}(k, p_i, p_f) = -\sum_{\kappa} \frac{\langle NN_f(p_f)|J^L_\mu(0)|\kappa(q)\rangle\langle\kappa(q)|J^L_\nu(0)|NN_i(p_i)\rangle}{q + E_\kappa(q) - \frac{1}{2}(p^0_i + p^0_f) - i\epsilon} \cdot \frac{1}{|k|}[\delta^{(3)}(k-q) + \delta^{(3)}(k+q)]. \tag{3.29}$$

$|NN_i\rangle$ and $|NN_f\rangle$ are scattering states, i.e., these two-nucleon wave functions must take into account the strong interactions, both short- and pion-range, which bind the system together. They can be described by making contact with the NN-scattering results discussed in [18,27] reviewed in Sec. II B, which imply

$$|NN_i\rangle(p_i) = (1 + \hat{G}(E)\hat{V})|\vec{p}_i\rangle = (1 + \hat{G}^0(E)\hat{T}^{(S)}(E))|\vec{p}_i\rangle, \tag{3.30}$$

for plane-wave state $|\vec{p}_i\rangle$, where the scattering operator is defined $\hat{T}^{(S)}(E) = \hat{V}(\mathbb{I} + \hat{G}^0(E)\hat{V})^{-1}$ in the notation of [8]. While both representations are convenient in their separation of the free and interacting components, the latter is perhaps more intuitive, because $\hat{T}^{(S)}(E)$ contains all iterated strong interactions, while $\hat{G}^0(E)$ simply encodes the free two-nucleon propagator at energy E.

This transition to a Euclidean spatial-momentum picture, and, in particular, the smoothness of the resultant single-current amplitudes and energy denominators, is the practical benefit of having treated $0\nu\beta\beta$ decay through the Cottingham lens. Again inserting complete sets of nuclear states between all defined operators, [8] decomposes the amplitude into four parts,

$$\begin{aligned}\mathcal{A}_\nu = \int \frac{d^3k}{(2\pi)^3}\Big[&\langle p_f|T^{(\nu)}(k)|p_i\rangle + \sum_{\kappa'}\langle p_f|\hat{T}^{(S)}(E')|\kappa'\rangle\langle\hat{G}^0(E')\rangle_{\kappa'}\langle\kappa'|\hat{T}^{(\nu)}(k)|p_i\rangle \\ &+ \sum_{\kappa}\langle p_f|\hat{T}^{(\nu)}(k)|\kappa\rangle\langle\hat{G}^0(E)\rangle_{\kappa}\langle\kappa|\hat{T}^{(S)}(E)|p_i\rangle \\ &+ \sum_{\kappa'}\sum_{\kappa}\langle p_f|\hat{T}^{(S)}(E')|\kappa'\rangle\langle\hat{G}^0(E')\rangle_{\kappa'}\langle\kappa'|\hat{T}^{(\nu)}(k)|\kappa\rangle\langle\hat{G}^0(E)\rangle_{\kappa}\langle\kappa|\hat{T}^{(S)}(E)|p_i\rangle\Big],\end{aligned} \tag{3.31}$$

where the Green's function expectation is $\langle\hat{G}^0(E)\rangle_\kappa = \frac{1}{E - E^0_\kappa + i\epsilon}$. This expression is directly useful, giving the full two-nucleon $0\nu\beta\beta$-decay amplitude so long as one can calculate matrix elements of the strong T matrix and the neutrino-exchange T matrix between relevant nuclear states. However, obtaining even those single-operator expectation values for a large selection of nuclear states is highly nontrivial. One simplification arises from the fortunate circumstance that only the neutrino-exchange potential in the ${}^1S_0$ partial wave requires a contact counterterm at LO in the chiral power counting [6], i.e., this entire procedure need only be performed with $|\vec{p_{i,f}}\rangle$ in that partial wave. However, this still leaves an unbounded nuclear state space from which intermediate states κ and κ' are to be selected. For this reason, [7,8] restrict to elastic intermediate states, i.e., pure $|NN\rangle$ states. Conservation of angular momentum then restricts both intermediate states purely to the ${}^1S_0$ partial wave.

If we take the spatial momentum to have magnitude $|\vec{k}| < m_\pi$ such that LO χEFT is certainly valid, then the above construction is exactly equivalent to the result (3.16) computed by [5,6]. Indeed, since $\mathcal{A}_{A,B,\overline{B},C}$ were distinguished from one another by the absence or presence of NN rescattering before and after the insertion of the neutrino-exchange potential, the four terms in Eq. (3.16) exactly correspond to the decomposition of Eq. (3.32). As a consequence, the target of this matching-based analysis need only be the divergent part of $\mathcal{A}_C = \mathcal{A}^{\rm div}_C + \delta\mathcal{A}_C$.

After much preamble, we can now define the matching procedure conceived by [7,8]. As presented earlier and in [6], $\mathcal{A}^{\rm div}_C$ was calculated in LO χEFT to have real component

$$\mathcal{A}_C^{\rm div}(\mu_\chi) = \left(\frac{4\pi}{M_N}\right)^2\left[-\frac{1+2g_A^2}{2} + \int_0^{\mu_\chi} dk a_\chi(k)\right]$$
$$= \left(\frac{4\pi}{M_N}\right)^2\left[-\frac{1+2g_A^2}{2} - \int_0^{\mu_\chi} dk (1+2g_A^2)\frac{1}{k}\theta(k-2p)\right], \tag{3.32}$$

where the role of μ_χ is apparent as a cutoff on the validity of this EFT amplitude. It is precisely the ignorance of short-range physics beyond μ_χ that our enhanced contact term parametrizes. As such, [8] conceives of a hypothetical $\mathcal{A}_C^{\rm exact}(\mu_\chi)$ that integrates accounts for all $0 < k < \infty$ and is finite. χEFT, of course, cannot provide such an amplitude; however, QCD may be treated perturbatively at scales above some $\Lambda \sim 1.5$ GeV, allowing us to compute some partial amplitude $\mathcal{A}_C^>$ such that

$$\mathcal{A}_C^{\rm exact} = \mathcal{A}_C^< + \mathcal{A}_C^> = \int_0^\Lambda dk a_<(k) + \int_\Lambda^\infty dk a_>(k). \tag{3.33}$$

Perturbative methods are valid for QCD in the $|k| > \Lambda$ regime because asymptotic freedom ensures that the effective strong coupling is small, i.e., $\alpha_s \ll 1$ [59]. If we were modeling the interactions of free, high-energy quarks and gluons, direct perturbative computation would be largely sufficient. However, our quarks and gluons are quanta of a nuclear (ground) state, as opposed to the QCD vacuum, and so our model clearly requires input from nonperturbative nuclear scale around $\Lambda_{\rm QCD}$. In fact, even in the free vacuum case, QCD vacuum condensates of both quarks and gluons are present due to the nonlinearities of the QCD Lagrangian [59], and some nonperturbative input is eventually necessary.

A clean way to decompose these perturbative and nonperturbative QCD inputs in the case of a two-point correlator is by constructing a Wilsonian operator product expansion (OPE) [60,61], first performed in this context by [62]. Formally, this expansion may be written

$$\lim_{x\to 0}\langle 0|\mathcal{T}\{\mathcal{O}_1(x)\mathcal{O}_2(0)\}|0\rangle = \sum_d C_d(x)\langle 0|\mathcal{O}_{(d)}(0)|0\rangle, \tag{3.34}$$

where $\mathcal{T}$ is the time-ordering symbol, $\mathcal{O}_{1,2}$ are two particular local operators, $\mathcal{O}_{(d)}$ are (typically other) local operators of dimension d, and C_d are their respective coefficients. Note that there may well be distinct operators $\mathcal{O}_{(d)}$ of the same dimension requiring independent coefficients, although this will not occur in our case. There is typically a unit operator $\mathcal{O}_0$ with vacuum expectation value 1 (in our case it will instead have expectation $\langle NN_f|\bar{u}_L\gamma_\mu d_L \bar{u}_L\gamma^\mu d_L|NN_i\rangle$), such that $C_0(x)$ encodes the usual perturbative expansion of QCD diagrams. This perturbative series is only the first term in the summation over vacuum condensates $\langle 0|\mathcal{O}_{(d)}(0)|0\rangle$ seen in Eq. (3.34), whose lowest-order nontrivial terms include the quark condensate $\bar{\psi}\psi$ and the gluon condensate $G^a_{\mu\nu}G^{a,\mu\nu}$. We will follow [8] in restricting ourselves to $d = 0$, but note that the subleading corrections would arise from the gluon condensate. Implicitly, the separation between perturbative and nonperturbative QCD has occurred at a chosen scale μ, where physics at scales greater than μ is explicitly calculated in coefficients $C_d(x)$, and physics at scales less than μ is absorbed into the QCD vacuum condensates.

A full derivation of $C_0(k^2)$ leads to the following amplitude truncated at the first term of the OPE [8]:

$$\mathcal{A}^> = \frac{3\alpha_S}{2\pi}\langle NN_f|\bar{u}_L\gamma_\mu d_L \bar{u}_L\gamma^\mu d_L|NN_i\rangle \int_\Lambda^\infty dk \frac{1}{k^3}, \tag{3.35}$$

where the condensate contains all contributions softer than Λ. From Eq. (3.13), those contributions are encoded in the local LECs $g_\nu^{\pi\pi}, g_\nu^{\pi N}, g_\nu^N \sim O(1)$, which together contribute a factor $\frac{2}{C^2}(g_\nu^{NN} + \frac{g_A^2}{2}(\frac{5}{6}g_\nu^{\pi\pi} - g_\nu^{\pi N}))$. For simplicity and since g_ν^{NN} is poorly constrained, [8] elects to set the latter term in parentheses to zero, absorbing any inaccuracy into the uncertainty assessment of g_ν^{NN}. Because the share of $\mathcal{A}_C$ from the $k > \Lambda$ regime is vanishingly small compared with uncertainties of this approach, only a very unnaturally large g_ν^{NN} or other LECs would confound this assumption. Altogether, the integrand for the matching analysis is therefore written

$$a_>(k) = \frac{3\alpha_S}{\pi}\frac{g_\nu^{NN}}{C^2}\frac{1}{k^3}. \tag{3.36}$$

Model-independent information about $a_<(k)$ is not so readily available as it is about $a_>(k)$ in the perturbative QCD limit. A multitude of hadronic states not included in χEFT are accessible between μ_χ and Λ, including strange pseudoscalar mesons η, η' and $K^{+,0,-}$, vector mesons $\rho^{+,0,-}$, ω, ϕ, and baryonic $\Delta^{++,+,0,-}$ resonances. Rather than account for these effects directly, [8] treats the intermediate momentum regime as a perturbation on the low-momentum regime already computed in χEFT. To the extent that nucleons are still appropriate degrees of freedom for the interaction, the topology of the bubble diagrams and therefore the decomposition equation (3.32) is retained. Thus, $\mathcal{A}_C^<$ can be obtained from $\mathcal{A}_C^{\chi\rm EFT}$ by some appropriate

generalizations of $\hat{T}^{(S)}(E)$ and $\hat{T}^{(\nu)}(E)$, i.e., by introducing form factors, which are accurate up to $\Lambda \sim 1.5$ GeV.

The modification of $\hat{T}^{(\nu)}(E)$ can be expected to proceed smoothly, since for larger momentum exchange the NN state should be at least as separable as in the χEFT regime. Therefore nucleon-level form factors at the neutrino vertices are an appropriate generalization; [8] chooses to include the form factors for all pairs of Lorentz structures compatible with the product of two left-handed currents: AA, PP, AP, and MM. However, the induced pseudoscalar current only contributes to the convergent part of the amplitude, so we need not include it in $\mathcal{A}_C^<$. Therefore this form factor contribution amounts to a substitution,

$$(1 + 2g_A^2) \mapsto g_V^2(k^2) + 2g_A^2(k^2) + \frac{k^2}{2M_N^2} g_M^2(k^2), \tag{3.37}$$

where the form factors were defined in Sec. III A and depend on scales $\Lambda_V = 0.84$ and $\Lambda_A = 1.0$ GeV. Reference [8] demonstrates that the dependence on the amplitude on these precise scales is a "by far subdominant uncertainty" in contrast to, for example, the truncation of nuclear states.

The modification of $\hat{T}^{(S)}(E)$ is somewhat more subtle, because it directly relies upon a choice of phenomenological short-range potential between nucleons. These data are encoded in a so-called "half-off-shell" form factor on the iterated strong-interaction vertex represented by $\hat{T}^{(S)}$, i.e., $T_<^{(S)}(q,p) \equiv T^{(S)}(p,p) \times f_S(q,p)$. Part of the appeal of this parametrization is that $f_S(q,p) = 1$ in LO χEFT [8], so the form factor will specifically encode deviations from the low-momentum amplitude. Simply extending χEFT to NLO gives

$$f_S^{\chi\mathrm{EFT}} = 1 - \frac{C_2}{2C}(p^2 - q^2), \tag{3.38}$$

where the two form factors together deliver a real-valued suppression factor $r^{\mathrm{NLO}}(k) = 1 - \frac{8C_2}{M_N C^2} k$ to $\mathcal{A}_C^<$. The ratio of constants C_2/C^2 evaluates to 0.52 in $\not{\pi}$EFT and 0.38 on χEFT. To obtain more precision at momenta up to $\Lambda \sim 1.5$ GeV, Ref. [8] calculates the form factor $f_S(q,p)$ using three popular phenomenological NN potentials: the Kaplan-Steele potential [63], the Reid potential [64], and the AV18 potential [65], which match very well to NLO χEFT below $k = 200$ MeV, and all show a suppression $r(k) \sim 0.1$ before $k = 400$ MeV. Model dependencies for momenta larger than this are thus highly suppressed in their contribution to the overall amplitude, whose integrand is written

$$a_<(k) = -\left(g_V^2(k^2) + 2g_A^2(k^2) + \frac{k^2}{2M_N^2} g_M^2(k^2)\right) \times \frac{r(k)}{k}\theta(k - 2p). \tag{3.39}$$

$a_\chi(k)$, $a_<(k)$, and $a_>(k)$ are plotted in Fig. 13, adapted from Fig. 6 in [8], alongside the corrected integrands from the $NN\pi$ analysis in Sec. IV D. These pieces together are sufficient to estimate the size of the enhanced contact counterterm $g_\nu^{NN}(\mu)$, since the scale-invariant amplitude $\mathcal{A}_C(\mu) + \frac{2g_\nu^{NN}(\mu)}{C^2}$ should have equal value to our constructed $\mathcal{A}_C^{\mathrm{exact}} = \mathcal{A}_C^< + \mathcal{A}_C^>$. Here we note some ambiguity in the notation; the constant g_ν^{NN} that appears in the OPE is more precisely the $\mu \to \infty$ limit of $g_\nu^{NN}(\mu)$, and performing the matching analysis is equivalent to determining the action of the renormalization group on this constant. In terms of the integrands [8],

$$2g_\nu^{NN}(\mu) = \frac{1 + 2g_A^2}{2} - \int_0^\mu dk a_\chi(k) + \int_0^\Lambda dk a_<(k) + \int_\Lambda^\infty dk a_<(k), \tag{3.40}$$

which is plotted as the pure NN comparison point for our later $NN\pi$ analysis in Figs. 14 and 15 for a range of matching scales Λ, where the dependence on the latter is comfortingly weak. Reference [8] selects the value $g_\nu^{NN}(\mu = m_\pi) = 1.32$ as a representative value, which is essentially independent of Λ between 1 and 4 GeV. However, this number by itself is not especially meaningful, because it is specific to a decomposition of the amplitude into convergent and divergent parts, i.e., the MS/PDS regularization scheme. Section 7 of [8] performs the analogous matching calculation for several choices of momentum and coordinate-space cutoff regulators. The material point is that the relative importance of light neutrino exchange and the contact counterterm is scheme dependent and therefore nonphysical; however, one can expect that the total $\mathcal{A}_\nu$ will be scheme independent and, in general, have been modified with a significance similar to the ~15% adjustment seen in the MS scheme. To facilitate other groups in evaluating the contact contribution within their own chosen regularization scheme, [7,8] provide "synthetic data" by computing $\mathcal{A}_\nu$ in full at a kinematic point relevant to the many-body nuclear community, $p = 25$ and $p' = 30$ MeV.

However, our primary interest is in the two-nucleon matrix element and, in particular, the improvement of the leading uncertainty on the matching calculation that arises from truncating the sum over intermediate nuclear states to elastic NN states only. Reference [8] demonstrates that this uncertainty is dominant primarily by constraining all other sources of uncertainty. The impact of model-dependent form factors for the strong interactions in the intermediate momentum range is assessed by parameter variation and contributes an uncertainty of ± 0.2 to δg_ν^{NN}, only ± 0.05 of which arises from the less well-described but suppressed region $0.4 < k < 1.5$ GeV. A further ± 0.05 (at most) enters δg_ν^{NN} from numerical parameter selections, especially the scales $\Lambda_{A,V}$ entering the single-nucleon form factors.

However, a rough evaluation of one divergent diagram with a $NN\pi$ intermediate state, which can be interpreted as a leading inelastic correction, contributes between -0.1 and 0.35 to δg_ν^{NN}; this, of course, is just one of numerous possible diagrams containing the first accessible inelastic state, and [8] consequently assigns an uncertainty of ± 0.5 in the absence of further information. This source of uncertainty, its more precise quantification, and steps toward its improvement will be the focus of the following section.

IV. QUANTIFYING THE $NN\pi$ INTERMEDIATE STATE

In the Cottingham procedure for studying loop corrections from nuclear operators, the superposition principle directly requires the completeness of the intermediate set of nuclear states. Taking a perturbative viewpoint of the nuclear state space, these intermediate states need not have the same particle content as the external NN states—such states are called inelastic. At the scales well modeled by χEFT, this will mean that dynamical fluctuations of the nucleon field induce fluctuation quanta in "nearby" strongly interacting fields, most accessibly the pseudo-Goldstone pion fields. Of course, all this is a convenient perturbative realization of systems that are more precisely nonperturbative bound configurations of QCD fields, where, as the particle number of a nucleon state is a distribution rather than a single value, the line between elastic and inelastic nuclear states is blurred. We are able to take advantage of a truncation between elastic and inelastic nuclear states in the case of $0\nu\beta\beta$ for two fortunate reasons: the bulk of the neutrino-momentum transfer occurs well below energy scales that probe the internal structure of nucleons, and chiral symmetry is sufficiently broken such that, roughly speaking, momentum at the order of the transferred neutrino is required to induce even a single (virtual) excitation of the pion field.

For these same reasons, we take a further truncation of inelastic nuclear states between $|NN_\pi\rangle$ and $|NN_\pi+\rangle$ (all other inelastic states) to be well defined. As [8] is careful to note, the two-particle kinematics of this process greatly complicate a direct relation between elastic states of the forward scattering amplitude and the Cottingham-style loop correction, and we accept the same limitation in framing our $|NN_\pi\rangle$ intermediate states. We retain the state decomposition of [8] from Eqs. (3.29) and (3.32), where $|\kappa\rangle, |\kappa'\rangle$ now are summed over both elastic and $NN\pi$ states. We will also refer to the leading elastic correction as the difference $\Delta\mathcal{A}_\nu^{NN\pi} = \mathcal{A}_\nu - \mathcal{A}_\nu^{NN}$. $\Delta\mathcal{A}_\nu^{NN\pi}$ receives contributions from diagrams (1) where only one of $|\kappa\rangle, |\kappa'\rangle$ is inelastic (distinguished by isospin breaking) and (2) where both $|\kappa\rangle$ and $|\kappa'\rangle$ are inelastic.

A significant complication regarding $NN\pi$ states is that both angular momentum and isospin may now be distributed between the component particles in multiple ways, and strong scattering $\hat{T}^{(S)}$ will transfer these quantum numbers. We cannot therefore retain the ${}^1S_0$ partial wave or some $NN\pi$ equivalent throughout our analysis as [8] does, and the principles of angular momentum, isospin, and parity conservation will constrain our result via selection rules.

We will proceed as follows. First, the role of selection rules in constraining the angular momentum and isospin properties of our intermediate states will be reviewed. Then, $\langle NN|\hat{T}^{(S)}|NN\pi\rangle$ will be characterized within χEFT and compared to the broader literature on threshold pion production from nucleon pairs. $\langle NN|\hat{T}^{(\nu)}|NN\pi\rangle$ and $\langle NN\pi|\hat{T}^{(\nu)}|NN\pi\rangle$ will also be characterized with the derivation of $\pi\pi$ and πN neutrino potentials within χEFT. Combining these two building blocks will lead to the complete diagrammatic structure of the divergent contributions to $\Delta\mathcal{A}_\nu^{NN\pi}$. Naive dimensional analysis *á la* Weinberg will be used to estimate the size of each diagram in comparison to $\mathcal{A}_\nu^{NN}$; finally, the leading divergences will be evaluated in the dimensional regularization scheme such that a numerical adjustment to the elastic computation of contact term g^{NN} can be claimed.

A. Selection rules for $NN \to NN\pi$ transitions

An excellent description of the selection rules for $NN \to NNx$ transitions is given in the review [66] and the thesis [67]. First, let us state the relevant quantum numbers. Two-nucleon systems may have total spin $S = 0,\ 1$, total isospin $T = 0,\ 1$, and total orbital angular momentum $L = 0, 1, 2, \ldots$, while a pion in an $NN\pi$ system has spin $S_\pi = 0$, total isospin $T_\pi = 1$, and angular momentum $l_\pi = 0, 1, 2, \ldots$ about the center of mass of the NN component. Total isospin T and total angular momentum $J = |\vec{L} + \vec{S}|$ are conserved by strong interactions, which may be thought of as the zeroth selection rule. It is crucial that L and S combine vectorially, so a given J can arise from any L and S satisfying $|L - S| \leq J \leq |L + S|$.

Nucleons, as fermions, obey Pauli statistics, so the wave function of an NN system (including as a component of an $NN\pi$ system) must be antisymmetric under particle exchange. Orbital angular momentum contributes $(-1)^L$ to this antisymmetry, while spin and isospin contribute $(-1)^{S+1}$ and $(-1)^{T+1}$, respectively. As a result, we have the first selection rule $(-1) = (-1)^{L+S+T}$ on both initial and final NN states, satisfied, for example, by ${}^1S_0$ nn and pp states ($S = 0, L = 0, T = 1$). Here we make use of the NN-spectroscopic notation ${}^{2S+1}X(L)_J$, where $X(L)$ is the conventional mapping $0 \to S, 1 \to P, 2 \to S, 3 \to F$ (lowercase will be used for pions).

Parity, the eigenvalue of a physical system under reversal of all spatial coordinates, is another quantum number that is at least approximately conserved under strong interactions [68]. Spin/isospin do not influence parity as they do not contribute to the spatial wave function, but each angular momentum quantum contributes (-1) to parity, which

together with the intrinsic parities of field quanta implies the second selection rule [66],

$$(-1)^{L_i} = \pi_\pi \cdot (-1)^{L_f + l_\pi} \Rightarrow (-1)^{\Delta S + \Delta T} = \pi_\pi (-1)^{l_\pi}, \quad (4.1)$$

where $\pi_\pi = -1$ is the intrinsic parity of the pion (relative to the proton, by convention), and the implication holds only in the presence of Pauli statistics.

As an example application of these rules, consider the $NN \to NN\pi$ processes of an initial ${}^1S_0$ state. Since $J_i = 0 = J_f$, conservation implies $J_f = l_\pi = 0, 1, 2, \ldots$, with each choice allowing for a multiplet of (L_f, S_f) selections. NN isospin $T = 0$, 1, and Pauli statistics require that $T_i = 1$ (nn or pp) as well as that $T_f = S_f + L_f + 1 (\mathrm{mod}\ 2)$.

If $T_f = 1$ ($\Delta T = 0$), Pauli statistics require $S_f + L_f$ to be even. Meanwhile, parity conservation requires $S_f + l_\pi$ to be odd. For example, we could take $S_f = 1$ and $l_\pi = 0$. Then $J_f = 0$, so $L_f = 1$ and the process is ${}^1S_0 \to {}^3P_0 + s$. We might also try $S_f = 0$ and $l_\pi = 1$, so $J_f = 1$ and again $L_f = 1$; but now $S_f + L_f$ is odd, so this combination is deselected. The next lowest-order candidates are $S_f = 2$ and $l_\pi = 1$, which gives $J_f = 1$ and $L_f = 2$ (${}^1S_0 \to {}^5D_1 + p$); and $S_f = 1$ and $l_\pi = 2$, which gives $J_f = 2$ and $L_f = 1$, 3 (${}^1S_0 \to {}^3P_2 + d$, ${}^1S_0 \to {}^3F_2 + d$).

If $T_f = 0$ ($\Delta T = -1$), Pauli statistics require $S_f + L_f$ to be odd, and parity conservation requires $S_f + l_\pi$ to be even. For example, we might try $S_f = 0$ and $l_\pi = 0$, so $J_f = 0$ and $L_f = 0$, but now $S_f + L_f$ is even, so this combination is deselected. Next we could take $S_f = 1$ and $l_\pi = 1$, so $J_f = 1$ and $L_F = 1$, selecting the process ${}^1S_0 \to {}^3S_1 + p$. The next lowest-order candidates are $S_f = 3$ and $l_\pi = 1$, which gives $J_f = 1$ and $L_f = 2$, 4 (${}^1S_0 \to {}^7D_1 + p$,${}^1S_0 \to {}^7G_1 + p$); and $S_f = 1$ and $l_\pi = 3$, which gives $J_f = 3$ and $L_f = 2$, 4 (${}^1S_0 \to {}^3D_3 + f$, ${}^1S_0 \to {}^3G_3 + f$).

The above results are summarized in Table II. Overall, Pauli statistics and the conservation of angular momentum and parity impose quite strong restrictions on what $NN \to NN\pi$ channels can contribute (virtually) to our process. Presuming suppression of higher angular momentum pion states, we will restrict ourselves to ($\Delta T = 0$) ${}^1S_0 \to {}^3P_0 + s$ and ($\Delta T = -1$) ${}^1S_0 \to {}^3S_1 + p$. Significantly, the neutrino-exchange insertion cannot occur in any ${}^1S_0 + x\ NN\pi$ state for ${}^1S_0$ external NN states. Note that only $\Delta T = 0$ can contribute to neutral-pion production, while both isospin channels contribute to charged-pion production.

TABLE II. $NN \to NN\pi$ processes permitted by Pauli statistics, conservation of angular momentum, and conservation of parity for an initial ${}^1S_0$ state, derived in the text and truncated at $J_F = l_\pi \leq 3$.

$NN \to NN\pi$ process	ΔT	$J_f = l_\pi$	S_f	L_f
${}^1S_0 \to {}^3P_0 + s$	0	0	1	1
${}^1S_0 \to {}^5D_1 + p$	0	1	2	2
${}^1S_0 \to {}^3P_2 + d$	0	2	1	1
${}^1S_0 \to {}^3F_2 + d$	0	2	1	3
${}^1S_0 \to {}^3S_1 + p$	−1	1	1	1
${}^1S_0 \to {}^7D_1 + p$	−1	1	3	2
${}^1S_0 \to {}^7G_1 + p$	−1	1	3	4
${}^1S_0 \to {}^3D_3 + f$	−1	3	1	2
${}^1S_0 \to {}^3G_3 + f$	−1	3	1	4

B. Off-shell pion production from nucleon pairs

There exists a long and thorough literature on "threshold" pion production from nucleon pairs in connection to low-energy scattering experiments. This literature will provide us with the necessary tools to account for virtual $NN \to NN\pi$ processes in our $\hat{T}^{(S)}$. As we are only interested in the divergent part of our $0\nu\beta\beta$-decay amplitude and will ultimately compute this through $\overline{\mathrm{MS}}$ at the diagram level, it will not be necessary to explicitly compute $\hat{T}^{(S)}$ as a matrix operator. Instead, here we will identify the leading partial diagrams for both s- and p-wave pion production through dimensional analysis and bound the subleading uncertainties through a comparison to the threshold scenario.

Early works such as [69,70] generally made use of the distorted-wave Born approximation (DWBA), where the process is decomposed into initial- and final-state strong interactions around a fixed, perturbative pion-production core. The three-parameter model described in [69], based on the [71] effective-range approach to p-wave pion-nucleon resonances, was the first to achieve broad agreement with scattering data, ranging from near threshold (where s-wave pion production becomes relevant) to ∼600 MeV (beyond which d-wave pion production becomes relevant). Reference [70] attempts to model higher-energy production using a one-pion-exchange model without final-state interactions, appropriate since deuteron formation is suppressed above ∼800 MeV. This approach is quite prescient of the later role one-pion exchange will play in χEFT-based NN and $NN\pi$ theory. In conceptual agreement with the methods of [8], we will also pursue a DWBA-like separation, but a review of early works that instead made use of fully nonperturbative, coupled-channel computations can be found in [66].

References [72,73] developed a formalism for s-wave pion production near threshold, based on a phenomenological pion-nucleon interaction Hamiltonian that is reminiscent of later χEFT Lagrangians and is accurate within 10% for the process $pp \to d + \pi^+$ while agreeing with limited experimental data on $pp \to pp + \pi^0$. Crucially, p- and s-wave pion production arise from distinct interaction terms, of respective size $\frac{f_\pi}{m_\pi}$ and $\frac{1}{2M_N}$, as well as two

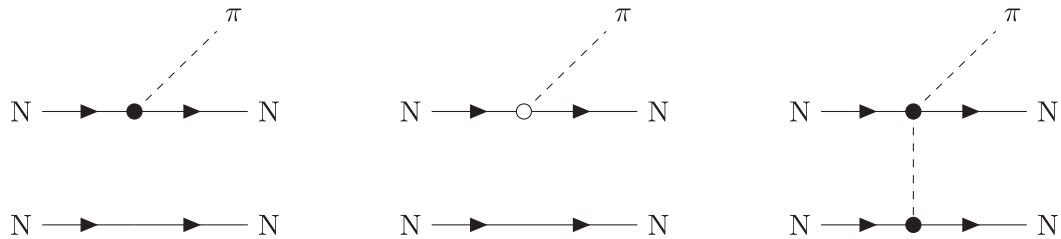

FIG. 6. $NN \to NN\pi$ production via the p-wave $NN\pi$ vertex (left), the suppressed s-wave $NN\pi$ vertex (middle), and the $NN\pi\pi$ Weinberg-Tomozawa vertex (right).

rescattering coefficients fit from πN scattering lengths. Reference [74], focusing on pion absorption, extends this methodology to include virtual ρ- and ω-meson diagrams in an attempt to explain discrepancies with experimental pion absorption in heavier nuclei, ultimately concluding that the fault lies with irreducible three-nucleon contributions. Such additional meson diagrams did, however, account for discrepancies with threshold $pp \to pp\pi^0$ as better data became available [75], albeit in conflict with similarly sized corrections from off-shell πN-rescattering contributions [76].

The first χEFT- and therefore QCD-based computations of $pp \to pp\pi^0$ near threshold were presented in [77,78]. As we have seen for NN scattering, the systematic organization of diagrams via a power counting facilitates a concrete calculation with controlled errors, with typical expansion parameter $\varepsilon \sim m_\pi/M_N \sim 0.1$. This typical power counting arises from treating both the typical three-momentum exchange and the typical nucleon three-momentum of a process as being of the order of the pion mass: $Q \sim p_N \sim m_\pi$. Reference [77] observes that, at threshold, this approximation is not kinematically sound, since at minimum $p_N \sim \sqrt{M_N m_\pi}$ is required to produce a real pion excitation. Then one expects also $Q \sim \sqrt{M_N m_\pi}$, and the revised expansion parameter is $\varepsilon_{\rm thr} \sim \sqrt{m_\pi/M_N} \sim 0.4$; a significantly slower perturbative expansion results, and we will see that in many cases the ordering of diagrams is changed substantially. This detail is relevant to us not because we will use $\varepsilon_{\rm thr}$; in fact, for off-shell pions, $Q \sim p_N \sim m_\pi$ is still a valid expectation, so we will use the standard ε power counting. However, most of the subsequent threshold literature has been expressed in $\varepsilon_{\rm thr}$, and it will be necessary to carefully convert between the two.

At this point, it is useful to define the dominant irreducible diagrams which in some order will fill out the LO through NNLO classes of contributions. The impulse or Born diagram is evidently the simplest, with a single πNN vertex facilitating the process. At threshold, this diagram is kinematically forbidden, as one of the external NN pairs must be off shell by m_π; Ref. [77] resolves this by defining connected impulse diagrams with a single (contact or pion-range) strong interaction, which together may be thought of as the impulse contribution. Equivalently, the connected impulse diagrams are irreducible because no kinematical two-nucleon unitary cut is permitted [66]. Of course, in our application, both the produced pion and the final NN state are expected to be off shell, so we can treat these subsidiary strong interactions as part of the scattered NN wave functions.

Several irreducible diagrams may be seen as modifications of the impulse diagram. The Δ-excitation impulse diagrams provide for an excited nucleon state between the pion-production vertex and the subsidiary strong interaction. The recoil diagrams have distinct kinematics to their one-pion-exchange impulse counterparts. Furthermore, as mentioned previously, there exist two distinct $NN\pi$ vertices corresponding to p- and s-wave pion production, the latter of which is suppressed; impulse diagrams with both vertices are shown in Fig. 6. The seagull or pion-rescattering diagram arises from the inclusion of the $NN\pi\pi$ or Weinberg-Tomozawa (WT) interaction vertex and is irreducible, as seen in Fig. 6. Irreducible diagrams containing higher-dimensional vertices, of course, can be constructed, but are surfeit to our needs. A collection of one-loop irreducible diagrams generically prove to be more relevant [66,77].

The power counting of [77] for s-wave pion production places impulse and Δ-excitation contributions at leading order, with recoil corrections, the seagull diagram, and all one-loop diagrams subleading by a ratio m_π/M_N. However, numerical calculations with phenomenological NN wave functions reveal that the seagull contribution is approximately equal (and opposite in sign) to the impulse contribution, which the authors attribute to some combination of spin/isospin factors and off-shell behavior. They also reveal a suppression of the Δ-excitation contributions that is strongly dependent on the choice of NN potential. Overall, the calculated result is much too small to agree with experiment, and so [77] is taken as a methodological point of comparison rather than a generalizable result. Reference [78] similarly realizes the cancellation between impulse contributions, attributing the mismatch with experiment to unaccounted-for heavy-meson exchange diagrams.

The fully relativistic approach of [79] delivered near percent-precision cross sections for s-wave $pp \to pp\pi^0$ and $pp \to pn\pi^+$ at threshold, including a verification of

the importance of heavy-meson exchange diagrams. The decomposition of an amplitude into perturbative diagrams is (always) model dependent, in the sense that we cannot take this relativistic computation as a comparable breakdown for the power counting of diagrams in χEFT with nonrelativistic nucleons. However, [79] also presents an excellent spin-operator decomposition of both processes,

$$T^{\rm com}_{\rm thr}(pp \to pp\pi^0) = \mathcal{A}(i\vec{\sigma}_1 - i\vec{\sigma}_2 + \vec{\sigma}_1 \times \vec{\sigma}_2)\cdot\vec{p},$$
$$T^{\rm com}_{\rm thr}(pp \to pn\pi^+) = \frac{\mathcal{A}}{\sqrt{2}}(i\vec{\sigma}_1 - i\vec{\sigma}_2 + \vec{\sigma}_1 \times \vec{\sigma}_2)\cdot\vec{p} - \sqrt{2}\mathcal{B}i(\vec{\sigma}_1 + \vec{\sigma}_2)\cdot\vec{p}, \tag{4.2}$$

where two complex-valued coefficients $\mathcal{A}$, $\mathcal{B}$ are then evaluated within one's chosen model and correspond, respectively, to ${}^3P_0 \to {}^1S_0 + s$ and ${}^3P_1 \to {}^3S_1 + s$ transitions [80]. References [66,80] employ the same representation in a demonstration that, with the modified power counting introduced by [77], the perturbative expansion of χEFT for threshold pion production does indeed converge.

It is easier to show this for p-wave pion production because irreducible loop diagrams should only appear at N^{3}LO [81]; the impulse term alone gives agreement within experimental error bars for $p_\pi < 0.7m_\pi$, with seagull and subleading $NN\pi$ vertex contributions entering at NNLO and pushing agreement up to $p_\pi \sim 0.9m_\pi$. For s-wave pion production, irreducible loop diagrams enter at NLO, but Ref. [80] shows an exact cancellation between divergences of these diagrams, which in the neutral-pion case has zero finite part. This is to be expected from consistency of the power counting, Ref. [66] explains, because there is no NNLO counterterm diagram to absorb NLO divergences. To NLO, $\mathcal{A}$ is then built only from the impulse and Δ-excitation terms, while $\mathcal{B}$ is built from the impulse, seagull, and finite-loop terms.

NNLO p-wave pion-production amplitudes were produced by [82] for three experimentally comparable channels ($pn \to pp\pi^-$, $pp \to d\pi^+$, and $pp \to pn\pi^+$), with a comfortable fit to data with $p_\pi < 0.4m_\pi$. Later, [83,84] followed a similar formalism in computing the first complete NNLO s-wave pion-production amplitude, employing a χEFT Lagrangian with explicit Δ degrees of freedom. Order-of-magnitude expectations from the modified power counting of [77] were again verified. Later still, [85] performed the phenomenological NN wave function convolution necessary to compare the NNLO s-wave $pp \to d\pi^+$ amplitude to experimental data, finding a 10%–20% deficit for cutoffs between 600 and 1000 MeV which is attributed to short-range processes, e.g., ρ- and ω-meson exchanges.

All this has been a rather roundabout way of justifying the application of LO and NLO χEFT to the virtual pion production and absorption within our $T^{(S)}$ operators. In the absence of an on-shell requirement for our intermediate $NN\pi$ state, we will follow the Weinberg power counting with small parameter $\varepsilon \sim m_\pi/M_N \sim 0.1$.

For p-wave charged-pion production, the leading terms [66] are the impulse and seagull diagrams of size $p_\pi/m_\pi \sim 1$ and $p_\pi m_\pi/p_N^2 \sim 1$, with error estimate $p_\pi/M_N \sim 0.1$ provided by the same topologies with subleading pion vertices.

For s-wave neutral- and charged-pion production, we need only consider partial amplitude $\mathcal{A}$ since we require one ${}^1S_0$ external NN state. The seagull term vanishes regardless of kinematics as the WT vertex is isovector, so the leading contributions are, in fact, NLO, arising from the subleading impulse and Δ-excitation diagrams of size $p_N/M_N \sim 0.1$.

C. $\pi\pi$ and πN neutrino potentials from χEFT

Now that we have determined the $T^{(S)}$ physics relevant to the $NN\pi$ intermediate-state contribution, we must also compute the relevant neutrino potential contributions corresponding to $\langle NN\pi|T^{(\nu)}|NN\rangle$. Intuitively, one expects that $\langle NN\pi|T^{(\nu)}|NN\pi\rangle$ will be dominated by three channels: the usual neutrino insertion between two nucleon lines (but in the presence of a pion state), an insertion between a pion line and a nucleon line, and a double insertion on the same pion line. The leading irreducible contribution to $\langle NN\pi|T^{(\nu)}|NN\rangle$ also includes a neutrino insertion between one nucleon line and a $\pi\nu NN$ vertex; all these diagrams are displayed in Fig. 7. We already discussed the Lorentz decomposition of neutrino couplings to a single nucleon line in Sec. IV B, in particular, Eq. (3.3) and the following χEFT-derived form factors, but in order to quantify these channels we must first perform a similar analysis of $\Delta L = 2$ couplings to one, two, and three pions and to a $\pi\nu NN$ vertex.

All pion couplings are derivable from the generic chiral Lagrangian, which with external vectorlike couplings can be parametrized as follows [46]:

$$\mathcal{L}_\pi = \frac{F_\pi^2}{4}\mathrm{Tr}\left[(D_\mu U)^\dagger D^\mu U\right] = \frac{F_\pi^2}{4}\mathrm{Tr}\left[\left(\partial_\mu U^\dagger + iU^\dagger l_\mu - ir_\mu U\right)(\partial^\mu U - il^\mu U + iUr^\mu)\right], \tag{4.3}$$

where l_μ and r_μ will facilitate a coupling to the leptonic states via a W propagator and therefore have an associated isospin operator τ^+. Here we show the extraction of the $\pi\nu$ vertex Feynman rule as an example. To compute the coupling to an axial-vector leptonic current $2a_\mu \equiv l_\mu - r_\mu$, we set $-l_\mu = r_\mu = a_\mu$ and find

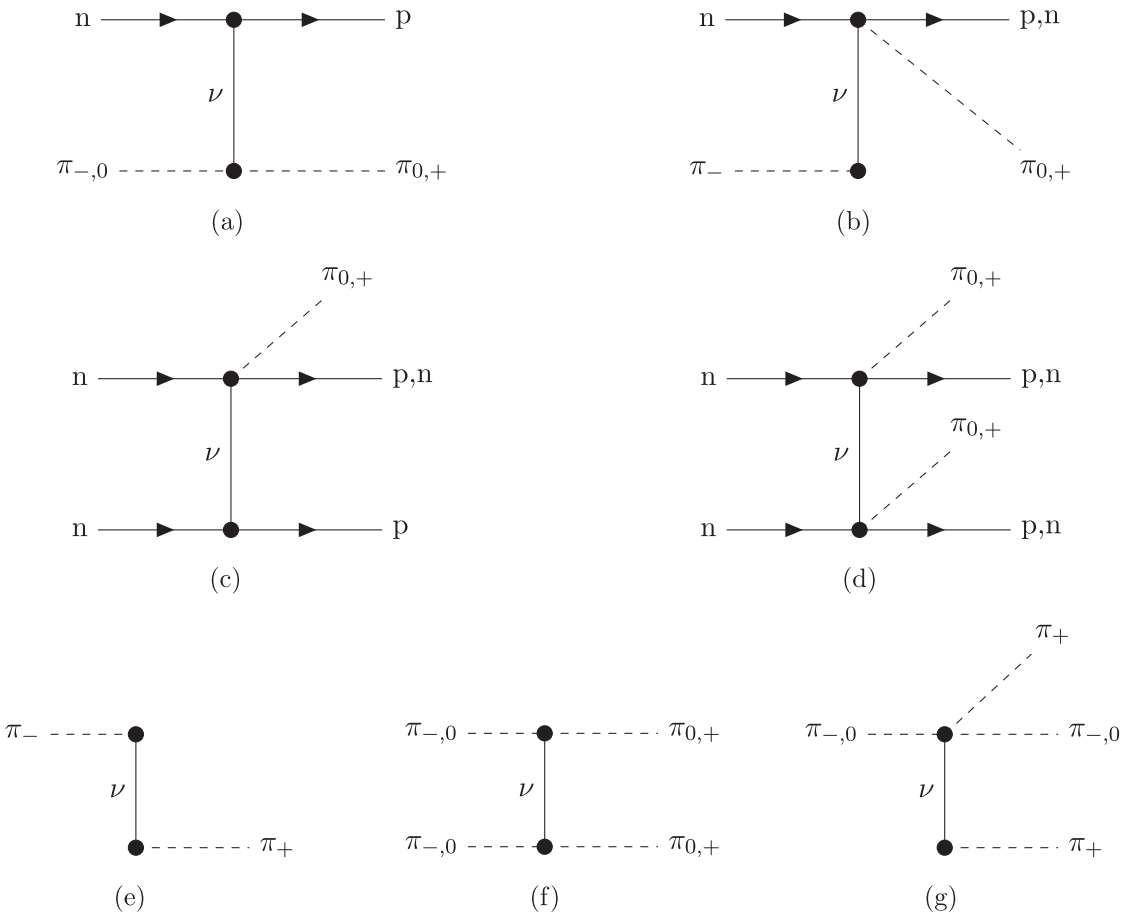

FIG. 7. Diagrams for the neutrino interaction potentials relevant for $NN\pi$ intermediate states. The solid dots denote interaction vertices from the chiral Lagrangian. (a) $NN-\pi\pi$. (b) $NN\pi-\pi$. (c) $NN\pi-NN$. (d) $NN\pi-NN\pi$. (e) $\pi-\pi$. (f) $\pi\pi-\pi\pi$. (g) $\pi\pi\pi-\pi$.

$$\begin{aligned}\mathcal{L}_\pi &= \frac{iF_\pi^2}{4}\mathrm{Tr}\left[\frac{-i}{F_\pi}\partial_\mu\vec{\phi}\cdot\vec{\tau}(2a^\mu\tau^+) + (-2a_\mu\tau^+)\frac{i}{F_\pi}\partial^\mu\vec{\phi}\cdot\vec{\tau}\right]\\ &= \frac{F_\pi}{2}Tr\left[\left\{\partial_\mu\vec{\phi}\cdot\vec{\tau},\tau^+\right\}\right]a^\mu\\ &= F_\pi\sqrt{2}\partial_\mu[\pi^-]a^\mu, \end{aligned} \tag{4.4}$$

where the quantity in square brackets indicates the isospin constraints on the Feynman vertex, amounting to charge conservation (i.e., only a π_- may decay to an e_-). Strictly speaking, this pion field is factored away from the coupled current at the vertex, so this notation serves only to indicate which diagrams are permitted. If instead, one takes $l_\mu = r_\mu = v_\mu$, a trivial cancellation reveals that the π coupling to a vector leptonic current vanishes. Similar computations reveal the patterned structure of $N\pi\nu$ vertices, where we display only those relevant for our $NN\pi$ diagrams,

$$\begin{aligned} J^\mu_{V,\pi} &= 0,\\ J^\mu_{A,\pi} &= -iF_\pi\sqrt{2}q^\mu[\pi^-],\\ J^\mu_{V,\pi\pi} &= -\sqrt{2}q^\mu[\pi^-\pi^0],\\ J^\mu_{A,\pi\pi} &= 0,\\ J^\mu_{V,\pi\pi\pi} &= 0,\\ J^\mu_{A,\pi\pi\pi} &= i\frac{1}{F_\pi}\sqrt{2}q^\mu[\pi^-\pi^0\pi^0 + 2\pi^-\pi^+\pi^-]. \end{aligned} \tag{4.5}$$

Also derivable from the above Lagrangian is the Feynman rule for the four-pion vertex, which we will later need to connect the $\pi\pi\pi-\pi$ neutrino potential into a loop diagram. In our case, this vertex will connect two momenta $\pm k$ and two momenta $\pm l$ and has amplitude

$$iA_{\pi\pi\pi\pi} = \frac{-2}{3F_\pi^2}(k^2 + l^2 - 2M^2), \tag{4.6}$$

where M^2 is a mass parameter generated by the explicit chiral symmetry breaking of the quark masses, which at LO is simply m_π^2 [13].

To study the $\pi\nu NN$ vertex, we also follow [46] in introducing an NLO nucleonic chiral Lagrangian,

$$\begin{aligned}\mathcal{L}_{\pi N,\mathrm{LO}} &= i\bar{N}V\cdot DN + g_A\bar{N}S\cdot uN,\\ \mathcal{L}_{\pi N,\mathrm{NLO}} &= \frac{1}{2M_N}(V^\mu V^\nu - \eta^{\mu\nu})(\bar{N}D_\mu D_\nu N)\\ &\quad + \frac{ig_A}{2M_N}\bar{N}\{S\cdot D, V\cdot u\}N,\end{aligned} \tag{4.7}$$

where a static nucleon approximation has been made with velocity $V^\mu = (1,\vec{0})$ and spin $S^\mu = (0,\vec{\sigma})$. D_μ is the chiral-covariant derivative derived in terms of covariant vector Γ_μ, and u_μ is the contravariant vector counterpart,

$$\begin{aligned}\Gamma_\mu &= D_\mu - \partial_\mu = \frac{1}{2}\left[u^\dagger(\partial_\mu - il_\mu)u + u(\partial_\mu - ir_\mu)u^\dagger\right],\\ u_\mu &= i\left[u^\dagger(\partial_\mu - il_\mu)u - u(\partial_\mu - ir_\mu)u^\dagger\right].\end{aligned} \tag{4.8}$$

Note that this is the same chiral order to which the neutrino potential for NN states has been presented here as well as in [8]. We will see that those terms in the Lagrangian that contributed to the vector coupling for an NN state will contribute only to the axial-vector coupling here, and vice versa. Again setting $-l_\mu = r_\mu = a_\mu$ for the axial-vector contribution, we find at LO

$$\begin{aligned}i\bar{N}V^\mu\vec{D}_\mu N &= i\bar{N}V^\mu\Gamma_\mu N\\ &= \frac{i}{2}\bar{N}V^\mu\left(u^\dagger(iA_\mu\tau^+)u + u(-iA^\mu\tau^+)u^\dagger\right)\\ &= \frac{-1}{2}\bar{N}V^\mu\frac{i}{F_\pi}A_\mu\left[\tau^+,\vec{\phi}\cdot\vec{\tau}\right]N\\ &= \frac{-i}{2F_\pi}V^\mu A_\mu[\sqrt{2}\bar{p}\pi^- p - \sqrt{2}\bar{n}\pi^- n - 2\bar{p}\pi^0 n],\end{aligned} \tag{4.9}$$

and at NLO

$$\begin{aligned}i\bar{N}\overleftarrow{D}_\mu\vec{D}_\nu N &= \overline{N}(\overleftarrow{\partial}_\mu\Gamma_\nu + \Gamma_\mu\vec{\partial}_\nu)N\\ &= \frac{-i}{2F_\pi}\frac{p^\mu + p'^\mu}{2M_N}A_\mu\\ &\quad\times\left[\sqrt{2}\bar{p}\pi^- p - \sqrt{2}\bar{n}\pi^- n - 2\bar{p}\pi^0 n\right].\end{aligned} \tag{4.10}$$

Setting $l_\mu = r_\mu = v_\mu$ for the vector contribution, we find at LO

$$\begin{aligned}g_A\bar{N}S\cdot uN &= g_A\bar{N}S^\mu\left(u^\dagger v_\mu\tau^+u - uv_\mu\tau^+u^\dagger\right)\\ &= \frac{ig_A}{F_\pi}\bar{N}S^\mu,\left[\tau^+,\vec{\phi}\cdot\vec{\tau}\right]v_\mu N\\ &= \frac{ig_A}{F_\pi}S^\mu v_\mu,[\sqrt{2}\bar{p}\pi^- p - \sqrt{2}\bar{n}\pi^- n - 2\bar{p}\pi^0 n],\end{aligned} \tag{4.11}$$

and at NLO

$$\begin{aligned}-\frac{ig_A}{2M_N}\{S\cdot D, V\cdot u\}N &= \frac{g_A}{2F_\pi M_N}\bar{N}\left\{S^\mu\partial_\mu, V^\nu v_\nu[\tau^+,\vec{\phi}\cdot\vec{\tau}]\right\}N\\ &= \frac{-ig_A}{F_\pi}\frac{V^\mu}{2M_N}S\cdot(p+p')v_\mu,\left[\sqrt{2}\bar{p}\pi^- p - \sqrt{2}\bar{n}\pi^- n - 2\bar{p}\pi^0 n\right],\end{aligned} \tag{4.12}$$

as well as the vector current induced by the pseudoscalar $NN\pi$ vertex and the $\pi-\nu$ coupling derived above,

$$J^\mu_{V,\mathrm{induced}} = \frac{ig_A}{F_\pi}\left(\frac{1}{q^2+m_\pi^2}q^\mu S\cdot q\right),[\sqrt{2}\bar{p}\pi^- p - \sqrt{2}\bar{n}\pi^- n - 2\bar{p}\pi^0 n]. \tag{4.13}$$

Thus, in total, we have for the currents at the $\pi\nu NN$ vertex,

$$\begin{aligned}J^\mu_{V,NN\pi} &= \frac{ig_A}{F_\pi}\left(S^\mu - \frac{V^\mu}{2M_N}S\cdot(p+p') + \frac{1}{q^2+m_\pi^2}q^\mu S\cdot q\right),\\ &\quad\cdot\left[\sqrt{2}\bar{p}\pi^- p - \sqrt{2}\bar{n}\pi^- n - 2\bar{p}\pi^0 n\right],\\ J^\mu_{A,NN\pi} &= \frac{-i}{2F_\pi}\left(v^\mu + \frac{p^\mu + p'^\mu}{2M_N}\right),\qquad\left[\sqrt{2}\bar{p}\pi^- p - \sqrt{2}\bar{n}\pi^- n - 2\bar{p}\pi^0 n\right].\end{aligned} \tag{4.14}$$

With all vertex-level building blocks defined, we can now contract them to form complete $\Delta L = 2$ potentials for $NN\pi$ states. Let us first consider the neutrino interaction between a nucleon line and a pion line, shown diagrammatically in Fig. 7(a). Since we have seen that the latter only couples via a vector current, the $NN - \pi\pi$ potential is given by

$$\begin{aligned} J^{\mu}_{V,NN} \cdot J_{\mu V,\pi\pi} &= \left(V^{\mu} + \frac{p^{\mu} + p'^{\mu}}{2M_N}\right)(-\sqrt{2}q^{\mu}) \\ &= -\sqrt{2}\left(q_0 + \frac{q\cdot(p+p')}{2M_N}\right) \\ &= -\sqrt{2}q_0[n\pi_0 \to p\pi_+, n\pi_- \to p\pi_0], \end{aligned} \tag{4.15}$$

where the final simplification results from observing that $q\cdot(p+p') = (p-p')\cdot(p+p') = p^2 - p'^2 \simeq E_{1,2}^2$. Following [46], we count the electron energies at NNLO in the chiral power counting, specifically $E_{1,2} \sim m_\pi(\frac{Q}{\Lambda_\chi})^2$, and therefore such terms can be safely neglected from our NLO potentials.

The neutrino interaction between a $\pi\nu NN$ vertex and a single π, shown in Fig. 7(b), proceeds only via an axial-vector current, but delivers a very similar potential to the above [this is less surprising comparing the diagram to that of Fig. 7(a)],

$$\begin{aligned} J^{\mu}_{A,NN\pi} \cdot J_{\mu A,\pi} = -\frac{\sqrt{2}}{2}q_0, \Big[&\sqrt{2}p\pi_- \to p\pi_+, \\ &-\sqrt{2}n\pi_- \to n\pi_+, -2n\pi_- \to p\pi_0\Big]. \end{aligned} \tag{4.16}$$

In fact, this pair of potentials very clearly exhibits the importance of carrying through all isospin algebra; although their kinematic dependence differs only by a constant factor, they share only one isospin channel and discriminate between three others. The neutrino interaction between a $\pi\nu NN$ vertex and a nucleon line NN, shown in Fig. 7(c), exhibits more complexity, as both vector $V - V$ and axial-vector $A - A$ channels may contribute. Fortunately, these two components turn out to be identical, and the static nucleon approximation leads to significant simplification,

$$\begin{aligned} J^{\mu}_{V,NN\pi} \cdot J_{\mu V,NN} &= J^{\mu}_{A,NN\pi} \cdot J_{\mu A,NN} \\ &= \frac{ig_A}{F_\pi}\left(S^{\mu} - \frac{v^{\mu}}{2M_N}S\cdot(p+p') + \frac{1}{q^2+m_\pi^2}q^{\mu}S\cdot q\right)\left(v_{\mu} + \frac{p_{\mu}+p'_{\mu}}{2M_N}\right) \\ &= \frac{ig_A}{F_\pi}\left(\frac{1}{q^2+m_\pi^2}q_0 S\cdot q - \frac{1}{4M_N^2}(p^0+p'^0)S\cdot(p+p') + \frac{1}{q^2+m_\pi^2}\frac{1}{2M_N}q\cdot(p+p')S\cdot q\right) \\ &= \frac{ig_A}{F_\pi}\left(\frac{1}{q^2+m_\pi^2}q_0\frac{1}{2}\vec{\sigma}\cdot\vec{q} - \frac{\vec{\sigma}\cdot(\vec{p}+\vec{p'})}{4M_N}\right)\left[\sqrt{2}np \to pp\pi_+, -\sqrt{2}nn \to pn\pi_+, -2nn \to pp\pi_0\right]. \end{aligned} \tag{4.17}$$

Similarly, the neutrino interaction between two $\pi\nu NN$ vertices, shown in Fig. 7(d), receives contributions from both vector $V - V$ and axial-vector $A - A$ channels. The current algebra matches that of the NN neutrino exchange, albeit with vector and axial-vector contributions interchanged, and an additional constant factor $\frac{-1}{F_\pi^2}$,

$$\begin{aligned} J^{\mu}_{V,NN\pi} \cdot J_{\mu V,NN\pi} &= \frac{-4g_A^2}{F_\pi^2}\left(S^{\mu} - \frac{v^{\mu}}{2M_N}S\cdot(p+p') + \frac{1}{q^2+m_\pi^2}q^{\mu}S\cdot q\right)^2 \\ &= \frac{-4g_A^2}{F_\pi^2}\left(S\cdot S + \frac{2}{q^2+m_\pi^2}(S\cdot q)^2 + \frac{q^2}{(q^2+m_\pi^2)^2}(S\cdot q)^2\right) \\ &= \frac{g_A^2}{F_\pi^2}\left(\vec{\sigma}_1\cdot\vec{\sigma}_2 - \frac{q^2+2m_\pi^2}{(q^2+m_\pi^2)^2}\vec{\sigma}_1\cdot\vec{q}\vec{\sigma}_2\cdot\vec{q}\right) \\ &= \frac{g_A^2}{F_\pi^2}\left(\frac{2}{3}\vec{\sigma}_1\cdot\vec{\sigma}_2\left(1 + \frac{m_\pi^4}{2(q^2+m_\pi^2)^2}\right) + \frac{1}{3}S_{12}\left(1 - \frac{m_\pi^4}{(q^2+m_\pi^2)^2}\right)\right), \\ &\quad [nn \to pp\pi_0\pi_0], \end{aligned} \tag{4.18}$$

and

$$J^{\mu}_{A,NN\pi} \cdot J_{\mu A,NN\pi} = \frac{-1}{F_\pi^2}\left(V_{\mu} + \frac{p_{\mu}+p'_{\mu}}{2M_N}\right)^2 = \frac{-1}{F_\pi^2} + \mathcal{O}\left(\frac{Q^2}{\Lambda_\chi^2}\right), \qquad [nn \to pp\pi_0\pi_0]. \tag{4.19}$$

TABLE III. Neutrino interaction potentials $V^{\nu}_{(X,Y)} = J^{\mu}_{V,X} \cdot J_{\mu_V,Y} + J^{\mu}_{A,X} \cdot J_{\mu_A,Y}$ as functions of exchange momentum q. These potentials correspond to the diagrams of Fig. 7.

Potential $V^{\nu}_{\ldots}$	$G_F^2 V_{ud}^2 m_{\beta\beta}\ (\ldots)\ \overline{u}(k_1)\hat{P}_R C\overline{u}^T(k_2)$
$(NN, \pi\pi)$	$-\sqrt{2}\frac{q_0}{q^2}$
$(NN\pi, \pi)$	$-\frac{\sqrt{2}}{2}\frac{q_0}{q^2}$
$(NN\pi, NN)$	$\frac{ig_A}{F_\pi}\frac{1}{q^2}\left(\frac{1}{q^2+m_\pi^2}q_0\frac{1}{2}\vec{\sigma}\cdot\vec{q} - \frac{\vec{\sigma}\cdot(\vec{p}+\vec{p}')}{4M_N}\right)$
$(NN\pi, NN\pi)$	$\frac{-1}{F_\pi^2}\frac{1}{q^2}(1 - \vec{\sigma}_1\cdot\vec{\sigma}_2 - \frac{q^2+2m_\pi^2}{(q^2+m_\pi^2)^2}\vec{\sigma}_1\cdot\vec{q}\vec{\sigma}_2\cdot\vec{q})$
(π, π)	$-2F_\pi^2$
$(\pi\pi, \pi\pi)$	2
$(\pi\pi\pi, \pi)$	2

Here we have only included the isospin factors for the double-neutral-pion case, as this is the only one relevant for our later analysis. The charged-pion channels are slightly suppressed by factors of either $\pm\sqrt{2}$ or ± 2.

Finally, we have three pion-only potentials, of the forms $\pi - \pi$, $\pi\pi - \pi\pi$, and $\pi\pi\pi - \pi$, which are shown in Figs. 7(e)–7(g), respectively. The first and third of these involve only axial-vector couplings because both vertices connect an odd number of pions; the second conversely involves only vector couplings. Contracting our previously calculated currents, we have

$$J^{\mu}_{A,\pi} \cdot J_{\mu A,\pi} = (-iF_\pi\sqrt{2}q^\mu)(-iF_\pi\sqrt{2}q_\mu) = -2F_\pi^2 q^2, [\pi_- \to \pi_+], \tag{4.20}$$

$$J^{\mu}_{V,\pi\pi} \cdot J_{\mu V,\pi\pi} = (-\sqrt{2}q^\mu)(-\sqrt{2}q_\mu) = 2q^2, [\pi_-\pi_- \to \pi_0\pi_0, \pi_-\pi_0 \to \pi_0\pi_+, \pi_0\pi_0 \to \pi_+\pi_+], \tag{4.21}$$

$$J^{\mu}_{A,\pi\pi\pi} \cdot J_{\mu A,\pi} = \left(\frac{-i}{F_\pi}\sqrt{2}q^\mu\right)(-iF_\pi\sqrt{2}q_\mu) = 2q^2, \qquad [\pi_0 \to \pi_0\pi_+\pi_+, 2\pi_- \to \pi_-\pi_+\pi_+]. \tag{4.22}$$

To express these products of currents as bona fide two-nucleon potentials, we must include the neutrino propagator $\frac{1}{q^2}$ as well as the leptonic structure (and dimensionful constants) that apply equally to all topologies. The resultant potentials are collected in Table III.

In computing these NLO potentials, we experience the full benefits of the χEFT formulation of nuclear forces. The highly symmetric interactions permitted for pions deliver simple kinematics for all permitted ν interactions. Indeed, only the $J^{\mu}_{V,NN\pi} \cdot J_{\mu V,NN}$ potential has any spin or pion-mass

Diagram	Dimensional Analysis	Chiral Order
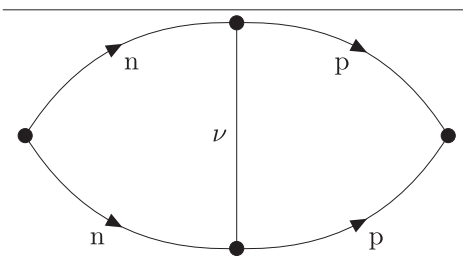	$g_V \cdot g_V + g_A \cdot g_A = 1 + g_A^2 \simeq 2.6$	LO
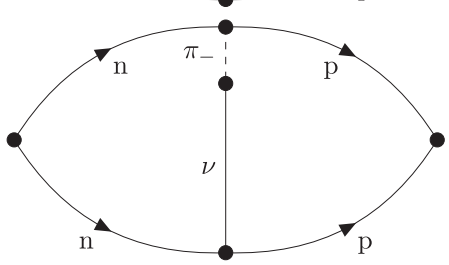	$\frac{g_A}{2}\frac{Q}{F_\pi}\cdot\frac{1}{Q^2}\cdot\sqrt{2}F_\pi Q\cdot g_A = g_a^2\frac{\sqrt{2}}{2} \simeq 1.1$	LO
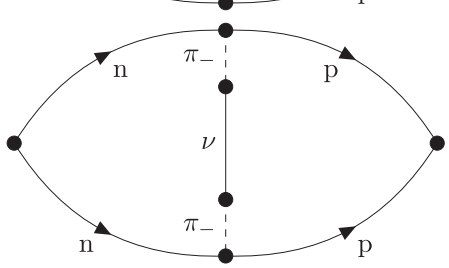	$\left(\frac{g_A}{2}\frac{Q}{F_\pi}\cdot\frac{1}{q^2}\cdot\sqrt{2}F_\pi Q\right)\cdot\left(\frac{g_A}{2}\frac{Q}{F_\pi}\cdot\frac{1}{Q^2}\cdot\sqrt{2}F_\pi Q\right) = \frac{g_a^2}{2} \simeq 0.8$	LO

FIG. 8. Dimensional analysis of leading NN neutrino-exchange diagrams. They are all at LO in the chiral power counting.

dependence up to NLO, a fact that will dramatically ease the estimation of our leading $0\nu\beta\beta$ diagrams.

D. Diagrammatics and power counting of the leading $NN\pi$ divergences

With both off-shell pion production/absorption $NN \to NN\pi$ and $NN\pi \to NN$ and neutrino potentials connecting $NN\pi$ and NN states characterized, we can now present the complete set of diagrams whose divergences will contribute to the size of the contact $0\nu\beta\beta$ counterterm. These are shown in Fig. 9, alongside the workings that demonstrate their (order-of-magnitude) NLO status in the chiral power counting; the diagrams with only NN intermediate states are also presented in Fig. 8.

We largely follow the power counting formalized in [86]. As is standard in chiral perturbation theory, pion propagators (being light compared to the cutoff scale) contribute $1/Q^2$, while nucleon propagators (being heavy compared to the cutoff scale and therefore static) contribute $1/Q$. Loop integrals generically contribute $Q^4/(4\pi)^2$, where the factor $(4\pi)^{-2}$ arises from angular integrations of $\frac{dq^4}{(2\pi)^4}$. From the exponential form of U in the chiral Lagrangian, a vertex with d derivatives, p-pion fields, and n-nucleon fields can be expected to contribute $Q^d F_\pi^{2-p-b} \Lambda_\chi^{2-d-b/2}$. At this point, two large scales enter into the power counting: F_π and Λ_χ; Manohar and Georgi's "naive dimensional analysis" procedure [15] shows that, in order for the leading non-renormalizable four-pion vertex to be sufficiently and naturally suppressed, Λ_χ can be at most $4\pi F_\pi$, and in the chiral power counting we take this bound to be saturated.

For multinucleon interactions, [20] showed that one must treat nucleon propagators and loops differently when they appear as reducible subdiagrams, i.e., elastic intermediate states. When integrating over these internal nucleon lines, pole contributions effectively restrict the nucleon from a static treatment, with the result [32,86,87] that the nucleon propagator is enhanced to $\sim M_N/Q^2$. The loop integral contribution is adjusted to $Q^5/(4\pi M_N)$, but since in the power counting $M_N \sim \Lambda_\chi \sim 4\pi Q$, is of the same order as the irreducible loop integral.

An additional feature of the chiral power counting specific to our application is that it distinguishes between p- and s-wave pion production from/absorption to NN states. As discussed in Sec. IV B and in [66], the leading $NN\pi$ vertex in the chiral Lagrangian only gives nonzero contributions for p-wave pion production and is assigned size $\frac{g_A}{2}\frac{Q}{F_\pi}$ in agreement with the generic vertex expression from [86] (we choose to retain simple constant factors since they prove substantial for certain $NN\pi$ diagrams). The first vertex to contribute to s-wave pion production is suppressed by 1 chiral order, specifically by a ratio $\frac{\omega_\pi}{2M_N}$ where ω_π is the pion energy. We recall that neutral-pion production receives no contribution from the p wave.

We conduct our power counting in the manner appropriate for comparison to the integrand $a_\chi(k)$ in the matching expression [8]

$$2g_\nu^{NN}(\mu) = \frac{1+2g_A^2}{2} - \int_0^\mu dk a_\chi(k) + \int_0^\Lambda dk a_<(k) + \int_\Lambda^\infty dk a_<(k). \tag{4.23}$$

Thus, the factor $\frac{M_N^2}{(4\pi)^2}$ arising from the two NN contact interactions on either side of each bubble diagram is neglected, and we implicitly include the neutrino-momentum measure $d|k|$ such that each estimate is formally dimensionless. As a proof of concept, Fig. 8 shows the application of our chosen power counting to the elastic diagrams $\mathcal{A}_C$ containing divergences; we separate these diagrams to make explicit the contributions from the pseudoscalar-induced axial $NN\nu$ coupling, whose presence will play a more direct role in the $NN\pi$-inelastic diagrams to follow. As expected, all three diagrams enter at leading chiral order $(\frac{Q}{\Lambda_\chi})^0$.

In Fig. 9, a complete classification is presented of NN $0\nu\beta\beta$ diagrams whose neutrino exchange occurs in an $NN\pi$ hadronic intermediate state. From the six neutrino potentials exhibited and two competing pion production/absorption channels (charged and neutral), one might naively have expected as many as 24 distinct topologies. However, isospin symmetry places severe restrictions on these combinatorics, leaving only the eight families of diagrams illustrated in Fig. 9. Note that we show only one representative of each family, whose pion production and absorption occur via the impulse diagram defined in Sec. IV B. As described there, each p-wave charged-pion production/absorption can occur either via an impulse or a seagull (pion-rescattering) diagram, both at leading order. In our power counting estimate, we will neglect the seagull diagrams, as simple power counting shows that the presence of an additional loop integral suppresses such diagrams by 2 chiral orders. Each s-wave neutral-pion production likewise can occur either via an impulse diagram or a Δ-excitation diagram, both at subleading order. We elect not to include these Δ-excitation diagrams in our estimate for the reason of consistency with our truncation of the inelastic hadronic states to $NN\pi$. Including Δ degrees of freedom in one stage of our calculation would necessitate their inclusion throughout, in particular, in the intermediate hadronic state present for neutrino exchange, which lies beyond the scope of this work. Furthermore, each charged-pion production/absorption diagram also includes a subleading s-wave component; we do not explicitly consider these, but they serve as a reminder that, generically, diagrams that enter the chiral power counting at some particular order may also experience contributions at any or all higher orders.

	Diagram	Dimensional Analysis	Chiral Order
(a)	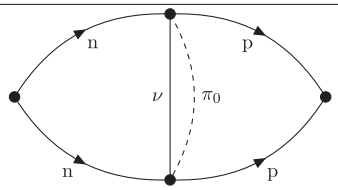	$\frac{1}{F_\pi^2}\left(1+2g_A^2\right)\cdot\frac{1}{Q^2}\cdot\int\frac{dQ^4}{(4\pi)^2}$ $=\left(1+2g_A^2\right)\frac{1}{(4\pi)^2}\simeq\left(1+2g_A^2\right)\left(\frac{Q}{\Lambda_\chi}\right)^2 \simeq 4.2\left(\frac{Q}{\Lambda_\chi}\right)^2$	$NNLO$
(b)	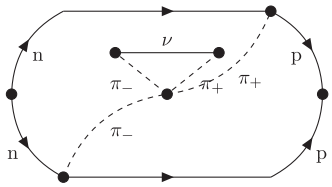	$\left(2Q^2\right)\cdot\left(\frac{1}{Q^2}\right)^3\cdot\int\frac{dQ^4}{(4\pi)^2}=2\frac{1}{(4\pi)^2} \simeq 2\left(\frac{Q}{\Lambda_\chi}\right)^2$	$NNLO$
(c)	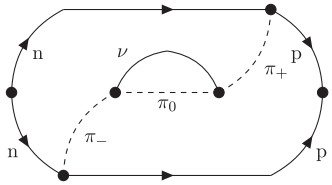	$\left(2F_\pi^2Q^2\right)\cdot\left(\frac{1}{Q^2}\right)^4\cdot\int\frac{dQ^4}{(4\pi)^2}=2\frac{F_\pi}{Q}\frac{1}{(4\pi)^2} \simeq 2\left(\frac{Q}{\Lambda_\chi}\right)^2$	$NNLO$
(d)	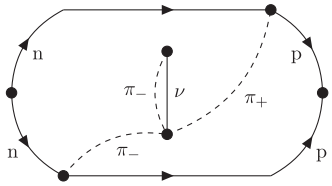	$\left(2Q^2\right)\cdot\left(\frac{1}{Q^2}\right)^3\cdot\int\frac{dQ^4}{(4\pi)^2}=2\frac{1}{(4\pi)^2} \simeq 2\left(\frac{Q}{\Lambda_\chi}\right)^2$	$NNLO$
(e)	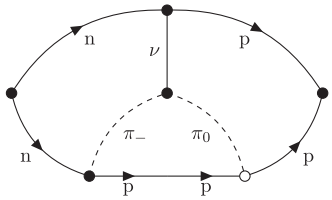	$\left(\sqrt{2}Q\right)\cdot\left(\frac{1}{Q^2}\right)^2\cdot\frac{1}{Q}\cdot\left(\frac{g_a}{2}\frac{Q}{F_\pi}\right)\cdot\left(\frac{g_A}{4}\frac{Q\omega_\pi}{F_\pi M_N}\right)\cdot\int\frac{dQ^4}{(4\pi)^2}$ $=\frac{1}{4\sqrt{2}}\frac{1}{(4\pi)^2}g_A^2\frac{Q^3}{F_\pi^2M_N}\simeq\frac{g_A^2}{4\sqrt{2}}\left(\frac{Q}{\Lambda_\chi}\right)^3 \simeq 0.3\left(\frac{Q}{\Lambda_\chi}\right)^3$	N^3LO
(f)	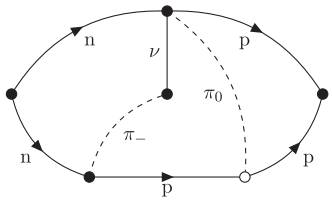	$\left(\frac{\sqrt{2}}{2}Q\right)\cdot\left(\frac{1}{Q^2}\right)^2\cdot\frac{1}{Q}\cdot\left(\frac{g_a}{2}\frac{Q}{F_\pi}\right)\cdot\left(\frac{g_A}{4}\frac{Q\omega_\pi}{F_\pi M_N}\right)\cdot\int\frac{dQ^4}{(4\pi)^2}$ $=\frac{1}{8\sqrt{2}}\frac{1}{(4\pi)^2}g_A^2\frac{Q^3}{F_\pi^2M_N}\simeq\frac{g_A^2}{8\sqrt{2}}\left(\frac{Q}{\Lambda_\chi}\right)^3 \simeq 0.15\left(\frac{Q}{\Lambda_\chi}\right)^3$	N^3LO
(g)	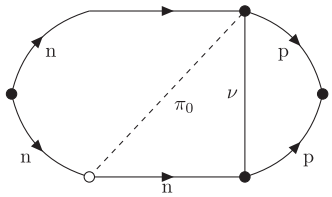	$\left(\frac{g_A}{F_\pi}\right)\cdot\frac{1}{Q^2}\cdot\frac{1}{Q}\cdot\left(\frac{g_A}{4}\frac{Q\omega_\pi}{F_\pi M_N}\right)\cdot\int\frac{dQ^4}{(4\pi)^2}$ $=\frac{g_A^2}{4}\left(\frac{Q}{\Lambda_\chi}\right)^3 \simeq 0.4\left(\frac{Q}{\Lambda_\chi}\right)^3$	N^3LO
(h)	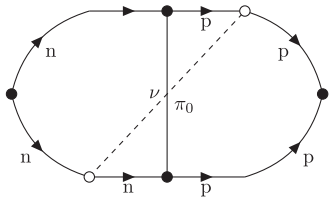	$\left(1+2g_A^2\right)\cdot\left(\frac{g_A}{4}\frac{Q\omega_\pi}{F_\pi M_N}\right)^2\cdot\frac{1}{Q^2}\cdot\left(\frac{1}{Q}\right)^2\cdot\int\frac{dQ^4}{(4\pi)^2}$ $=\left(1+2g_A^2\right)\frac{g_A^2}{16}\frac{1}{(4\pi)^2}\simeq\left(1+2g_A^2\right)\frac{g_A^2}{16}\left(\frac{Q}{\Lambda_\chi}\right)^4\simeq 0.4\left(\frac{Q}{\Lambda_\chi}\right)^4$	N^4LO

FIG. 9. Dimensional analysis of leading $NN\pi$ neutrino-exchange diagrams. Diagram (a) is the "eye" diagram evaluated in Eq. (4.35), diagrams (b)–(d) are the "surfer" diagrams evaluated in Eqs. (4.27)–(4.34), and diagrams (e)–(h) give significantly subleading contributions, as explained in the text.

This classification reveals four broader types of $NN\pi$ diagrams according to the isospin properties of their virtual pion. First, the lone "eye" diagram in Fig. 9(a) simply inserts a pion exchange at the same vertices of the neutrino exchange, as captured by our $NN\pi - NN\pi$ neutrino potential. The pion production vertices contribute near unity factors of $\frac{Q}{F_\pi}$, but the integration of the pion loop suppresses Fig. 9(a) to NNLO in the chiral counting, 2 orders below the NN contributions. The eye diagram topology was fully evaluated in Appendix C of [8] and forms the basis of the $NN\pi$ uncertainty estimate quoted in that work. Second, three "surfer" diagrams [Figs. 9(b)–9(d)] are distinguished by both charged-pion production and absorption, as well as by neutrino exchange via a purely pionic potential; these diagrams are also suppressed to NNLO. However, all the other families of diagrams will experience additional suppressions. Next, three "mountain" diagrams [Figs. 9(e)–9(g)] involve a lone neutral-pion interaction (some with an additional charged-pion interaction), with the neutrino exchanged via a mixed pion-nucleon potential; all these diagrams are suppressed to $\mathrm{N^3LO}$ due to the s-wave interaction of the neutral pion. Note that each of these diagrams has a further multiplicity of 2 since the neutral pion could interact on either nucleon line, not impacting the power counting estimate but giving a distinct momentum routing. Finally, the lone "bridge" diagram [Fig. 9(h)] is present, whose virtual pion experiences 1 order of suppression at both the production and absorption ends, while neutrino exchange occurs via a purely nucleonic potential, just as in the NN contribution of [8]. This diagram is thus suppressed to $\mathrm{N^4LO}$, along with a family of variations depending on the placement of the pion-production vertices on the nucleon lines. Overall, one expects from the power counting that the surfer diagrams will dominate with the mountain diagrams subleading.

Before proceeding to the integrals, we can now give a power-counting-driven estimate of the error bar that $0\nu\beta\beta$ diagrams with an $NN\pi$ intermediate-state place on the elastic contact term size. Summing all diagrams constructively alongside the aforementioned multiplicities for each family, approximating $\frac{Q}{\Lambda\chi} \sim \frac{1}{7.5}$, and comparing with the estimate $g_{NN}(\mu_\chi = m_\pi) \simeq 1.32$ from [8], we find

$$\begin{aligned}\Delta g_{NN\pi} &\sim (4.2 + 2\cdot 2 + 2\cdot 2 + 2\cdot 2)\left(\frac{Q}{\Lambda\chi}\right)^2 \\ &\quad + (8\cdot 0.3 + 8\cdot 0.15 + 8\cdot 0.4)\left(\frac{Q}{\Lambda\chi}\right)^3 \\ &\quad + (4\cdot 0.4)\left(\frac{Q}{\Lambda\chi}\right)^4 \\ &= 0.288_{\mathrm{NNLO}} + 0.016_{\mathrm{N^3LO}} + 0.0005_{\mathrm{N^4LO}}, \\ \frac{\Delta g_{NN\pi}}{g_{NN}} &= 21.8\%_{\mathrm{NNLO}} + 1.2\%_{\mathrm{N^3LO}} + 0.04\%_{\mathrm{N^4LO}}. \end{aligned} \tag{4.24}$$

This estimate is in agreement with the error bars allocated by [8], suggesting that we can expect as much as a 22% modification to the size of contact counterterm g_ν^{NN} through the inclusion of our NNLO corrections (the eye and surfer diagrams). Even further, our estimate shows that, if all four described NNLO diagrams [Figs. 9(a)–9(d)] are taken into account in a complete regularization analysis, the remaining $NN\pi$ contributions only induce uncertainties on the order of 1%.

E. Dimensional regularization of the NNLO $NN\pi$ divergences

In the preceding subsection, we identified a collection of four neutrino-exchange diagrams, the "eye" diagram [Fig. 9(a)] and "surfer" diagrams [Figs. 9(b)–9(d)], as encoding the leading $NN\pi$ contribution to NN $0\nu\beta\beta$ decay. These diagrams and their power counting are shown in the top four rows of Fig. 9 and were expected to enter at NNLO in the chiral power counting, with as much as a 8% modification to the elastic contact coefficient anticipated. Here we will test that hypothesis by evaluating the divergent part of all four diagrams in the dimensional regularization framework and follow the matching strategy of [8] in order to compute the corrected contact term.

We first consider the surfer diagrams in Figs. 9(b)–9(d), which require novel calculation. All three give a generalized amplitude with the structure

$$\begin{aligned}\delta A_{S,i} = -iK \int \frac{d^4 l}{(2\pi)^4} \frac{i}{l^2 - m_\pi^2 + i\epsilon} \\ \frac{i}{l^2 - m_\pi^2 + i\epsilon} I_C(l^2, p^2, p'^2) I_{S,i}(l^2), \quad i = 1,2,3,\end{aligned} \tag{4.25}$$

where $I_C(l^2, p^2, p'^2)$ is the two-nucleon bubble integral, shown in [8] to have asymptotic ($p \sim p'$) real component $\frac{1}{8l}\theta(|l| - 2|p|)$, the partial amplitudes $I_{S,i}(l^2)$ encode the kinematics of the distinct pion-neutrino subdiagrams, and K encodes constant factors. We will see momentarily that the leading divergences of $I_{S,i}(l^2)$ in which we are interested will resolve to the form $Al^2 + B$, and so, very fortunately, we can factorize the internal one- and external two-loop integrals.

However, first, one further factorization can be performed, as all of the $I_{S,i}$ enjoy the same spin structure at the $NN\pi$ vertices. Following the normalization of [66,88], this p-wave charged-pion vertex is determined by the following term of the LO chiral Lagrangian:

$$\mathcal{L}_{\pi N} \ni \frac{g_A}{2F_\pi} \overline{N} \tau_a \sigma^j \nabla^j \pi_a N. \tag{4.26}$$

The isospin algebra (index a) is implicitly accounted for in our enforcement of charge conservation at each $NN\pi$ vertex; however, the spin algebra requires more thought.

Each $I_{S,i}$ will include an operator $\sigma_1 \cdot l\sigma_2 \cdot l$, where σ_i indicates the vector of Pauli spin operators on nucleon i. This operator may be decomposed into a spherical component $\frac{1}{3} l \cdot l\sigma_1 \cdot \sigma_2$, which we will need, and a tensor component $-\frac{1}{3} S_1 2$, which vanishes since we are only considering ${}^1S_0$ NN partial waves on the external legs. In this partial wave, $\sigma_1 \cdot \sigma_2 = -3$, so the total spin algebra factor is simply $-l^2$.

Now we perform the external integration separately for both $I_{S,i} = 1$ and $I_{S,i} = l^2$, a complete basis for our solution. Because we are working within a static nucleon approximation, pion-exchange momentum l needs only be treated within $D = 3$, averting the usual Wick rotation step. For $I_{S,i} = 1$, the resultant Euclidean integral is logarithmically solvable and divergent, and following [8] we regulate it with a cutoff scale $\mu_\pi \sim \Lambda_\chi$,

$$\begin{aligned}
\delta A_{S,i,1} &= -\frac{1}{8}\left(\frac{g_A}{2F_\pi}\right)^2 \int \frac{d^3 l}{(2\pi)^3} \frac{l^2}{(l^2+m_\pi^2)^2} \frac{1}{|l|} \theta(|l| - 2|p|) \\
&= -\frac{1}{8}\frac{1}{8\pi^2}\left(\frac{g_A}{2F_\pi}\right)^2 \int_{2|p|}^{\mu_\pi} dl \frac{l^3}{(l^2+m_\pi^2)^2} \\
&= -\frac{1}{8}\frac{1}{2\pi^2}\frac{1}{2}\left(\frac{g_A}{2F_\pi}\right)^2 \left[-\frac{m_\pi^2}{m_\pi^2+4p^2} + \frac{m_\pi^2}{m_\pi^2+{\mu_\pi}^2} + \log\left(\frac{m_\pi^2+{\mu_\pi}^2}{m_\pi^2+4p^2}\right)\right] \\
&\underset{p\to 0}{=} \frac{-g_A^2}{128\pi^2 F_\pi^2}\left[-1 + \frac{m_\pi^2}{m_\pi^2+{\mu_\pi}^2} + \log\left(1+\frac{{\mu_\pi}^2}{m_\pi^2}\right)\right].
\end{aligned} \tag{4.27}$$

For $I_{S,i} = l^2$, the Euclidean integral is solvable but naively appears quadratically divergent. The situation is analogous to the NN one-pion-exchange potential as treated in [18], whose momentum-space integral is proportional to

$$\frac{g_A^2}{4F_\pi^2}\int \frac{d^3 l}{(2\pi)^3}\frac{l^2}{l^2+m_\pi^2}\frac{1}{|l|} = \frac{g_A^2}{4F_\pi^2}\int \frac{d^3 l}{(2\pi)^3}\left(1 - \frac{m_\pi^2}{l^2+m_\pi^2}\right)\frac{1}{|l|}. \tag{4.28}$$

In the above, the latter term gives a convergent contribution to the one-pion-exchange bubble diagram (seen in Fig. 3). The former term is linearly divergent, but has the same form as the four-nucleon contact interaction C; in spatial coordinates, they are both $\delta^{(3)}(r)$ potentials. Thus, by setting the contact interaction $C \mapsto \tilde{C} = C + \frac{g_A^2}{4F_\pi^2}$, the linear divergence is absorbed into an existing, observable constant encoding short-range physics.

We assume, perhaps liberally, that our leading quadratic divergence can be absorbed into short-range parameters in a similar fashion; we isolate and subtract the linear term from the integrand, assuming that it can absorbed into the coefficient of the χEFT $NNNN\pi\pi$ vertex, which will only contribute to our process at a much lower order. This leaves only a logarithmic divergence, regularized as follows:

$$\begin{aligned}
\delta A_{S,i,l^2} &= -\frac{1}{8}\left(\frac{g_A}{2F_\pi}\right)^2 \int \frac{d^3 l}{(2\pi)^3} \frac{l^4}{(l^2+m_\pi^2)^2} \frac{1}{|l|} \theta(|l| - 2|p|) \\
&= -\frac{1}{8}\frac{1}{8\pi^2}\left(\frac{g_A}{2F_\pi}\right)^2 \int_{2|p|}^{\mu_\pi} dl \frac{l^5}{(l^2+m_\pi^2)^2} \\
&\underset{\text{subtraction}}{\to} -\frac{i}{8}\frac{1}{8\pi^2}\left(\frac{g_A}{2F_\pi}\right)^2 \int_{2|p|}^{\mu_\pi} dl \frac{m_\pi^4}{l(l^2+m_\pi^2)^2} - \frac{2m_\pi^2}{l(l^2+m_\pi^2)} \\
&= -\frac{1}{8}\frac{1}{2\pi^2}\frac{1}{2}\left(\frac{g_A}{2F_\pi}\right)^2 m_\pi^2 \left[-\frac{m_\pi^2}{m_\pi^2+{\mu_\pi}^2} + \frac{m_\pi^2}{m_\pi^2+4p^2} + 2\log\left(\frac{m_\pi^2+4p^2}{m_\pi^2+{\mu_\pi}^2}\right)\right] \\
&\underset{p\to 0}{=} \frac{-g_A^2 m_\pi^2}{128\pi^2 F_\pi^2}\left[1 - \frac{m_\pi^2}{m_\pi^2+{\mu_\pi}^2} - 2\log\left(1+\frac{{\mu_\pi}^2}{m_\pi^2}\right)\right].
\end{aligned} \tag{4.29}$$

Now we apply dimensional regularization to each of the $I_{S,i}$, making use of standard integration results similar to those shown by [13] in computing the one-loop chiral correction to the nucleon mass. $I_{S,1}$, corresponding to Fig. 9(b), is regularized as follows:

$$\begin{aligned} I_{S,1} &= 2\int \frac{d^4k}{2\pi^4}\frac{1}{(k-l)^2-m_\pi^2+i\epsilon}\frac{k^2}{k^2-m_\nu^2+i\epsilon} \\ &= 2\int \frac{d^4k}{2\pi^4}\frac{1}{(k-l)^2-m_\pi^2+i\epsilon} + 2\frac{1}{(k-l)^2-m_\pi^2+i\epsilon}\cdot\frac{m_\nu^2}{k^2-m_\nu^2+i\epsilon} \\ &= \frac{2m_\pi^2}{16\pi^2}\left(\frac{2}{\varepsilon}+\gamma_E-1-\log(4\pi)-\log\left(\frac{{\mu_\nu}^2}{m_\pi^2}\right)\right)+\mathcal{O}(m_\nu^2), \end{aligned} \tag{4.30}$$

where μ_ν is the scale of dimensional regularization, and where we employ a finite m_ν as a regulator, but find that such contributions are suppressed by $\frac{m_\nu^2}{m_\pi^2}$. Thus, applying the $\overline{\mathrm{MS}}$ scheme such that $\frac{2}{\varepsilon}+\gamma_E-\log(4\pi)-1$ is absorbed into the coupling constants of the Lagrangian [i.e., $g_A \mapsto g_A^{(r)}$, $F_\pi \mapsto F_\pi^{(r)}$] overall we find

$$\delta A_{S,1} = \frac{M_N^2}{(4\pi)^2}\frac{g_A^2 m_\pi^2}{64\pi^2 F_\pi^2}\left[-1+\frac{m_\pi^2}{m_\pi^2+\mu_\nu^2}+\log\left(1+\frac{\mu_\nu^2}{m_\pi^2}\right)\right]\left[\log\left(\frac{\mu_\pi^2}{m_\pi^2}\right)\right]. \tag{4.31}$$

Examining Fig. 9(c), we find that $I_{S,2}=I_{S,1}$ up to corrections of $\mathcal{O}(\frac{m_\nu^2}{m_\pi^2})$, since

$$\int \frac{d^4k}{2\pi^4}\frac{1}{k^2-m_\pi^2+i\epsilon}\frac{k^2}{k^2-m_\nu^2+i\epsilon} = \int \frac{d^4k}{2\pi^4}\frac{1}{k^2-m_\pi^2+i\epsilon}+\frac{1}{k^2-m_\pi^2+i\epsilon}\frac{m_\nu^2}{k^2-m_\nu^2+i\epsilon} \tag{4.32}$$

is equivalent to the integrand of $I_{S,1}$ after a shift in k [sans corrections of $\mathcal{O}(\frac{m_\nu^2}{m_\pi^2})$]. This equivalence is facilitated by chiral symmetry, via the equivalence of the $\pi\pi-\pi\pi$ and $\pi\pi\pi-\pi$ potentials seen in Table I.

Now considering Fig. 9(d), we will see that the four-pion vertex $\sim\frac{-2}{3F_\pi^2}(k^2+l^2-2m_\pi^2)$ will facilitate a demarcation into terms that are proportional either to l^2 or to a constant. Regularizing,

$$\begin{aligned} I_{S,3} &= \frac{-4F_\pi^2}{3F_\pi^2}\int \frac{d^4k}{2\pi^4}\frac{k^2+l^2-2m_\pi^2}{(k^2-m_\pi^2+i\epsilon)^2}\frac{k^2}{k^2-m_\nu^2+i\epsilon}+\mathcal{O}(m_\nu^2) \\ &= -\frac{4}{3}\int \frac{d^4k}{2\pi^4}\frac{k^2}{(k^2-m_\pi^2+i\epsilon)^2}\frac{k^2}{k^2-m_\nu^2+i\epsilon} \\ &\quad -\frac{4}{3}(l^2-2m_\pi^2)\int \frac{d^4k}{2\pi^4}\frac{1}{(k^2-m_\pi^2+i\epsilon)^2}\frac{k^2}{k^2-m_\nu^2+i\epsilon}+\mathcal{O}(m_\nu^2) \\ &= -\frac{1}{12\pi^2}\left(2m_\pi^2\log\left(\frac{\mu^2}{m_\pi^2}\right)+(l^2-2m_\pi^2)\log\left(\frac{{\mu_\nu}^2}{m_\pi^2}\right)\right)+\mathcal{O}(m_\nu^2) \\ &= -\frac{l^2}{12\pi^2}\log\left(\frac{{\mu_\nu}^2}{m_\pi^2}\right)+\mathcal{O}(m_\nu^2), \end{aligned} \tag{4.33}$$

where in the final steps we have enforced the $\overline{\mathrm{MS}}$ scheme and canceled all but the divergent term proportional to l^2. Then, combining with the result of the l^2 external integration Eq. (4.29), the regularized amplitude is

$$\delta A_{S,3} = \frac{M_N^2}{(4\pi)^2}\frac{g_A^2 m_\pi^2}{96\pi^2 F_\pi^2}\left[1-\frac{m_\pi^2}{m_\pi^2+{\mu_\pi}^2}-2\log\left(1+\frac{{\mu_\pi}^2}{m_\pi^2}\right)\right]\left[\log\left(\frac{{\mu_\nu}^2}{m_\pi^2}\right)\right]. \tag{4.34}$$

All of the calculated $A_{S,i}$ are displayed as functions of μ_ν and μ_π in Fig. 10, where the remarkable cancellation between the logarithmic divergences of $2A_{S,1}+2A_{S,2}$ and $2A_{S,3}$ is apparent. Shown alongside are enhanced models, where g_A is replaced with the dipole form factor defined in Eq. (3.6) with scale $\Lambda_A = 1.0$ GeV, with the intention of making the amplitudes more valid for the intermediate momenta between m_π and Λ_χ. These enhanced models will prove essential for a matching analysis analogous to that performed by [8] in the NN case. In addition to these contributions, we quote the amplitude for the eye diagram (top row in Fig. 8) as computed in Appendix C of [8],

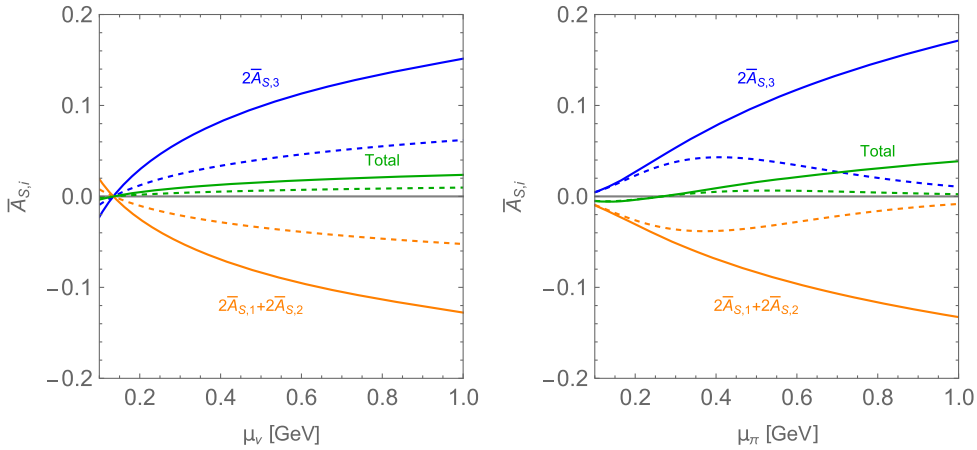

FIG. 10. Dimensionless amplitudes for surfer diagrams 1 and 2 (orange), 3 (blue), and their sum (green), as functions of regularization scales μ_ν (left) and μ_π (right), with the respective other scale set to $\mu_\pi = 0.5$ GeV. In both plots, the solid lines show the direct χEFT result, while the dashed lines show the enhanced model defined in the text, where g_A is replaced with its dipole form factor.

$$\delta A_E = \frac{M_N^2}{(4\pi)^2}\int_0^{\mu_\nu} dk\,\delta a_E(k),$$
$$\text{where } \delta a_E(k) = \frac{1+2g_A^2}{2(4\pi F_\pi)^2}\left[k\left(1+\log\frac{\mu_\pi m_\pi}{(k+\sqrt{k^2+m_\pi^2})^2}\right)+m_\pi F\left(\frac{k}{m_\pi}\right)\right],$$
$$F(x) = \sqrt{1-x^2}\left[\tan^{-1}\left(\frac{x^2}{\sqrt{1-x^4}}\right)-\tan^{-1}\left(\frac{x}{\sqrt{1-x^2}}\right)\right] \tag{4.35}$$

and where we have made the substitution $1+3g_A^2 \mapsto 1+2g_A^2$ in accordance with the induced pseudoscalar component of the NN neutrino potential in χEFT. Note that the final integration in neutrino momentum k for this diagram has not been analytically solved; in order to compare apples to apples with our analytically regulated amplitudes for the surfer diagrams, we define partial amplitudes

$$a_{s,i}(\mu_\nu) \equiv \frac{d}{d\mu_\nu}A_{s,i}(\mu_\nu). \tag{4.36}$$

Strictly speaking, these distributions are not physically meaningful; they encode the density of an amplitude that one obtains while increasing the dimensional regularization scale, rather than amplitude densities over loop momentum k defined before regularization. However, we will only use them for visualization purposes and to verify our power counting, instead applying $A_{s,i}(\mu_\nu)$ directly when we compute the contact counterterm coefficient.

Recall that three adjustable scales appear in this procedure: the neutrino loop regularization scale μ_ν appearing above, which is the running renormalization scale of the counterterm coefficient g_{NN}^ν; the pion loop regularization scale μ_π, which we treat with a simple momentum cutoff, as does Appendix C of [8]; and the matching scale Λ, which was seen in [8] to introduce negligible error into the counterterm estimate for $1 < \Lambda < 4$ GeV. We will follow [8] in choosing the renormalization point $\mu_\nu = m_\pi$ for quoted values of g_{NN}^ν, but emphasize that the entire function $g_{NN}^\nu(\mu_\nu)$ is the physical quantity that this analysis aims to predict.

The partial amplitudes for all three surfer diagrams are shown in Figs. 11(b)–11(d) for example pion regularization

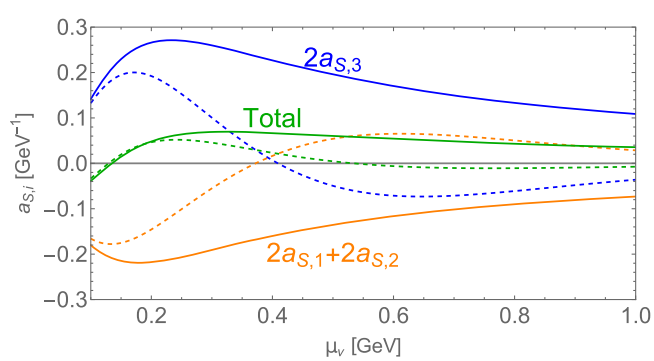

FIG. 11. Partial amplitudes (defined in text) for surfer diagrams 1 and 2 (orange), 3 (blue), and their sum (green), as functions of regularization scale μ_ν with $\mu_\pi = 0.5$ GeV. The solid lines show the direct χEFT result, while the dashed lines include a dipole form factor for g_A.

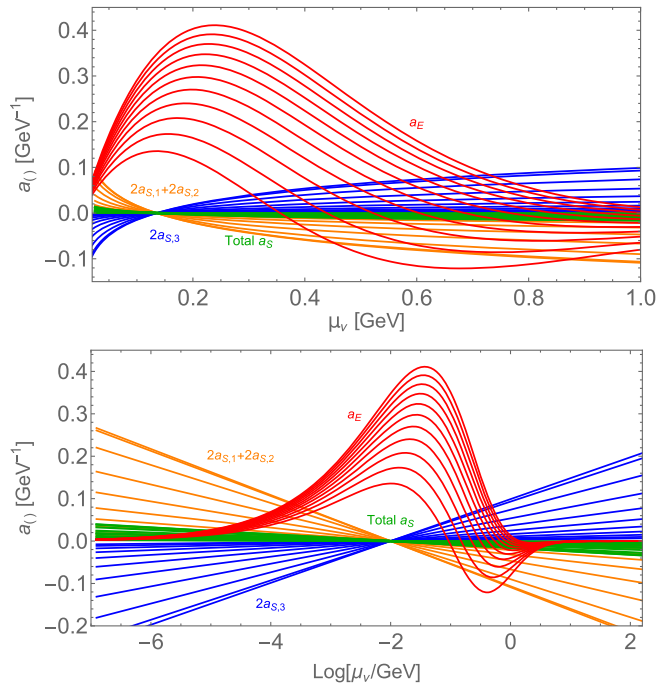

FIG. 12. Partial amplitudes for the eye diagram (red), surfer diagrams 1 and 2 (orange), 3 (blue), their sum (green), as functions of regularization scale μ_ν shown linearly (top) and logarithmically (bottom). μ_π is varied between $0.5\Lambda_\chi$ and $1.5\Lambda_\chi$, and the dipole g_A form factor is included throughout.

point $\mu_\pi = 0.5$ GeV, where again the significant cancellation is apparent, as well as some indication that virtual momenta above nuclear scales contribute diminishing amounts to these diagrams. To illustrate sensitivity of our results to the pion regularization point, Fig. 12 again shows the partial amplitudes for the surfer diagrams as well as for the eye diagram treated in [8], for a range of μ_π values between $0.5\Lambda_\chi$ and $1.5\Lambda_\chi$. One notices immediately that, although the partial amplitude for the eye diagram suffers from some significant pion regularization scale dependence, the sum of partial amplitudes for the surfer diagrams is nearly vanishing across a broad range of both μ_π and μ_ν; in fact, the total surfer diagram contribution exactly vanishes at $\mu_\nu = m_\pi$ (the representative nuclear scale chosen here and by [8]), regardless of μ_π. We can say roughly that the chiral symmetry inherent in our treatment of this nuclear system has enforced a natural smallness of pion loops through both the permitted neutrino currents and the combinatorics. This exact cancellation will be broken by electromagnetic effects that separate m_{π^0} and $m_{\pi^\pm}$, but these should only be relevant 1 chiral order lower than our diagrams, at N^{3}LO.

To illustrate the size of these contributions relative the partial amplitudes a_χ, $a_<$, and $a_>$ needed for the matching analysis of [8], we interpret our χEFT result as a correction on a_χ, while we interpret its enhanced g_A form factor counterpart as a correction on $a_<$. In a more complete analysis, phenomenological pion-nucleon form factors would be included in a corrected $a_<$ alongside an appropriate extension of the half-off-shell form factors used in [8] to improve the robustness of the NN contact interactions. We will treat these possible extensions as falling within the uncertainties accorded to the choice of the short-range potential and see that this simple parametrization of intermediate-momentum behavior is enough to deliver a corrected matching result with expected scale dependence properties. There is certainly no need to adjust $a_>$ within the precision desired in this analysis, since as discussed in [8]

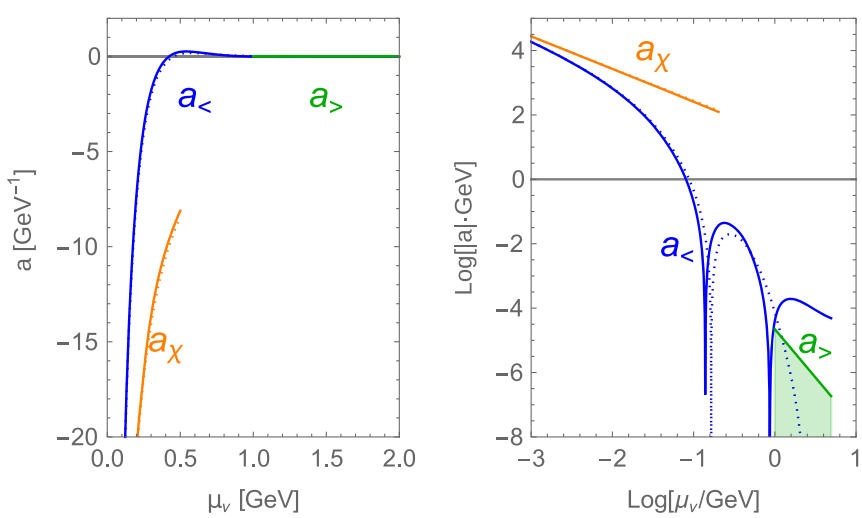

FIG. 13. Total partial amplitudes for the matching analysis following Fig. 6 of [8], where a_χ is accurate in the low-momentum exchange region up to $\sim m_\pi$, $a_<$ is the enhanced model for the intermediate-momentum exchange region, $a_>$ is the high-momentum exchange OPE from perturbative QCD, and the pion regularization scale is fixed at $\mu_\pi = \Lambda_\chi$. The solid lines include all four $NN\pi$ partial amplitudes, while the dotted lines include only the NN results of [8].

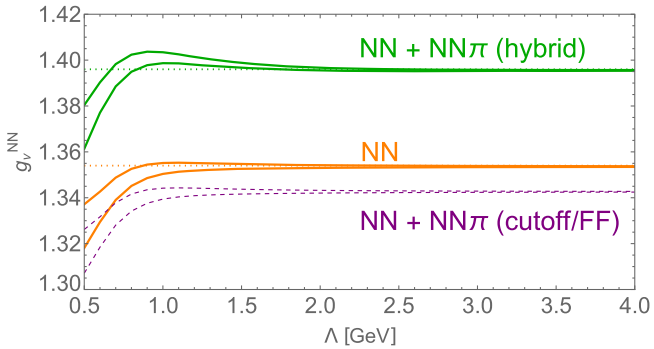

FIG. 14. Computed low-energy constant g_ν^{NN} from combined NN and $NN\pi$ amplitudes using the naive low-momentum schemes described in the text (purple), a more robust low- and intermediate-momentum scheme (green), in comparison with the NN-only result following [8] (orange). The weak dependence of g_ν^{NN} on matching scale Λ is seen, and all computations are performed at pion regularization scale $\mu_\pi = \Lambda_\chi$ and neutrino regularization scale $\mu_\nu = m_\pi$.

the role of this partial amplitude is primarily to enforce finiteness in the UV, and at any rate, the quark-level diagrams used in its calculation already include at least some inelastic intermediate nuclear states.

In Fig. 13 the corrected partial amplitudes for the matching analysis are plotted (solid) in comparison to the NN-only partial amplitudes from [8] (dotted). Viewed globally, these corrections are almost invisible to the eye, certainly smaller than say 5%, showing the most discrepancy in the $0.1 < \mu_\nu < 0.5$ GeV range where the eye partial amplitude is strongest.

With these partial amplitudes in hand, we can perform a preliminary matching analysis analogous to that of [8] to estimate the corrected size of the contact counterterm g_ν^{NN}. In practice, this amounts to implementing Eq. (3.40) on our corrected partial amplitudes, and in particular, we propose a hybrid matching scheme where the pure χEFT corrections and those including a g_A form factor are applied separately to a_χ and $a_<$, thus preserving the demarcation between low- and intermediate-momentum physics. However, other schemes are plausible: naively, one might assume that due to our incomplete knowledge of the intermediate-momentum range, we should only apply our corrections to a_χ, either with a hard cutoff or with the softer inclusion of the g_A dipole form factor (FF). The results of all three approaches, at $\mu_\nu = m_\pi$, $\mu_\pi = \Lambda_\chi$, and as a function of matching scale Λ, are displayed in Fig. 14. We find that, in our hybrid matching scheme, the size of $g_\nu^{NN}(\mu_\nu = m_\pi)$ is enhanced from 1.35 to 1.40, an increase of just under 4%, while generic independence of sufficiently large matching scale Λ is preserved. The suppression of 1% in the naive cutoff and form factor schemes, in our view, neglects relevant intermediate-momentum-scale physics that is present in our analysis. However, at the very least, it provides an additional confirmation that the $NN\pi$ correction g_ν^{NN} is small, well below the 38% uncertainty allocated by [8]. Note also that our value of 1.35 for the NN-only counterterm size differs from the value of 1.34 quoted by [8]; this difference appears to be entirely attributable to updated measurement of m_π and so does not represent a correction but rather an update on the NN-only result.

In Fig. 15, we illustrate the dependence of these results on the neutrino regularization scale μ_ν. As expected, the size of

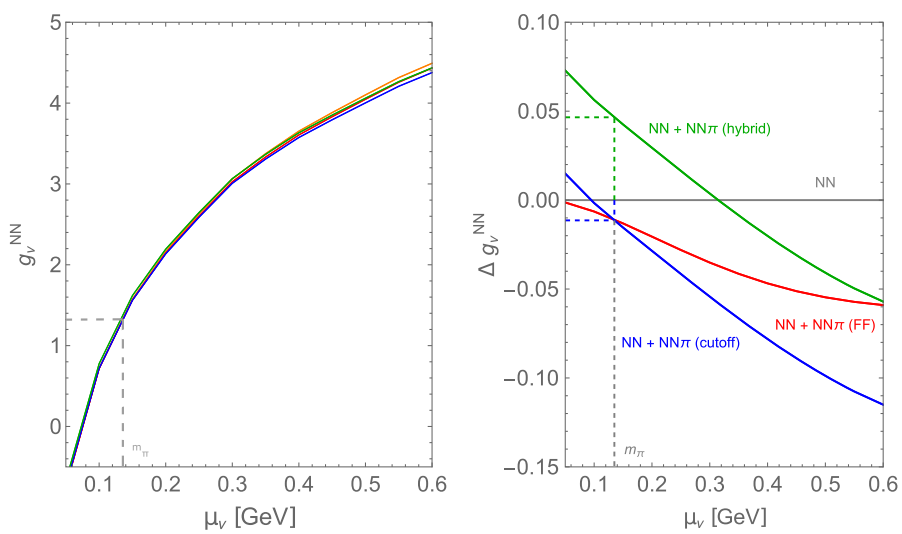

FIG. 15. Computed low-energy constant g_ν^{NN} from combined NN and $NN\pi$ amplitudes using the naive low-momentum schemes described in the text (purple), a more robust low- and intermediate-momentum scheme (green), in comparison with the NN-only result (orange). The logarithmic dependence of g_ν^{NN} on neutrino regularization scale μ_ν is seen, and all computations are performed at pion regularization scale $\mu_\pi = \Lambda_\chi$ and matching scale $\Lambda = \Lambda_\chi$. Global similarity of the running coupling is demonstrated on the left, while the right shows the NN_π corrections Δg_ν^{NN} by scheme, where the values at chosen scale $\mu_\nu = m_\pi$ correspond to Fig. 14.

the correction remains small across all μ_ν and, globally, we can state that the shape of the renormalization group of g_ν^{NN} is adjusted very little. However, the total corrections to g_ν^{NN} are scale dependent; in the hybrid scheme they vary between $-0.06 < \Delta g_\nu^{NN} < 0.07$ for scales $0.05 < \mu_\nu < 0.6$ GeV. The results according to the naive cutoff and form factor schemes diverge from one another as one moves away from $\mu_\nu = m_\pi$ and the surfer diagram contributions become larger; however, all three schemes exhibit decreasing scale dependence of Δg_ν^{NN}. In other words, accounting for $NN\pi$ diagrams has served to improve the scale dependence of g_ν^{NN}, albeit very slightly.

In total, we quote the following $NN\pi$-corrected result for the size of the $\Delta L = 2$ contact counterterm first estimated by [8], representing a ~4% increase in its size:

$$g_\nu^{NN} \simeq 1.40(20)_{V_S}(5)_{\text{parameters}}(3)_{\text{inelastic}} = 1.4(3). \tag{4.37}$$

Regarding our uncertainties, we retain the short-range potential and parameter uncertainties claimed by [8], since we have not sought to make improvements on the calculation in either of these areas, and since we have not introduced any dramatically different short-range physics or physical parameters into the picture that would be more prone to uncertainty. In addition, we have checked that reasonable variation of our model parameters (namely, Λ_A in the g_A dipole form factor) does not exceed $\delta = 0.05$.

Our remaining inelastic uncertainty is derived from the power counting performed in Fig. 9, from which all unaccounted for, subleading $NN\pi$ diagrams are expected to contribute not more than 0.016 uncertainty to the total correction amplitude. $NN\pi\pi$ and more-pion intermediate states only begin to contribute at N^{4}LO in our power counting and can be expected to be safely subpercentile. We suggest that the inclusion of Δ and heavier resonance intermediate states in our analysis, because it would require a full extension of the underlying χEFT framework to include explicit heavier degrees of freedom, is already accounted for in the short-range potential uncertainty $\delta_{V_S} = 0.20$. To account for any N^{3}LO Δ-resonance diagrams that might contribute at N^{3}LO to our power counting of diagrams, we conservatively double our remaining inelastic uncertainty to give $\delta_{\text{inelastic}} = 0.03$.

Therefore, in addition to identifying a ~5% increase in the size of the contact counterterm owing to $NN\pi$ intermediate states, our χEFT framework demonstrates a reduction of inelastic uncertainties from the ~38% of [8] to ~3%, corresponding to a total uncertainty improvement from ~46% to ~21%. Thus, the dominant source of contact counterterm uncertainty, rather than inelastic states, is the selection of a short-range internucleon potential for intermediate momenta.

V. DISCUSSION

The complexity of the nuclear many-body problem and resultant wide spread in estimates of NMEs remains the primary obstacle to improving the precision of our theoretical understanding of $0\nu\beta\beta$ decay. While development continues for a variety of computational methods based on phenomenological nuclear theory, a growing proportion of the nuclear theory community has come to view *ab initio*, first principles nuclear theory as the most promising way forward. Uncertainty quantification in *ab initio* nuclear theory is more rigorous than in phenomenological models, granting insights into disagreements between calculations and ultimately the systematic improvement of many-body methods as well as the NMEs they predict [89].

In this work, we have attempted to expand upon the calculation of the contact counterterm contribution to $0\nu\beta\beta$ decay, as first noted in Ref. [5] and quantified for elastic intermediate states in Refs. [7,8]. At renormalization point $\mu = m_\pi$, this estimate was

$$g_\nu^{NN}|_{NN} \simeq 1.32(50)_{\text{inelastic}}(20)_{\text{V}_\text{S}}(5)_{\text{parameters}} = 1.3(6), \tag{5.1}$$

where a total of ~46% uncertainty is present, dominated by the ~38% uncertainty arising from the choice to only account for elastic intermediate hadronic states. By accounting for $NN\pi$ intermediate states, we have generated an improved estimate of the contact coefficient

$$g_\nu^{NN}|_{NN+NN\pi} \simeq 1.40(20)_{V_S}(5)_{\text{parameters}}(3)_{\text{inelastic}} = 1.4(3), \tag{5.2}$$

where a total of ~21% uncertainty is present, only ~3% now stemming from the intermediate-state truncation (an order of magnitude reduction). As indicated in Sec. IV E, additional work will be required to ensure the robustness of this intermediate-state correction through intermediate-momentum scales. Further improvements in precision could mainly be obtained through careful characterization of the short-range nuclear potentials employed in modeling that intermediate-momentum scale.

A distinct verification of the size of the contact counterterm, justifying in part the relation to charge independence breaking low-energy constants made in [5], was recently performed by [90,91] using a large-N_c analysis. We note that their determination, like ours, favors a slightly larger g_ν^{NN} than the elastic truncation, and that our results agree within uncertainties.

Recently, the author became aware of a new and alternative approach by [92], in which the $0\nu\beta\beta$-decay amplitude is computed using the manifestly Lorentz-invariant chiral Lagrangian of [93]. Just as Ref. [93] shows how to absorb all UV divergences for S-wave NN scattering, Ref. [92] claims that this relativistic Lagrangian leads to an $0\nu\beta\beta$-decay amplitude that requires no counterterm at

LO. The resultant LO amplitude is numerically compatible with the nonrelativistic approach with a counterterm and, therefore, our improved precision estimate as well; it would be interesting to consider whether the subleading corrections presented here have an analogous effect in the relativistic setting.

To obtain an *ab initio* estimate of the NME for $0\nu\beta\beta$ decay in a given isotope, input from the two- and few-nucleon scale must be provided to an appropriate many-body method; popular contenders include the self-consistent Green's function approach [94], the in-medium similarity renormalization group (IMSRG) [95], coupled-cluster methods [96], and the in-medium generator coordinate method (IM-GCM) [97]. NME estimates from these approaches, built upon long-range few-nucleon inputs only, skew smaller than estimates from most phenomenological nuclear models, with the consequence that a given $0\nu\beta\beta$-decay search will probe less of new-physics parameter space. The most recent calculation based on IMSRG [98] suggested as much as an order-of-magnitude decrease in experimental reach or, rather, that biased estimates based on phenomenological nuclear models have overinflated experimental reach by this amount.

Reference [99] was the first to produce NME estimates that include the contact counterterm as input, demonstrating (within a no-core shell model) a $\sim$15% enhancement in ^{6}He compared to the long-range-only estimate. References [98,100] similarly applied IMSRG and IM-GCM incorporating the contact counterterm to experimentally relevant isotopes such as ^{76}Ge; compared to the long-range-only NME estimates, these results show 40%–90% enhancements depending on the isotope. As a result, a significant portion of the experimental reach that was lost in proceeding from a phenomenological to an *ab initio* nuclear model is restored. Since our improved precision estimate of the contact term has resulted in only a very small adjustment of the central value, within even the improved uncertainties, we should therefore anticipate a tightening of the *ab initio* NME estimates, without much movement.

Clearly, it is essential both to the interpretation and design of future $0\nu\beta\beta$-decay searches that the remaining theoretical uncertainties embedded in these *ab initio* estimates be suitably resolved. As [98] explains, many of these theoretical uncertainties will arise from neglected many-body effects, e.g., in IMSRG; these are beyond the scope of this work and represent significant future endeavors of the nuclear theory community. However, other theoretical uncertainties arise from the two-nucleon scale, and it is precisely those uncertainties on the contact counterterm that we have here reduced by a factor of 2.

ACKNOWLEDGMENTS

The author wishes to thank, first and foremost, their doctoral supervisor Frank Deppisch for essential guidance and feedback in pursuing this line of research. The author also thanks Matteo Agostini, Patrick Bolton, James Canning, Vincenzo Cirigliano, Jonathan Engel, Jason Holt, Emanuelle Mereghetti, and Fedor Šimkovic for illuminating conversations that helped to bring this work to completion. G. V. G., in particular, acknowledges support from the UCL Centre for Doctoral Training in Data Intensive Science, funded by STFC, from the UCL Overseas Research Scholarship/Graduate Research Scholarship, and the Science and Technology Facilities Council, part of U.K. Research and Innovation, Grants No. ST/P00072X/1, No. ST/T000880/1, No. ST/T004169/1, and No. ST/W00058X/1, as well as support from the University of Southampton and Grant No. ST/W006251/1 during the writing of this work.

DATA AVAILABILITY

No data were created or analyzed in this study.

[1] M. Doi, T. Kotani, H. Nishiura, and E. Takasugi, Double beta decay, Prog. Theor. Phys. **69**, 602 (1983).

[2] M. J. Dolinski, A. W. Poon, and W. Rodejohann, Neutrinoless double-beta decay: Status and prospects, Annu. Rev. Nucl. Part. Sci. **69**, 219 (2019).

[3] J. Engel and J. Menéndez, Status and future of nuclear matrix elements for neutrinoless double-beta decay: A review, Rep. Prog. Phys. **80**, 046301 (2017).

[4] M. Agostini, G. Benato, J. A. Detwiler, J. Menéndez, and F. Vissani, Toward the discovery of matter creation with neutrinoless $\beta\beta$ decay, Rev. Mod. Phys. **95**, 025002 (2023).

[5] V. Cirigliano, W. Dekens, J. de Vries, M. L. Graesser, E. Mereghetti, S. Pastore and U. van Kolck, New leading contribution to neutrinoless double-β decay, Phys. Rev. Lett. **120**, 202001 (2018).

[6] V. Cirigliano, W. Dekens, J. de Vries, M. L. Graesser, E. Mereghetti, S. Pastore, M. Piarulli, U. van Kolck, and R. B. Wiringa, Renormalized approach to neutrinoless double-β decay, Phys. Rev. C **100**, 055504 (2019).

[7] V. Cirigliano, W. Dekens, J. de Vries, M. Hoferichter, and E. Mereghetti, Toward complete leading-order predictions for neutrinoless double β decay, Phys. Rev. Lett. **126**, 172002 (2021).

[8] V. Cirigliano, W. Dekens, J. de Vries, M. Hoferichter, and E. Mereghetti, Determining the leading-order contact term in neutrinoless double β decay, J. High Energy Phys. 05 (2021) 289.

[9] K. G. Wilson, Confinement of quarks, Phys. Rev. D **10**, 2445 (1974).

[10] G. t'Hooft, The topological mechanism for permanent quark confinement in a non-Abelian gauge theory, Phys. Scr. **25**, 133 (1982).

[11] S. L. Adler, Axial-vector vertex in spinor electrodynamics, Phys. Rev. **177**, 2426 (1969).

[12] J. S. Bell and R. W. Jackiw, A PCAC puzzle: $\pi^0 \to \gamma\gamma$ in the σ-model, Nuovo Cimento **60**, 47 (1969).

[13] S. Scherer and M. R. Schindler, *A Primer for Chiral Perturbation Theory* (Springer Science & Business Media, New York, 2011), Vol. 830.

[14] S. Weinberg, Phenomenological Lagrangians, Physica (Amsterdam) **96A**, 327 (1979).

[15] A. Manohar and H. Georgi, Chiral quarks and the non-relativistic quark model, Nucl. Phys. **B234**, 189 (1984).

[16] E. Jenkins and A. V. Manohar, Baryon chiral perturbation theory using a heavy fermion Lagrangian, Phys. Lett. B **255**, 558 (1991).

[17] S. Weinberg, Nuclear forces from chiral Lagrangians, Phys. Lett. B **251**, 288 (1990).

[18] D. B. Kaplan, M. J. Savage, and M. B. Wise, Nucleon-nucleon scattering from effective field theory, Nucl. Phys. **B478**, 629 (1996).

[19] P. D. Group, R. L. Workman, V. D. Burkert, V. Crede, E. Klempt, U. Thoma *et al.*, Review of particle physics, Prog. Theor. Exp. Phys. **2022**, 083C01 (2022).

[20] S. Weinberg, Effective chiral Lagrangians for nucleon-pion interactions and nuclear forces, Nucl. Phys. **B363**, 3 (1991).

[21] V. G. J. Stoks, R. A. M. Klomp, C. P. F. Terheggen, and J. J. de Swart, Construction of high-quality *nn* potential models, Phys. Rev. C **49**, 2950 (1994).

[22] R. Machleidt, High-precision, charge-dependent bonn nucleon-nucleon potential, Phys. Rev. C **63**, 024001 (2001).

[23] E. Epelbaum, H. Krebs, and P. Reinert, High-precision nuclear forces from chiral EFT: State-of-the-art, challenges, and outlook, Front. Phys. **8**, 98 (2020).

[24] D. R. Phillips, What hath Weinberg wrought? reflections on what Weinberg's papers on 'nuclear forces from chiral Lagrangians' did and did not accomplish, Few-Body Syst. **63**, 23 (2022).

[25] H. P. Noyes, The nucleon-nucleon effective range expansion parameters, Annu. Rev. Nucl. Sci. **22**, 465 (1972).

[26] M. A. Preston, *Structure of the Nucleus* (CRC Press, Boca Raton, 2018).

[27] D. B. Kaplan, M. J. Savage, and M. B. Wise, A new expansion for nucleon-nucleon interactions, Phys. Lett. B **424**, 390 (1998).

[28] D. R. Phillips and T. D. Cohen, How short is too short? constraining zero-range interactions in nucleon-nucleon scattering, Phys. Lett. B **390**, 7 (1997).

[29] H. W. Hammer, C. Ji, and D. R. Phillips, Effective field theory description of halo nuclei, J. Phys. G **44**, 103002 (2017).

[30] V. Efimov, Energy levels arising from resonant two-body forces in a three-body system, Phys. Lett. **33B**, 563 (1970).

[31] P. Naidon, L. Pricoupenko, and C. Schmickler, Shallow trimers of two identical fermions and one particle in resonant regimes, SciPost Phys. **12**, 185 (2022).

[32] P. F. Bedaque and U. V. Kolck, Effective field theory for few-nucleon systems, Annu. Rev. Nucl. Part. Sci. **52**, 339 (2002).

[33] B. Long, Power counting for nuclear forces in chiral effective field theory, Int. J. Mod. Phys. E **25**, 1641006 (2016).

[34] V. Bernard, T. R. Hemmert, and U.-G. Meissner, Cutoff schemes in chiral perturbation theory and the quark mass expansion of the nucleon mass, Nucl. Phys. **A732**, 149 (2004).

[35] S. Fleming, T. Mehen, and I. W. Stewart, NNLO corrections to nucleon–nucleon scattering and perturbative pions, Nucl. Phys. **A677**, 313 (2000).

[36] S. R. Beane, P. F. Bedaque, M. J. Savage, and U. van Kolck, Towards a perturbative theory of nuclear forces, Nucl. Phys. **A700**, 377 (2002).

[37] S. R. Beane, D. B. Kaplan, and A. Vuorinen, Perturbative nuclear physics, Phys. Rev. C **80**, 011001 (2009).

[38] E. Epelbaum, H. Krebs, and P. Reinert, *Semi-Local Nuclear Forces from Chiral EFT: State-of-the-Art and Challenges* (Springer, New York, 2022), pp. 1–25.

[39] A. Nogga, R. G. E. Timmermans, and U. van Kolck, Renormalization of one-pion exchange and power counting, Phys. Rev. C **72**, 054006 (2005).

[40] M. C. Birse, Power counting with one-pion exchange, Phys. Rev. C **74**, 014003 (2006).

[41] E. Epelbaum, H. Krebs, and U.-G. Meißner, Precision nucleon-nucleon potential at fifth order in the chiral expansion, Phys. Rev. Lett. **115**, 122301 (2015).

[42] R. J. Furnstahl, N. Klco, D. R. Phillips, and S. Wesolowski, Quantifying truncation errors in effective field theory, Phys. Rev. C **92**, 024005 (2015).

[43] J. A. Melendez, S. Wesolowski, and R. J. Furnstahl, Bayesian truncation errors in chiral effective field theory: Nucleon-nucleon observables, Phys. Rev. C **96**, 024003 (2017).

[44] S. Wesolowski, R. J. Furnstahl, J. A. Melendez, and D. R. Phillips, Exploring bayesian parameter estimation for chiral effective field theory using nucleon–nucleon phase shifts, J. Phys. G **46**, 045102 (2019).

[45] F. Šimkovic, G. Pantis, J. D. Vergados, and A. Faessler, Additional nucleon current contributions to neutrinoless double β decay, Phys. Rev. C **60**, 055502 (1999).

[46] V. Cirigliano, W. Dekens, J. de Vries, M. L. Graesser, and E. Mereghetti, Neutrinoless double beta decay in chiral effective field theory: Lepton number violation at dimension seven, J. High Energy Phys. 12 (2017) 82.

[47] I. S. Towner and J. C. Hardy, Currents and their couplings in the weak sector of the standard model, in Symmetries and fundamental interactions in nuclei (World Scientific, 1995), p. 183.

[48] V. Bernard, H. W. Fearing, T. R. Hemmert, and U.-G. Meißner, The form factors of the nucleon at small momentum transfer, Nucl. Phys. **A635**, 121 (1998).

[49] V. Cirigliano, W. Dekens, E. Mereghetti, and A. Walker-Loud, Neutrinoless double-β decay in effective field theory: The light-Majorana neutrino-exchange mechanism, Phys. Rev. C **97**, 065501 (2018).

[50] X. Kong and F. Ravndal, Coulomb effects in low energy proton–proton scattering, Nucl. Phys. **A665**, 137 (2000).

[51] W. N. Cottingham, The neutron proton mass difference and electron scattering experiments, Ann. Phys. (N.Y.) **25**, 424 (1963).

[52] N. Barnea, L. Contessi, D. Gazit, F. Pederiva, and U. van Kolck, Effective field theory for lattice nuclei, Phys. Rev. Lett. **114**, 052501 (2015).

[53] R. Zwicky, A brief introduction to dispersion relations and analyticity (2016), 10.3204/DESY-PROC-2016-04/Zwicky.

[54] J. Gasser and H. Leutwyler, Implications of scaling for the proton-neutron mass difference, Nucl. Phys. **B94**, 269 (1975).

[55] J. Gasser, H. Leutwyler, and A. Rusetsky, On the mass difference between proton and neutron, Phys. Lett. B **814**, 136087 (2021).

[56] R. Horsley, Z. Koumi, Y. Nakamura, H. Perlt, D. Pleiter, P. Rakow *et al.*, Isospin splittings in the decuplet baryon spectrum from dynamical QCD + QED, J. Phys. G **46**, 115004 (2019).

[57] T. Das, G. S. Guralnik, V. S. Mathur, F. E. Low, and J. E. Young, Electromagnetic mass difference of pions, Phys. Rev. Lett. **18**, 759 (1967).

[58] J. F. Donoghue and A. F. Pérez, Electromagnetic mass differences of pions and kaons, Phys. Rev. D **55**, 7075 (1997).

[59] P. Colangelo and A. Khodjamirian, *QCD Sum Rules, a Modern Perspective* (World Scientific, Singapore, 2001), pp. 1495–1576.

[60] K. Wilson, On products of quantum field operators at short distances, Cornell Report No. LNS-64-15, 1364 (1964).

[61] K. G. Wilson and W. Zimmermann, Operator product expansions and composite field operators in the general framework of quantum field theory, Commun. Math. Phys. **24**, 87 (1972).

[62] M. A. Shifman, A. I. Vainshtein, and V. I. Zakharov, Qcd and resonance physics. theoretical foundations, Nucl. Phys. **B147**, 385 (1979).

[63] D. B. Kaplan and J. V. Steele, Long and short of nuclear effective field theory expansions, Phys. Rev. C **60**, 064002 (1999).

[64] R. V. Reid Jr, Local phenomenological nucleon-nucleon potentials, Ann. Phys. (N.Y.) **50**, 411 (1968).

[65] R. B. Wiringa, V. G. J. Stoks, and R. Schiavilla, Accurate nucleon-nucleon potential with charge-independence breaking, Phys. Rev. C **51**, 38 (1995).

[66] C. Hanhart, Meson production in nucleon–nucleon collisions close to the threshold, Phys. Rep. **397**, 155 (2004).

[67] V. Malafaia, Pion production reactions in nucleon-nucleon collisions, arXiv:nucl-th/0602026.

[68] D. H. Wilkinson, Parity conservation in strong interactions: Introduction and the reaction $he^4(d,\gamma)li^6$, Phys. Rev. **109**, 1603 (1958).

[69] S. Mandelstam, Determination of the pion-nucleon scattering amplitude from dispersion relations and unitarity. general theory, Phys. Rev. **112**, 1344 (1958).

[70] E. Ferrari and F. Selleri, An approach to the theory of single pion production in nucleon-nucleon collisions, Nuovo Cimento (1955–1965) **27**, 1450 (1963).

[71] G. F. Chew and F. E. Low, Effective-range approach to the low-energy p-wave pion-nucleon interaction, Phys. Rev. **101**, 1570 (1956).

[72] A. E. Woodruff, Semiphenomenological analysis of the process $p + p \to d + \pi^+$ near threshold, Phys. Rev. **117**, 1113 (1960).

[73] D. S. Koltun and A. Reitan, Double-charge-exchange scattering of low-energy pions by nuclei, Phys. Rev. **139**, B1372 (1965).

[74] G. F. Bertsch and D. O. Riska, Threshold pion absorption in nuclei, Phys. Rev. C **18**, 317 (1978).

[75] T.-S. H. Lee and D. O. Riska, Short range exchange contributions to the cross section for $pp \to pp\pi^0$ near threshold, Phys. Rev. Lett. **70**, 2237 (1993).

[76] E. Hernández and E. Oset, Off shell πn amplitude and the $pp \to pp\pi^0$ reaction near threshold, Phys. Lett. B **350**, 158 (1995).

[77] T. D. Cohen, J. L. Friar, G. A. Miller, and U. van Kolck, $pp \to pp\pi^0$ reaction near threshold: A chiral power counting approach, Phys. Rev. C **53**, 2661 (1996).

[78] B.-Y. Park, F. Myhrer, J. R. Morones, T. Meissner, and K. Kubodera, Chiral perturbation approach to the $pp \to pp\pi^0$ reaction near threshold, Phys. Rev. C **53**, 1519 (1996).

[79] V. Bernard, N. Kaiser, and U.-G. Meissner, Novel approach to pion and eta production in proton-proton collisions near threshold, Eur. Phys. J. A **4**, 259 (1999).

[80] C. Hanhart and N. Kaiser, Complete next-to-leading-order calculation for pion production in nucleon-nucleon collisions at threshold, Phys. Rev. C **66**, 054005 (2002).

[81] C. Hanhart, U. van Kolck, and G. A. Miller, Chiral three-nucleon forces from p-wave pion production, Phys. Rev. Lett. **85**, 2905 (2000).

[82] V. Baru, E. Epelbaum, J. Haidenbauer, C. Hanhart, A. E. Kudryavtsev, V. Lensky and U.-G. Meißner, p-wave pion production from nucleon-nucleon collisions, Phys. Rev. C **80**, 044003 (2009).

[83] A. A. Filin, V. Baru, E. Epelbaum, H. Krebs, C. Hanhart, A. E. Kudryavtsev and F. Myhrer, Pion production in nucleon-nucleon collisions in chiral effective field theory: Next-to-next-to-leading order contributions, Phys. Rev. C **85**, 054001 (2012).

[84] A. A. Filin, V. Baru, E. Epelbaum, H. Krebs, C. Hanhart, and F. Myhrer, Pion production in nucleon-nucleon collisions in chiral effective field theory with $\delta(1232)$ degrees of freedom, Phys. Rev. C **88**, 064003 (2013).

[85] V. Baru, E. Epelbaum, A. A. Filin, C. Hanhart, H. Krebs, and F. Myhrer, Threshold pion production in proton-proton collisions at nnlo in chiral EFT, Eur. Phys. J. A **52**, 146 (2016).

[86] U. V. Kolck, The problem of renormalization of chiral nuclear forces, Front. Phys. **8**, 79 (2020).

[87] H.-W. Hammer, S. König, and U. van Kolck, Nuclear effective field theory: Status and perspectives, Rev. Mod. Phys. **92**, 025004 (2020).

[88] V. Bernard, N. Kaiser, and U.-G. Meißner, Chiral dynamics in nucleons and nuclei, Int. J. Mod. Phys. E **04**, 193 (1995).

[89] V. Cirigliano, Z. Davoudi, J. Engel, R. J. Furnstahl, G. Hagen, U. Heinz *et al.*, Towards precise and accurate calculations of neutrinoless double-beta decay, J. Phys. G **49**, 120502 (2022).

[90] T. R. Richardson, M. R. Schindler, S. Pastore, and R. P. Springer, Large-n_c analysis of two-nucleon neutrinoless double-β decay and charge-independence-breaking contact terms, Phys. Rev. C **103**, 055501 (2021).

[91] T. Richardson, Large-n_c constraints for beyond the standard model few-nucleon currents in effective field theory, in *The 10th International Workshop on Chiral Dynamics* (Proceedings of Science, Trieste, 2024), p. 98.

[92] Y. Yang and P. Zhao, Relativistic model-free prediction for neutrinoless double beta decay at leading order, Phys. Lett. B **855**, 138782 (2024).

[93] E. Epelbaum and J. Gegelia, Weinberg's approach to nucleon–nucleon scattering revisited, Phys. Lett. B **716**, 338 (2012).

[94] V. Soma, Self-consistent green's function theory for atomic nuclei, Front. Phys. **8**, 340 (2020).

[95] H. Hergert, In-medium similarity renormalization group for closed and open-shell nuclei, Phys. Scr. **92**, 023002 (2016).

[96] G. Hagen, T. Papenbrock, M. Hjorth-Jensen, and D. J. Dean, Coupled-cluster computations of atomic nuclei, Rep. Prog. Phys. **77**, 096302 (2014).

[97] J. Yao, J. Engel, L. Wang, C. Jiao, and H. Hergert, Generator-coordinate reference states for spectra and $0\nu\beta\beta$ decay in the in-medium similarity renormalization group, Phys. Rev. C **98**, 054311 (2018).

[98] A. Belley, T. Miyagi, S. Stroberg, and J. Holt, *Ab initio* calculations of neutrinoless $\beta\beta$ decay refine neutrino mass limits, arXiv:2307.15156.

[99] R. Wirth, J. M. Yao, and H. Hergert, *Ab initio* calculation of the contact operator contribution in the standard mechanism for neutrinoless double beta decay, Phys. Rev. Lett. **127**, 242502 (2021).

[100] J. M. Holt, *Ab initio* theory for heavy nuclei and the physics of neutrinos and dark matter, *Plenary Talk Given at the 7th Symposium on Neutrinos and Dark Matter in Nuclear Physics (NDM22)* (Asheville, NC, 2022).